University of Crete
Department of Materials Science and Technology

Photonic Devices of Piezoelectric Quantum Dots

Savvas Germanis

Heraklion, Greece, October 2015

Savvas Germanis

Photonic Devices of Piezoelectric Quantum Dots

Thesis
submitted to the Department of Materials Science and Technology, University of Crete
for the Degree of Doctor of Philosophy in Materials Science.

Heraklion, Greece, October 2015

Photonic Devices of Piezoelectric Quantum Dots

Thesis author	Savvas Germanis
Thesis supervisor	Prof. Nikolaos T. Pelekanos
Thesis committee	Prof. Pavlos Savvidis Prof. Vallia Voliotis Associate Prof. Zacharias Chatzopoulos Associate Prof. Thomas Kehagias Associate Prof. George Kiosseoglou Tenured Prof. Ioannis Remediakis

Department of Materials Science and Technology, University of Crete
Heraklion, Greece

October 2015

This thesis is dedicated to my mom, Maria Andradopoulou who always encouraged me to go for every adventure and never give up.

Abstract

Semiconductor Quantum Dots (QDs) are an ideal artificial system to study fundamental properties of matter and the ultimate component of quantum information processing. Towards the implementation of a tunable source of single photons or entangled photon pairs, we present here a study on self-assembled InAs/GaAs QDs, grown on a high-index (211)B GaAs substrate. The system has all the benefits of regular and well-studied (100) InAs/GaAs QDs, but additionally has a fascinating characteristic, which is the presence of a large vertical piezoelectric (PZ) field inside the QDs, bringing in a number of significant advantages, which are illustrated in this work. First, the PZ field along the growth direction preserves the high symmetry of the confining potential, leading to negligible fine structure splitting (FSS) values in the system, which is essential for entanglement applications. By polarization resolved micro-photoluminescence experiments we deduce negligible FSS values of PZ QDs, which make them good candidates for quantum information applications. Second, the PZ field generates large exciton-biexciton energy splittings, which is prerequisite for single photon applications at high temperatures. This ability is demonstrated by cross-correlation experiments on single exciton emission lines, showing clear anti-bunching behaviour at elevated temperatures. Third, due to the pronounced PZ field, the emission wavelength of these QDs should be very sensitive to an applied external electric field, leading to significant Stark shifts in this QD system. To explore this, a special dot-containing diode structure has been fabricated and studied, and enhanced Stark tuning of the QD emission has been observed. Finally, our results provide a clear demonstration of the importance of non-linear piezoelectric effects in Zinc-Blende semiconductors.

Acknowledgements

I have been fortunate to spend my time at F.O.R.T.H, in the Microelectronics Research Group, under the supervision of Prof. Nikolaos T. Pelekanos. Prof. Pelekanos has introduced me into the magic world of applied quantum mechanics, taught me not only a lot of physics, but also a way of thinking and a way of doing research as a physicist. He also gave me the ability to collaborate with other groups in Greece and France which luckily happened in the beginning of my career giving me possibility to share knowledge and work together with passionate scientist such as Prof. Pavlos Savvidis, Dr. Alexios Beveratos, Prof. Valia Voliotis, Prof. Thomas Kehagias and Dr. George Konstandinidis, who have also gathered, a brilliant and talented group of students and researchers, who have helped me in my thesis work. I would also like to express my gratitude to Prof. Zacharias Chatzopoulos, for the MBE samples.

I would like to thank the current and former Microelectronics Research Group members, whom I have cooperated with, but here I mention by name only those who have contributed most directly to the work, reported in this thesis: Dr. Simeon Tsintzos, Dr. Rahul Jayaprakash, George Dialynas, Maria Androulidaki, Katerina Tsagaraki, Maria Kayabaki and Antonios Stavrinidis.

I would also like to thank the technicians of MRG, Nikolaos Papadakis and Michael Sfendourakis, without whose technical support I would never have been able to do anything in the laboratory. I would also like to extent my requrds to the administrative staff member, Maria Karavasili responsible for the financial support of the program Herakleitus II. This research has been co-financed by the European Social Fund and Greek national funds through the Program "Education and Lifelong Learning" of the National Strategic reference Framework - Research Funding Program: Herakleitus II (KA 3396).

Last but not the least, a special thank you to my family, friends and Effrosyni Mitsopoulou who helped me make this happen!

Contents

Chapter 1

Introduction

1.1 Quantum Dots: Background

A new technological era has risen from the merger of quantum and solid state physics, giving place to the research field of modern semiconductor physics. We are living in a rapidly-developing world, where new knowledge can be translated into high-end devices with electronic, photonic and optoelectronic applications. The new question is, can we go further by exploiting the quantum properties of man-made semiconductor structures and nanostructures.

Semiconductor Quantum Dots (QDs) are offering an ideal artificial quantum laboratory to study fundamental properties of matter, by naturally embedding complex nanostructures in materials with wider band gap, making them attractive for different kinds of electronic and photonic devices such as semiconductor lasers, detectors and modulators. There are many types of QDs based on the different fabrication techniques such as lithographically defined QDs, chemically synthesized QDs, naturally formed QDs through interface fluctuations, and self-assembled QDs by epitaxial growth techniques. The latter type of QDs can be composed of a wide variety of alloy semiconductors and their optical transitions cover the full spectral

range from the ultraviolet ∼350nm down to the mid infrared ∼ 1.5μm.

1.1.1 Optical and Electronic Properties:Band Structure

A semiconductor QD is a nano-structure of a semiconductor material with a band gap E_g^2 embedded in a matrix of another semiconductor of larger band-gap E_g^1. The new band gap E_g^{QD} of the QD, obeys to the relation $E_g^1 > E_g^{QD} > E_g^2$ and corresponds to the optical transition energy between the first quantum confined electron and hole levels inside a 3D potential well, whose dimensions are smaller than the *De-Broglie* wavelength of the charge carriers in the respective semiconductor (≃12nm for InAs).

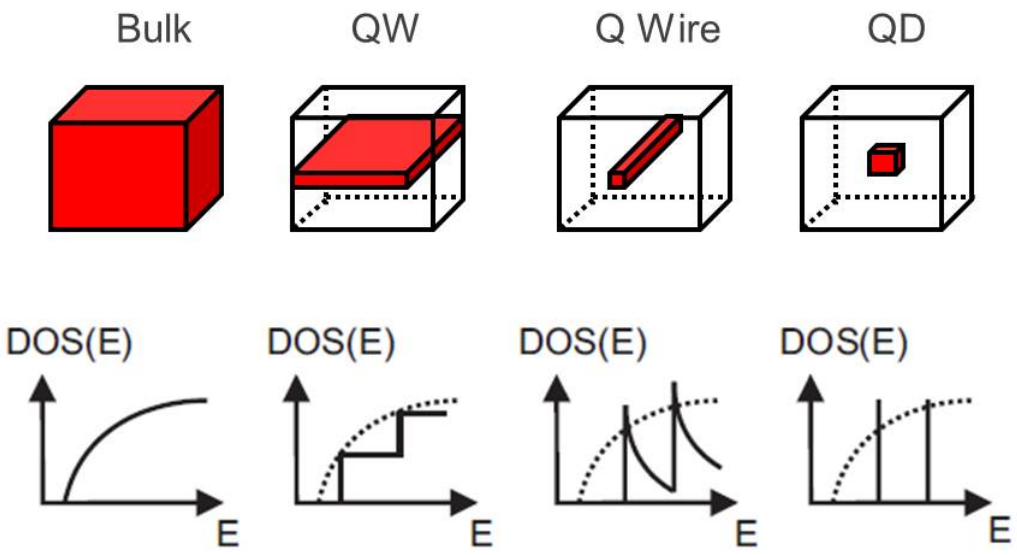

Figure 1.1: Graphical representations for the Density Of States (DOS) for bulk semiconductor, quantum well, quantum wire and quantum dot. The DOS for the QDs is discrete while all others have a continuous DOS.

The mobility of charge carriers then is limited and quantum mechanical effects govern the electronic properties of the semiconductor nano-structure. In general, we can classify three categories of nanostructures according to the number of con-

fined dimensions: Quantum Wells (QWs), where the carriers are confined in one dimension, usually along the growth direction, Quantum Wires, which cause a confinement in two dimensions, while the electrons and holes move freely in one dimension, and finally, Quantum Dots (QDs), inside which the carriers are experiencing a three dimensional confinement. The density of states (DOS) of a structure or heterostructure that reflects the dimensionality of the confinement is depicted in figure 1.1. We observe that in all cases, the DOS stays continuous, while in QDs shows a delta function-like DOS. This means that when electrons and holes recombine in a QD, they give rise to a discrete energy transition, very much like that of an atom.

1.1.2 Excitons and Biexcitons

Figure 1.2(a) shows a one-dimensional band diagram of a QD, with the band discontinuity between the two materials resulting to a potential well. If an electron-hole pair is generated, the two opposite charges are attracted and captured inside the QD potential well.

The electrons and holes in the QD have ground (n=0, e0/h0) and excited (n=1,2... e1,e2.../h1,h2...) states. The discrete energy states for electrons and holes differ from the conduction band and valence band edges of the low energy band gap material and the difference between them is a function of effective masses, the form of the confinement potential and the morphology of the QD.

The electron-hole (e-h) pair which is trapped in the QD potential is further attracted by Coulomb interaction forming an exciton state, thus we can picture the new quasi-particle named as exciton (X). The excitons typically separate in two categories according to the strength of the attraction developed among e-h. When it is strong they are called Frenkel excitons and can be found in ionic

crystals, whereas Wannier excitons, which are those of interest in this work, refer to electron hole pairs weakly bound to each other.

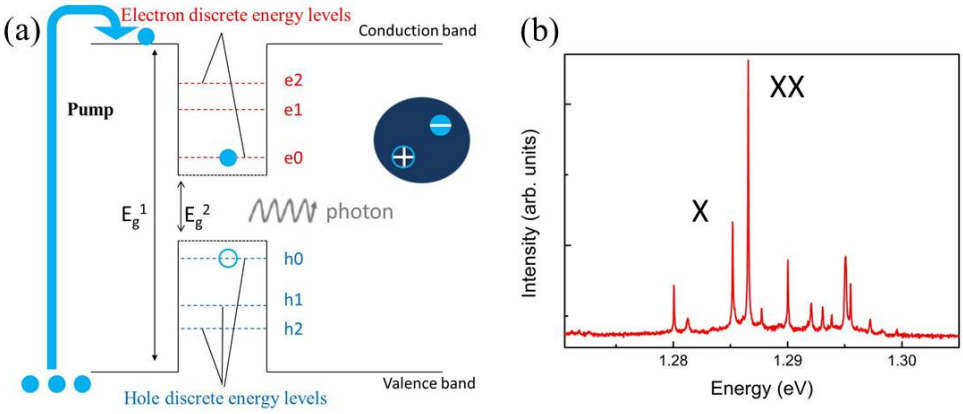

Figure 1.2: (a) One dimensional scheme of the electronic structure of the QD. Non-resonant pumping above the band gap of GaAs is depicted and the emission from an exciton state is accompanied with a visualization of the exciton as a quasi-particle. (b) The photoluminescence spectrum of a few InAs/GaAs QDs under excitation above GaAs band gap. The two sharp lines denoted as X and XX correspond to exciton and biexciton emission from a single QD, generated by the cascade process, explained in the text.

The two particle system, i.e. an electron in the conduction band and a hole in the valence band, can be described by a Hamiltonian H.

$$H = H_e + H_h, \tag{1.1}$$

Due to e-h interaction, the exciton energy is determined by the following Hamiltonian H_X for the bound exciton state, including Coulomb interaction which reads as

$$H_X = H_e + H_h + H_{Coulomb}, \tag{1.2}$$

Where the single particle Hamiltonian for electrons is H_e, for holes is H_h and

$H_{coulomb}$ is the Coulomb interaction between them. The total energy of a bound exciton state is lower than the energy of the uncorrelated e-h pair due to the Coulomb attraction, by an amount called the *exciton binding energy*. In a bulk material, the exciton binding energy is often called the Rydberg energy, R_y, and the exciton transition energy is given by the following equation using the effective mass approximation.

$$E_X(n) = E_g - \frac{R_y}{n^2}, \tag{1.3}$$

Where n=1,2,.. is the exciton state quantum number, $R_y = \frac{\mu e^2}{2\hbar^2\varepsilon^2}$ is the Rydberg energy which corresponds to the exciton ionization energy. The Rydberg energy also includes the Bohr radius for the excitons which is $\alpha_X = \frac{\hbar^2\varepsilon}{\mu e^2}$ where $\mu = \frac{m^e_{eff}m^h_{eff}}{m^e_{eff}+m^h_{eff}}$ is the reduced mass and ε is the dielectric constant of the medium.

At low temperatures, the main decay process for the exciton in direct gap semiconductors is the radiative recombination, as this is depicted in figure 1.2(a), accompanied by the generation of a photon.

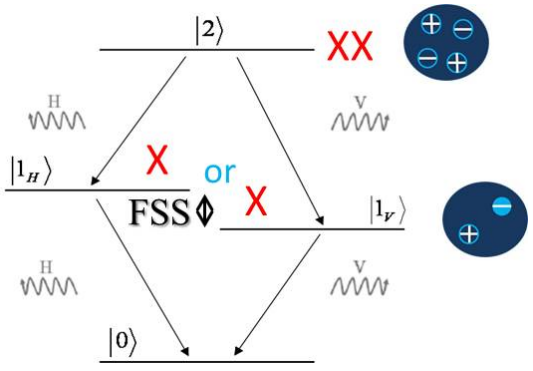

Figure 1.3: Schematic of biexciton cascade through the intermediate exciton state, generating a polarized photon pair.

If we consider an excitation scheme where the system is pumped above the band gap it is possible to form more than one excitons. In this case, inside the QD, two e-h pairs are captured at the same time, and the new quasi-particle named as biexciton (XX) is created. Then, one of the two electrons can be recombined with the one of the two holes and generate a photon. The remaining e-h pair then can recombine as aforementioned. In other words, the biexciton decays through the intermediate exciton state, and the total process results in the generation of a polarized photon pair as shown in figure1.3. The polarization splitting of the intermediate exciton state will be described in the FSS session and chapter 2.

1.2 Main applications

As previously mentioned, single QDs are nanometer-sized semiconductor entities providing confinement to the carriers (electrons and holes) in all three directions, resulting to a discrete energy spectrum. The zero-dimensional character of QD states attracted the scientific community early on, for a number of applications. One of them is to use the QDs as active medium in laser systems. As predicted by Y. Arakawa et al. [1] the threshold current density of quantum dot lasers could be much lower compared to that of quantum well lasers due to the zero-dimensional character of their density of states. Several technological difficulties were overcome twelve years later, when N. Kirstaedter et al. [2] used QDs as an active material in an injection laser structure, and five years later, the first QD-based laser became a reality. G. Liu et al. [3] demonstrated an very low threshold laser with a single layer of InAs QDs embedded inside an $In_{0.15}Ga_{0.85}As$ quantum well. It was the first time that the threshold current density performance of QD lasers had surpassed that of QW lasers even at room temperature. In parallel to these research activities, where the photonic devices made use of a considerably large number of QDs, in

the millions, scientists have started investigating experimental methods in order to isolate and to study single QDs.

The field of fundamental research that develops, optimizes structures and studies isolated Single QDs (SQDs) is called *Single Quantum Dot Spectroscopy*. The high spatial and spectral resolution which is needed in order to isolate the emission from a SQD sets high experimental standards. Towards this direction, A. Zrenner et al. [4], through optical experiments, resolved sets of extremely narrow emission lines near and below the fundamental band gap energy of GaAs QW, attributed to natural QDs which are formed by well width fluctuations inside the GaAs QW. Then, J. Y. Marzin et al. [5] and M. Grundmann et al. [6] reported photoluminescence (PL) and cathodoluminescence (CL) spectra respectively, of narrow emission lines originating from single InAs QDs. Even though the recorded spectra consisted of the emission from more than one QDs, it was the first experimental evidence of the δ-function character of the density of QD states, as it was expected.

One of the first experimental evidence of a *spectrally* isolated SQD was presented by D. Hessman et al. [7] by successfully recording a PL spectrum from a single InP QD, using a gold mask with nano-aperture openings on top of the structure to isolate the emission of one dot from the ensemble of QDs. Next P. Michler et al. [8] and C. Santori et al. [9] experimentally proved that a SQD is a single photon emitter "on demand". In other words, a SQD has the possibility to generate a regulated photon stream, containing one and only one photon in a given time interval. In their experiments, this was expressed by the clear anti-bunching behaviour of a SQD. This anti-bunching behaviour sets the QDs in the heart of the new field of quantum cryptography, with applications in secure quantum key distribution systems, where security from eavesdropping depends on the ability to produce no more than one photon at a time, as proposed by G. Brassard et al. [10].

Even though a heavily attenuated laser pulse can be used to produce a stream

of single photons for quantum key distribution, it is clear that a true source of single photons "on demand" would greatly improve the performance of such systems [11]. Up to now, single photon emission from QDs at elevated temperatures has been demonstrated in a II-VI QD system, up to 220K for (Cd,Zn)Se/Zn/Se QD [12], and in group-III nitrides, up to room temperature with GaN/AlN QDs [13].

Clearly, however, for the realistic implementation of a single photon device, electrical pumping is necessary, and from this point of view the GaAs-based QDs hold a concrete advantage due to all the available technological know-how. Regarding GaAs-based QDs, R. Mirin et al [14] with 120K single photon operation, holds the highest temperature record in optical pumping conditions, while up to now the only electrically driven single photon device based on arsenides has been presented by X. Dou et al. [15] at liquid Nitrogen conditions. As discussed below, the piezoelectric QDs have the potential to surpass these limitations due to the large Exciton-Biexciton energy splittings that can easily exceed 10 meV, allowing us to aim at single photon emitters operating at elevated temperatures.

Another very interesting possibility of QDs is to be used as quantum light sources in future quantum communication and teleportation systems, where the quantum networks distribute keys over very long distances using *entangled photon pairs* [16]. An ideal source of entangled photon pairs could be a conveniently triggered QD generating one entangled photon pair per excitation pulse. As proposed by Benson et al. [17], this can occur by the cascade emission process from a QD biexciton state through the intermediate exciton state to the QD ground state, provided that the fine structure splitting (FSS) of the intermediate exciton state is smaller than the radiative linewidth of the exciton emission line. Then, the two optical paths become "indistinguishable" and produce polarization entangled photon pairs. This kind of entanglement is very similar to that in atoms [18]. Even though this kind of experiments have already been performed in both optical and

electrical pumping conditions [19], they have been limited up to now to cryogenic temperatures (∼10K) and required several cumbersome techniques to reduce or cancel the FSS. On the other hand, InAs/GaAs QDs grown on high index substrates such as (111), have been proposed to exhibit *as-grown*, zero or negligible FSS [20, 21, 22]. In this work, we show that the (211)B InAs QDs exhibit reduced FSS values compared to their (100) counterparts [23], and along with their potential for single photon emission at elevated temperatures, we truly believe that the PZ QDs hold the key for the implementation of practical single and entangled photon sources at elevated temperatures.

1.3 Motivation of this Work

In this work, we focus on piezoelectric QDs, i.e. QDs containing a strain-induced internal electric field. More specifically, the QD structures that attract our interest are InAs QDs grown on (211)B GaAs substrates, allowing us to take full advantage of the available GaAs technology. As will be discussed in the next chapters, piezoelectric QDs exhibit clear advantages for applications such as single photon sources (SPS) operating at elevated temperatures, entangled photon sources and tunable single photon emitters. Our final aim is to provide new standards for semiconductor QD applications by exploiting the optical properties of piezoelectric QDs.

1.3.1 Piezoelectric QDs.

The main feature of the QD system studied in this work, is the piezoelectric field (PZ). The piezoelectricity stems from the epitaxial growth of the QD heterostructure on (211)B GaAs substrates. The (211) crystallographic orientation of Zinc Blende structure is a member of the polar high index (N11) crystallographic ori-

entations family, able to produce piezoelectric fields when appropriate strain is applied to the system. We will now describe in a pictorial way, how the piezoelectricity appears along high index crystallographic orientation of a Zinc Blende lattice.

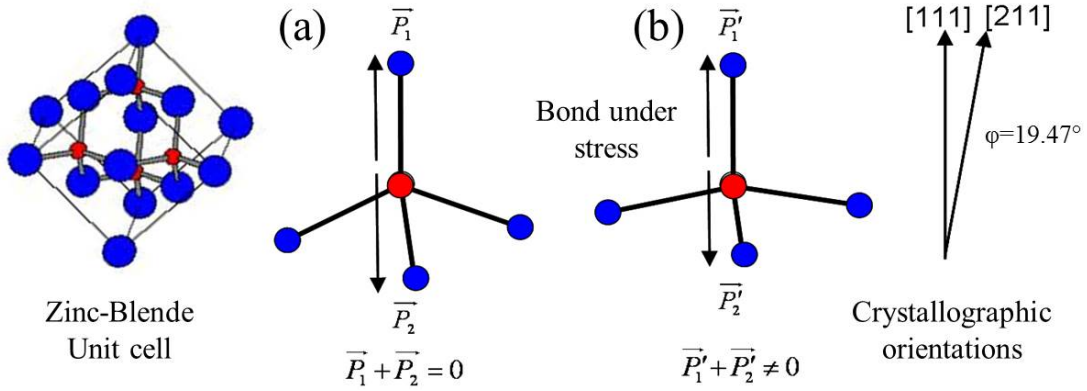

Figure 1.4: Schematic representation of the polarization induced due to a mechanical deformation along the (111) crystallographic orientation of Zinc Blende structure.

The epitaxy of materials with different lattice constants, on polar orientation substrates, creates a mechanical bond deformation due to strain, resulting in the appearance of net polarization between the III-V ions along the growth axis. As we can see in figure1.4(a) for a (111) orientation, without strain, the four tetrahedral bonds form a perfect tetra-pole whose total polarization is zero. The situation changes radically when we have strain, as the four bonds become deformed, resulting in a net total dipole along the (111) direction of the tetrapod, as depicted in figure1.4(b).

The situation in (211) crystallographic orientation resembles closely that of the (111) schematic depicted in figure1.4, and explains the appearance of PZ field in our nanostructures as discussed next.

We can consider now the construction of a chain of such dipoles as in fig-

ure1.5(a). The positive charge of each dipole is neutralized by its adjacent negative charge, and only the top and bottom bound charges survive creating a dipole along the chain. In the body of a QD many of such dipole chains exist, as visible in figure1.5(b), along the axis of growth, resulting to the appearance of a surface bound charge density on the apex and the base of the QD, and the generation of an internal electric field. Since this field is initiated by strain is referred to as piezoelectric field.

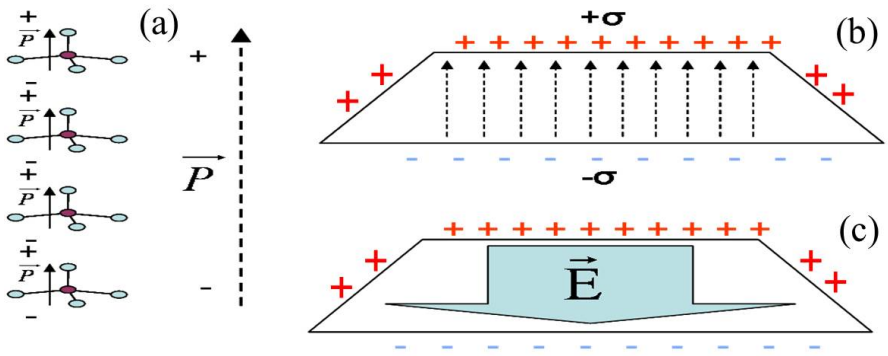

Figure 1.5: (a) a chain of dipoles and the appearance of a total dipole along the chain. (b) A macroscopic view of the surface charge in a QD. (c) The induced field.

In actuality, the generation of a piezoelectric field in a semiconductor is slightly more complicated, as the field is generated not only by the deformation of the ionic positions, but also from the response to strain of their surrounding electronic clouds. Nevertheless, the ionic picture provides a good base for understanding in a simple manner the origins of piezoelectricity in (N11) QDs.

The consequences of the strain-induced PZ field in the QDs will be addressed in the next sections and the details will be analysed in the next chapters.

1.3.2 Fabrication Method

Before continuing any further, some main points on QD fabrication will be addressed. We focus mainly on epitaxially grown piezoelectric QDs and their optical and electronic properties. The piezoelectric (PZ) InAs QDs which are presented in this thesis are grown by Molecular Beam Epitaxy (MBE) in the Stranski-Krastanov method on (211)B GaAs substrates. This method consists of depositing materials with large lattice mismatch, such as InAs on GaAs with a 7% lattice mismatch. With this method, after the deposition of a critical InAs thickness of ∼1.4 monolayers (ML) on top of GaAs, begins the formation of InAs islands due to elastic relaxation of the mechanical strain. These islands constitute the QDs. The PZ QDs are taking the shape of truncated pyramids, typically 1.5-2.5 nm thick and 20-35 nm large.

Several conditions during the growth have strong effect on the optical and structural properties of QDs. The substrate temperature typically varies during the epitaxy of the different layers in the QD heterostructure. For example, the optimal temperature during the GaAs growth is 620°C whereas the temperature before the InAs growth is ramped down to 480°C, which is critical for the formation of InAs QDs along (211)B crystallographic orientation. The fluxes of materials and the growth time should also be controlled very carefully for a successful sample growth. The growth parameters affect the shape and size of QDs, as well as the amount of Ga atoms exchanging places with those of In in the InAs QD matrix, changing dramatically the optical properties which can be visualized through the photoluminescence spectrum of the QDs. Moreover, these conditions determine the high purity and quality of the interfacial InAs/GaAs layer, which is responsible for non-radiative recombination centers. More information about the samples fabrication and structural properties will be given in the next chapters.

1.3.3 Enhanced Quantum Confined Stark Effect.

The presence of internal PZ field developed inside the (211)B QD results to the following effects:

1. Band bending of the conduction and valence bands.

2. Spatial separation of electrons and holes, decreasing their wavefunctions overlap and oscillator strength of the corresponding optical transition.

3. Redshift of the transition energy according to the Quantum Confinement Stark Effect (QCSE)[24].

4. The biexciton transition energy can be expected at higher energies than the exciton transition energy due to increased carrier screening of the PZ field in the biexciton case [25].

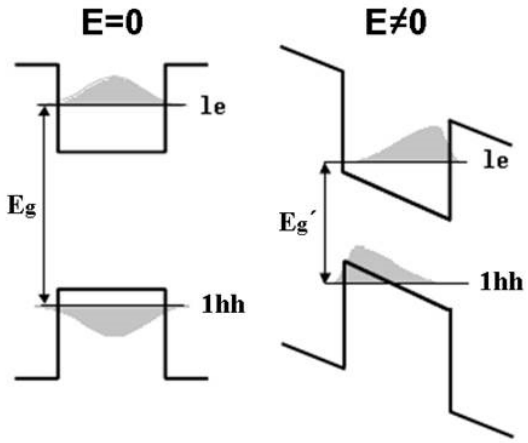

Figure 1.6: Schematic representation of the band alignment without and with applied electric Field **E**. The electron and hole wavefunctions are shown with gray and due to band bending caused by the field are realigned. The exciton transition energy E_g changes to $E_g^{'}$.

Efficient emission tuning.

The pronounced PZ effect along polar orientations can be exploited to efficiently tune the emission from a PZ QD, as this QD system is very sensitive to the application of small external fields.

The idea is described in figure1.7, where for a given applied external electric field, shown with arrows, the corresponding Stark shift in the presence of the internal PZ field, ΔE_2, is much larger than ΔE_1, i.e. the Stark shift obtained in the absence of the PZ field, as is the case of the (100) non-piezoelectric QDs. Moreover, heavily-strained PZ QDs are a model system for demonstrating non-linear PZ effects [26], as will be discussed in Chapter 5.

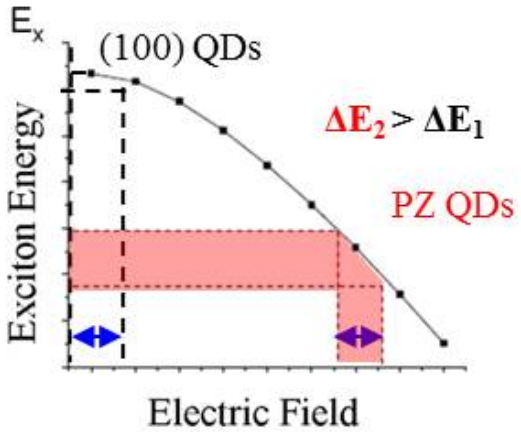

Figure 1.7: Schematic representation of the enhanced Stark Shift of the exciton transition energy in the case of PZ QDs versus non-PZ QDs.

The work demonstrating enhanced Stark effect on the exciton emission line of a SQD by applying an external bias as well as the first experimental evidence for non-linear piezoelectric effects in InAs/GaAs (211)B QDs will be presented in Chapter 5.

1.3.4 Low Fine Structure Splitting values

It is possible that inside the potential well of a QD two (e-h) pairs (i.e. excitons) are captured at the same time leading to the formation of the biexciton. The formation of the exciton states follows the allowed configurations depending on the charge carriers spin. Electrons and holes as Fermions carry a half-integer spin and obey to the Pauli's exclusion principle. The exciton states are formed by the superposition of an electron with angular momentum $m_s = \pm\frac{1}{2}$ and a Heavy hole with angular momentum $m_j = \pm\frac{3}{2}$. The total angular momentum of an exciton state can be $M_{dark} = \pm 2$ (dark states) or $M_{bright} = \pm 1$ (bright states) [27]. The latter ones, are called bright because the recombination of an e-h pair is able to generate a photon with spin ± 1, while this is not possible with the dark states. The pure exciton state is normally a fourfold degenerate state, but the presence of exchange interaction between electrons and holes removes this degeneracy. The new non-degenerate states consist of the following symmetric and anti-symmetric bright 1.4 and dark 1.5 doublets.

$$\{\frac{1}{\sqrt{2}}|1\rangle + |-1\rangle\}, \{\frac{1}{\sqrt{2}}|1\rangle - |-1\rangle\} \tag{1.4}$$

$$\{\frac{1}{\sqrt{2}}|2\rangle + |-2\rangle\}, \{\frac{1}{\sqrt{2}}|2\rangle - |-2\rangle\} \tag{1.5}$$

In figure1.8 the two bright states are shown, along with the linearly polarized decay paths starting from the degenerate biexciton state with zero total angular momentum. The energy difference between the bright exciton states is the *Fine Structure Splitting* (FSS) which is caused by the anisotropy of the confinement potential, lifting the degeneracy of the bright states and leading into two well-defined energy levels.

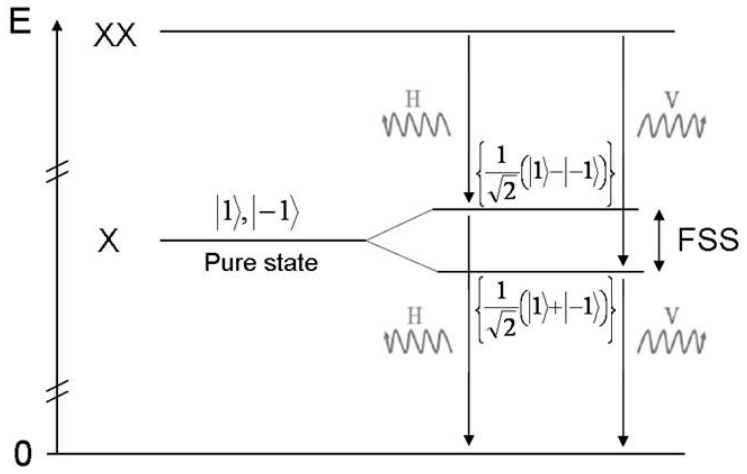

Figure 1.8: Energy scheme for the XX,X and global ground states in a QD without exchange interaction (left side) and with exchange interaction between electrons and holes (right side). In the diagram is also visible the bright doublet of the exciton state, the FSS energy splitting between the non-degenerate states and all the possible optical transitions from the excited biexciton state allthe way down to the relaxed ground state in a QD.

We can consider the FSS as a measure of the symmetry of the confinement potential. The factors that influence and lower the confinement symmetry are : i) Structural anisotropy of the QD. For instance the elongation of QD base, reduces the symmetry of the confinement potential to C_{2V} compared to the C_{4V} which applies for the case of isotropic potential [28], ii) Strain-induced lateral piezoelectric fields developed at side facets of a QD [29].

In recent works, it has been proposed that a high piezoelectric field along the growth direction can preserve the high symmetry of the confinement potential to C_{3V} and in that case the expected FSS values can be close to zero [20, 21, 22]. In Chapter 2, we present results confirming negligible FSS values in *as-grown* (211)B InAs/GaAs PZ QDs, making them attractive for the generation of entangled photon pairs as discussed in Chapter 2.

1.3.5 Anti-binding Biexciton energy.

The fourth effect which is expected in PZ QDs is attributed to electron-electron and hole-hole Coulomb repulsive interactions which are larger than the electron-hole attraction, giving rise to negative biexciton binding energy.

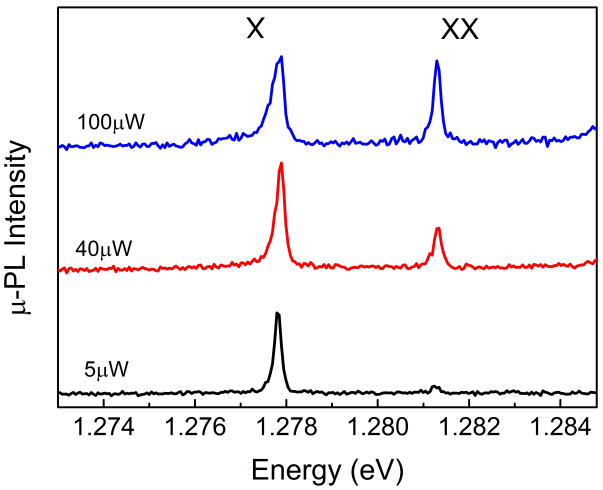

Figure 1.9: Micro PL power dependence spectra from a (211) InAs QD. Due to piezoelectric field, the biexciton line appears at higher energy compared to the exciton one .

This effect is confirmed by the experimental data of this work, and in figure1.9 is depicted the micro-PL spectrum from a single QD, showing the exciton and biexciton emission lines under various excitation powers. At low powers of excitation, the exciton transition dominates as the number of injected carriers in the QD is small and most of them recombine through the first excited state (exciton state). With increasing power of excitation the probability of having simultaneously two e-h pairs in the QD increases non-linearly and the biexciton emission appears vividly. In such power dependent measurements we can have the signature of PZ QDs. In (111) and (211)B InAs/GaAs QDs the internal PZ fields are expected to be in the order of hundreds kV/cm [26], giving rise to large negative biexciton binding energies and opening new perspectives for single photon emitters

as discussed in the next chapters.

High Temperature SPSs.

The high temperature operation of highly efficient Single Photon Sources (SPS's) by electrical injection, can become a reality with InAs PZ QDs, because the energy difference between the exciton and biexciton emission lines is large enough and the two lines can be distinguished even at high temperatures.

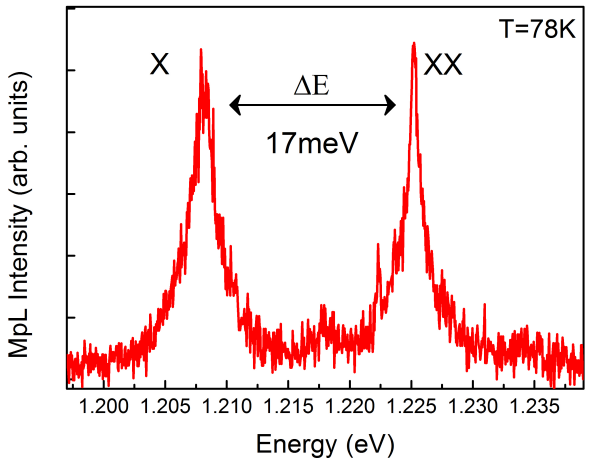

Figure 1.10: Micro-PL spectrum from a single PZ QD, of our sample, showing the large X-XX energy difference. The emission lines of the X and XX do not interfere at all at 80K.

The condition for room temperature SPS operation is to have the energy difference between exciton and biexciton larger than the homogeneous linewidth of exciton's and biexciton's emission lines at that temperature. A typical homogeneous linewidth for a GaAs exciton at room temperature is 10 meV. Moreover the GaAs based systems are well studied and can be easily integrated to electronic circuits, in contradistinction to the Nitride based systems where the PZ fields are much stronger but electrical injection is of serious concern especially when referring

to the GaN/AlN QDs. The results and discussion from a comprehensive PL study of ensemble and single PZ QDs, designed for high temperature operation, accompanied with the corresponding anti-bunching experiments providing evidence for single photon emission up to 150K, is presented in Chapters 3 and 4.

REFERENCES

[1] Y. Arakawa and H. Sakaki. Multidimensional quantum well laser and temperature dependence of its threshold current. *Appl. Phys. Lett.*, 40(11):939–941, 1982.

[2] N. Kirstaedter, N.N. Ledentsov, M. Grundmann, D. Bimberg, V.M. Ustinov, S.S. Ruvimov, M.V. Maximov, P.S. Kop'ev, Zh.I. Alferov, U. Richter, P. Werner, U. Gosele, and J. Heydenreich. Low threshold, large To injection laser emission from (InGa)As quantum dots. *Electron. Lett.*, 30(17):1416, 1994.

[3] G.T. Liu, A. Stintz, H. Li, K.J. Malloy, and L.F. Lester. Extremely low room-temperature threshold current density diode lasers using InAs dots in In0.15Ga0.85As quantum well. *Electron. Lett.*, 35(14):1163, 1999.

[4] A. Zrenner, L. V. Butov, M. Hagn, G. Abstreiter, G. Böhm, and G. Weimann. Quantum dots formed by interface fluctuations in AlAs/GaAs coupled quantum well structures. *Phys. Rev. Lett.*, 72(21):3382–3385, 1994.

[5] J. Y. Marzin, J. M. Gérard, A. Izraël, D. Barrier, and G. Bastard. Photoluminescence of single InAs quantum dots obtained by self-organized growth on GaAs. *Phys. Rev. Lett.*, 73(5):716–719, 1994.

[6] M. Grundmann, J. Christen, N. Ledentsov, J. Böhrer, D. Bimberg, S. Ru-

vimov, , P. Werner, U. Richter, U. Gösele, J. Heydenreich, V. Ustinov, A. Egorov, A. Zhukov, P. Kop'ev, and Zh. Alferov. Ultranarrow Luminescence Lines from Single Quantum Dots. *Phys. Rev. Lett.*, 74(20):4043–4046, 1995.

[7] D. Hessman, P. Castrillo, M.-E. Pistol, C. Pryor, and L. Samuelson. Excited states of individual quantum dots studied by photoluminescence spectroscopy. *Appl. Phys. Lett.*, 69(6):749, 1996.

[8] P Michler, A Kiraz, C Becher, W V Schoenfeld, P M Petroff, L Zhang, E Hu, and A Imamoglu. A quantum dot single-photon turnstile device. *Science*, 290(5500):2282–2285, 2000.

[9] Charles Santori, Matthew Pelton, Glenn Solomon, Yseulte Dale, and Yoshihisa Yamamoto. Triggered single photons from a quantum dot. *Phys. Rev. Lett.*, 86(8):1502–1505, 2001.

[10] Gilles Brassard, Norbert Lütkenhaus, Tal Mor, and Barry C. Sanders. Limitations on practical quantum cryptography. *Phys. Rev. Lett.*, 85(6):1330–1333, 2000.

[11] Edo Waks, Kyo Inoue, Charles Santori, David Fattal, Jelena Vuckovic, Glenn S Solomon, and Yoshihisa Yamamoto. Secure communication: Quantum cryptography with a photon turnstile. *Nature*, 420(6917):762–762, December 2002.

[12] O. Fedorych, C. Kruse, A. Ruban, D. Hommel, G. Bacher, and T. Kümmell. Room temperature single photon emission from an epitaxially grown quantum dot. *Appl. Phys. Lett.*, 100(6):061114, 2012.

[13] Mark J Holmes, Kihyun Choi, Satoshi Kako, Munetaka Arita, and Yasuhiko

Arakawa. Room-Temperature Triggered Single Photon Emission from a III-Nitride Site-Controlled Nanowire Quantum Dot. *Nano Lett.*, 14(2):982–986, February 2014.

[14] Richard P. Mirin. Photon antibunching at high temperature from a single InGaAs/GaAs quantum dot. *Appl. Phys. Lett.*, 84(8):1260–1262, 2004.

[15] X. M. Dou, X. Y. Chang, B. Q. Sun, Y. H. Xiong, Z. C. Niu, S. S. Huang, H. Q. Ni, Y. Du, and J. B. Xia. Single-photon-emitting diode at liquid nitrogen temperature. *Appl. Phys. Lett.*, 93(10):1–4, 2008.

[16] Dirk Bouwmeester, J W Pan, K Mattle, M Eibl, Harald Weinfurter, and a Zeilinger. Experimental quantum teleportation. *Nature*, 390(6660):575–579, 1997.

[17] Oliver Benson, Charles Santori, Matthew Pelton, and Yoshihisa Yamamoto. Regulated and Entangled Photons from a Single Quantum Dot. *Phys. Rev. Lett.*, 84(11):2513–2516, March 2000.

[18] Alain Aspect, Philippe Grangier, and Gérard Roger. Experimental realization of Einstein-Podolsky-Rosen-Bohm Gedankenexperiment: A new violation of Bell's inequalities. *Phys. Rev. Lett.*, 49(2):91–94, 1982.

[19] R. M. Stevenson, R. J. Young, P. Atkinson, K. Cooper, D. a. Ritchie, and a. J. Shields. A semiconductor source of triggered entangled photon pairs. *Nature*, 439(7073):179–182, 2006.

[20] D. Bimberg, E. Stock, a. Lochmann, a. Schliwa, J.a. Tofflinger, W. Unrau, M. Munnix, S. Rodt, V.a. Haisler, a.I. Toropov, a. Bakarov, and a.K. Kalagin. Quantum Dots for Single- and Entangled-Photon Emitters. *IEEE Photonics J.*, 1(1):58–68, June 2009.

[21] Andrei Schliwa, Momme Winkelnkemper, Anatol Lochmann, Erik Stock, and Dieter Bimberg. In(Ga)As/GaAs quantum dots grown on a (111) surface as ideal sources of entangled photon pairs. *Phys. Rev. B - Condens. Matter Mater. Phys.*, 80(16):161307, October 2009.

[22] Ranber Singh and Gabriel Bester. Nanowire quantum dots as an ideal source of entangled photon pairs. *Phys. Rev. Lett.*, 103(6):1–4, August 2009.

[23] Savvas Germanis, Alexios Beveratos, George E. Dialynas, George Deligeorgis, Pavlos G. Savvidis, Zacharias Hatzopoulos, and Nikos T. Pelekanos. Piezoelectric InAs/GaAs quantum dots with reduced fine-structure splitting for the generation of entangled photons. *Phys. Rev. B - Condens. Matter Mater. Phys.*, 86(3):1–10, 2012.

[24] D. A B Miller, D. S. Chemla, T. C. Damen, A. C. Gossard, W. Wiegmann, T. H. Wood, and C. A. Burrus. Band-edge electroabsorption in quantum well structures: The quantum-confined stark effect. *Phys. Rev. Lett.*, 53(22):2173–2176, 1984.

[25] G.E. Dialynas, C. Xenogianni, S. Tsintzos, E. Trichas, P.G. Savvidis, G. Constantinidis, J. Renard, B. Gayral, Z. Hatzopoulos, and N.T. Pelekanos. Antibinding of biexcitons in (211)B InAs/GaAs piezoelectric quantum dots. *Phys. E Low-dimensional Syst. Nanostructures*, 40(6):2113–2115, April 2008.

[26] Gabriel Bester, Xifan Wu, David Vanderbilt, and Alex Zunger. Importance of second-order piezoelectric effects in zinc-blende semiconductors. *Phys. Rev. Lett.*, 96(18):1–4, 2006.

[27] R. Seguin, a. Schliwa, S. Rodt, K. Pötschke, U. W Pohl, and D. Bimberg. Size-Dependent Fine-Structure Splitting in Self-Organized InAs/GaAs Quantum Dots. *Phys. Rev. Lett.*, 95(25):10–13, December 2005.

[28] M. Bayer, G. Ortner, O. Stern, A. Kuther, A. Gorbunov, A. Forchel, P. Hawrylak, S. Fafard, K. Hinzer, T. Reinecke, S. Walck, J. Reithmaier, F. Klopf, and F. Schäfer. Fine structure of neutral and charged excitons in self-assembled In(Ga)As/(Al)GaAs quantum dots. *Phys. Rev. B*, 65(19):1–23, May 2002.

[29] M. Grundmann, O. Stier, and D. Bimberg. InAs/GaAs pyramidal quantum dots: Strain distribution, optical phonons, and electronic structure. *Phys. Rev. B*, 52(16):11969–11981, 1995.

Chapter 2

Fine Structure Splitting in Piezoelectric QDs

2.1 Abstract

In this Chapter we present polarization resolved and anti-bunching measurements on single PZ QDs. The aim is to demonstrate the possibility of PZ QDs to act, not only as a single photon emitters, but also as sources of entangled photon pairs. Polarization-resolved single dot spectroscopy reveals that the exciton Fine Structure Splitting (FSS) in piezoelectric (211)B InAs/GaAs quantum dots, in the vast majority of examined dots, is smaller than 10μeV. These values are significantly reduced compared to as-grown (100)-oriented InAs dots. By time-resolved measurements (TRPL) we confirm the high oscillator strength of these dots, in spite of the internal piezoelectric field, suggesting good quantum efficiency at 4 K comparable with that of (100) InAs/GaAs dots. Last, photon correlation measurements demonstrate single photon emission from exciton levels of these dots. All these features make this intriguing dot system promising for implementing solid-state entangled photon sources.

2.2 Introduction

Quantum information science strongly relies on the efficient generation of "on demand" single and entangled photon sources [1, 2]. In several pioneering experiments [3, 4, 5], entangled photon pairs were obtained using parametric down-conversion [6, 7], which, while easy to implement, suffers from the Poissonian statistics of the emitted photon pairs, leading to multi-pair emission, decreasing thus the fidelity of entanglement [8]. "On demand" entangled photon pairs can be obtained by heralding a 3-photon process [3] or with the detection of several auxiliary photons [9], but both schemes are inefficient in terms of photon pair production probability. Single quantum dots (QDs) have been proposed as sources of "on demand" polarization entangled photon sources [10] by using the radiative decay of two electron-hole pairs trapped in the QD. As mentioned in Chapter 1, the subsequent decay of the biexciton (XX) and exciton (X) states will produce polarization entangled photon pairs, provided that the two possible, Horizontal (H) or Vertical (V), decay paths

$$|H_{xx}\rangle|H_x\rangle \quad \text{or} \quad |V_{xx}\rangle|V_x\rangle \tag{2.1}$$

to the ground state are indistinguishable, which requires that the FSS of the intermediate excitation state is zero.

Then, the emitted two-photon state is a superposition of the two horizontally-polarized and the two vertically-polarized photons, which are produced by the cascade emission to the ground state through the intermediate exciton state, and can be written as follows:

$$\Psi = \frac{1}{\sqrt{2}}(|H_{xx}H_x\rangle + |V_{xx}V_x\rangle). \tag{2.2}$$

Ψ corresponds to an overall unpolarized photon state.

2.3 The importance of the reduced FSS

In actual QDs, due to lateral anisotropies of the dot wave-functions, a fine structure splitting of the intermediate X level arises, rendering the two paths distinguishable and diminishing the entangled photon pair fidelity [11, 12]. Several techniques, using QD annealing [13], in-plane magnetic [14] or electric field [15], perpendicular electric field [16, 17] and biaxial strain [18] have been suggested to reduce or cancel FSS. Moreover, broadening of the X line by Purcell effect has been used to make the two paths indistinguishable [12]. Generation of polarization entangled photons has been reported in the last few years by using one or several of the above techniques [19, 20, 21]. While these techniques are successful, they are hardly scalable, as it is not simple to obtain a QD with FSS below 2μeV, necessary for the generation of high-fidelity entangled photons [12].

Alternatively, it has been proposed recently that QDs grown along polar orientations, such as (111) or (211), are capable of negligible FSS values [22, 23] based on the following considerations. Unlike the (100) dots, where lateral piezoelectric (PZ) fields elongate the electron and hole wave-functions in the growth plane generating thus significant FSS [23] in the case of (111) or (211) dots, the main manifestation of the PZ effect is a strong vertical PZ field ($\leqq$1MV/cm) [24, 25] which does not introduce any lateral wavefunction anisotropy, and hence does not generate FSS. Lateral PZ fields are also present in these orientations, however, they are much weaker and, as shown for (111) dots, they do not generate FSS either, as they preserve the C_{3v} symmetry of the confining potential. We argue that this equally applies to our (211) dots, not only because a (211) surface closely resembles the (111) surface, but in addition due to the large diameter to height aspect ratio

in our dots, minimizing any influence that lateral facets may have in the system. A recent work on (111) InGaAs/GaAs QDs fabricated using droplet epitaxy has indeed shown evidence for reduced FSS values (10-40μeV) [26] although clearly such values are still too large for entanglement applications. On the other hand, another recent report on pyramidal InGaAs QDs grown by metalorganic chemical vapor deposition on pre-patterned (111)B GaAs substrates [27] has reported very small FSS splittings ($\leqq$5μeV, in the majority of dots) as well as evidence for polarization entanglement out of these higher symmetry dots. In this report, we present results on InAs/GaAs QDs grown along the (211)B orientation in the standard Stranski-Krastanow growth mode, which *as-grown* exhibit FSS values smaller than 10μeV, *for over 90% of the dots*, suggesting that (211)B-grown QDs may prove suitable for use in entangled photon sources, without necessitating any pre-patterning or post-processing step.

2.4 Sample and experimental techniques

The sample named as "859" used here contains a single layer of InAs QDs, grown in the middle of a 10nm-thick GaAs/$Al_{0.3}Ga_{0.7}As$ quantum well, about 50nm beneath the sample surface. The QD layer is grown by depositing 1.5 monolayers (MLs) of InAs at 500^{o}C with a growth rate of 0.1ML/s. Under these growth conditions, the InAs dots take the shape of truncated pyramids, with typical QD heights between 2 and 3nm, an aspect ratio larger than 10, and a QD density of $\sim 10^{10} cm^{-2}$ [28]. As an example, figure 2.1(a) presents an atomic force microscopy (AFM) image from an uncapped QD sample grown at exactly the same conditions, the analysis of which reproduces well the above values.

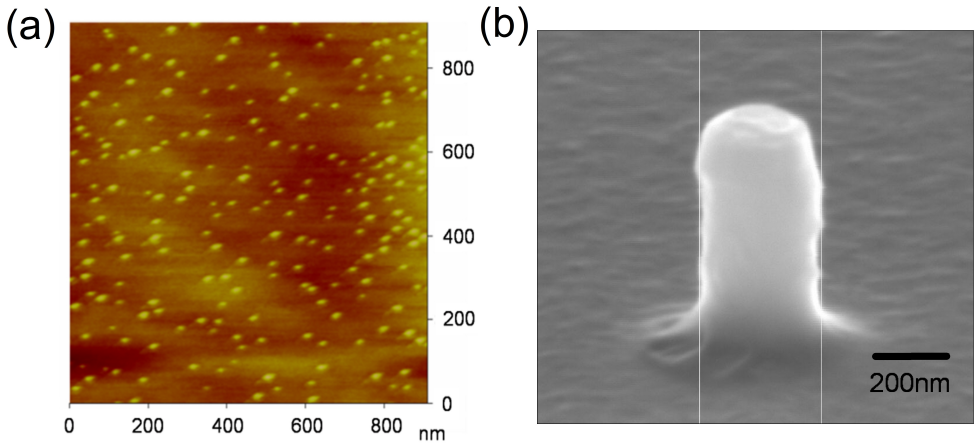

Figure 2.1: (a) AFM image from an uncapped QD layer grown at the same conditions as in the sample used in this work. (b) SEM picture from a typical mesa used for μ-PL experiments.

For single dot spectroscopy, the sample is processed by e-beam lithography into mesas of various diameters (150-500nm), placed more than 15μm apart. A typical mesa is shown in figure2.1(b). A continuous-wave 405nm laser diode is used for the excitation of isolated mesas with a spot size of 2μm. The micro-photoluminescence (μ-PL) signal is dispersed in a 0.75m spectrograph with 1200gr/mm grating and is detected by a Nitrogen-cooled charge-coupled device camera. The sample is cooled down to 5K in a variable temperature continuous-flow helium cryostat. The polarization-resolved spectra are recorded using a fixed linear polarizer in front of the spectrograph and a broadband $\lambda/2$ wave-plate to rotate the polarization as demonstrated in figure 2.2. The exciton lifetime measurements are performed by a TRPL set up attached on a typical μ-setup and is visible in figure 2.2, where a mode-locked Ti:sapphire laser at 780nm with 4ps pulses at 81MHz repetition rate, is used as an excitation source. The laser diode signal from the laser is used to trigger the clock of the time to amplitude converter for the photon correlation measurments performed for the purpose of this Chapter. More information will be given in Chapter 4.

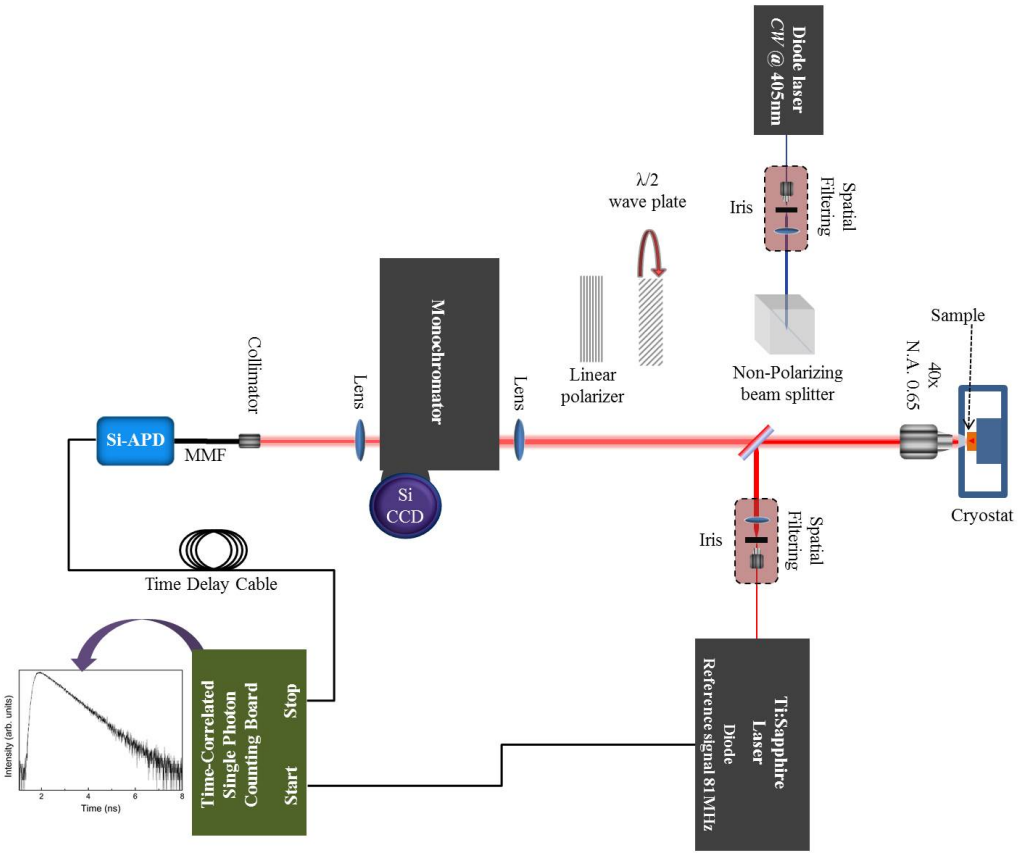

Figure 2.2: A schematic representation of the μ-PL setup combined with TRPL setup for measuring the decay times of the emitting QD states. The polarisation-resolved setup is also schematically presented and can be inserted in the μ-PL setup for polarization measurements.

2.5 Polarization resolved micro PL experiments

2.5.1 The determination of exciton and biexciton lines

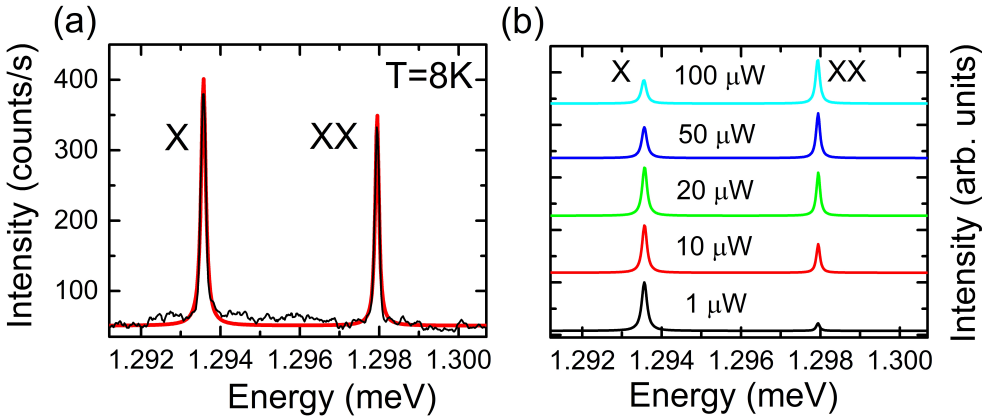

Figure 2.3: (a) μ-PL spectrum from a single (211)B InAs/GaAs QD consisting of an excitonic (X) and a bi-excitonic (XX) peak. Lorentzian fittings of the two peaks are superposed. The intensity axis is given in counts per sec. (b) Power-dependent μ-PL spectra from the same QD, demonstrating the strongly nonlinear character of the XX line. The spectra are upshifted for clarity and normalized to the maximum peak.

In figure 2.3(a) is presented a characteristic μ-PL spectrum from a single (211)B InAs/GaAs QD. It consists of two lines, labeled as exciton (X) and biexciton (XX). The two peaks are identified as exciton and bi-exciton, based on their linear and quadratic power dependence, respectively, at low excitation powers. The related power dependent spectra demonstrating the strongly nonlinear character of the XX line are depicted in figure 2.3(b). In fact, the intensity of X scales at low powers as $\sim P^{0.98}$, whereas that of XX as $\sim P^{1.8}$. The energy difference between the XX and X lines is $\sim$4.4meV in this QD, with the XX line appearing characteristically at higher energy as a manifestation of the large PZ field inside the dots, expected to be several hundreds of kV/cm based on our own measurements. [25].

Alternative assignments for the two lines involving charged excitons can be

easily ruled out, based on the observed power dependence and the fact that in undoped QD systems as ours, charged excitons are typically observed as additional lines to the neutral exciton ones. For instance, the possibility to interpret the XX line as due to a charged exciton can be excluded, not only based on its near quadratic power dependence, but also on the fact that in such case a third *distinct* bi-excitonic line would be expected at the exciton saturation excitation levels, which is not observed in our dots. Moreover, for the particular dot discussed in figure2.4, showing a sizable FSS ($> 10\mu eV$), if either or both of the lines were due to charged excitons, they should not exhibit any linear polarization splitting [29], unlike the experimental findings of figure 2.4.

2.5.2 The determination of FSS values in PZ QDs

To determine FSS in (211)B InAs/GaAs QDs, we performed polarization dependent μ-PL on 20 different single dots of the sample. Here, it must be pointed out that taking into account the instrument's spectral resolution and the typical exciton line-widths of 100μeV, the resolving power of this set-up using standard de-convolution procedure is estimated to be $\sim$10μeV. One can further improve the precision of the FSS measurement beyond this 10μeV limit, by applying the method of ref. [13], i.e. utilizing Lorentzian fittings to determine the energies of the exciton (X) and biexciton (XX) peaks, and subsequently fitting the XX-X energy difference versus polarization angle by a sinusoidal function, where applicable. Among the 20 examined QDs, only two have shown FSS larger than our resolving power of 10μeV.

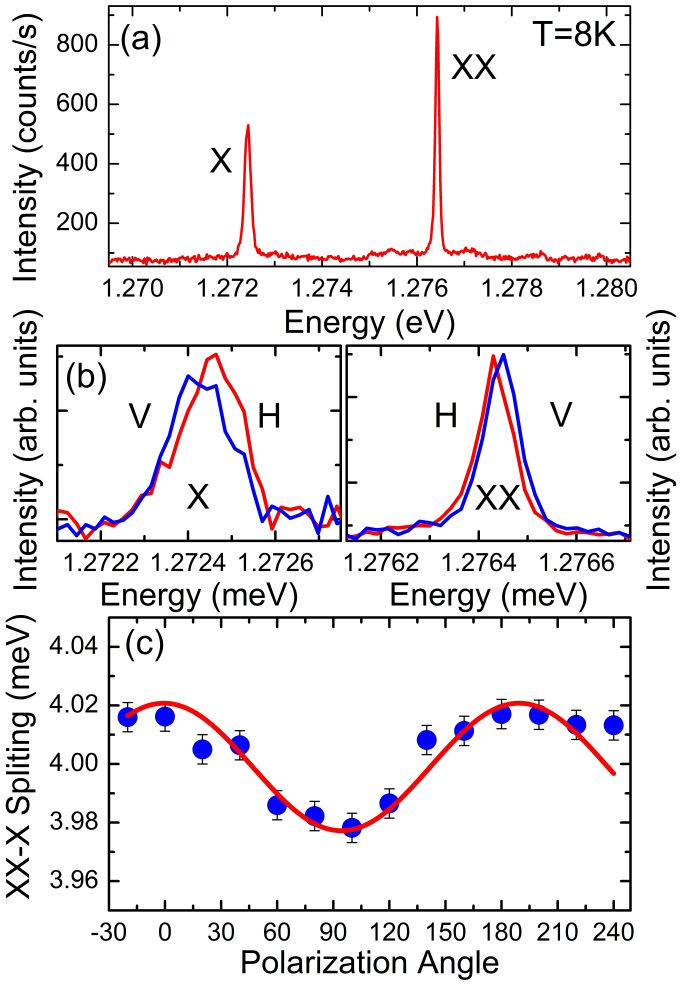

Figure 2.4: (a) μ-PL spectrum from a (211)B InAs/GaAs QD with sizable FSS, consisting of the characteristic exciton (X) and bi-exciton (XX) peaks. (b) Polarization-resolved emission from the X and XX lines of same dot. (c) XX-X energy splitting as a function of polarization angle, showing characteristic periodicity. The extracted FSS for this QD is 20μeV.

One such case is shown in figure 2.4, where the X and XX emission lines of figure2.4(a) are analyzed in terms of linear polarization in figure2.4(b). We observe that while the intensity of the lines remains practically intact, their energy positions vary periodically with polarizer angle, shifting in opposite directions. By extracting the energy positions by Lorentzian fittings, the XX-X energy difference

is plotted in figure 2.42(c) as a function of polarizer angle, exhibiting the characteristic sinusoidal periodicity of 180°. From the max-min energy difference, we deduce that the FSS in this QD is 20μeV. However, as previously mentioned, 90% of the dots tested in this work have shown FSS below 10μeV.

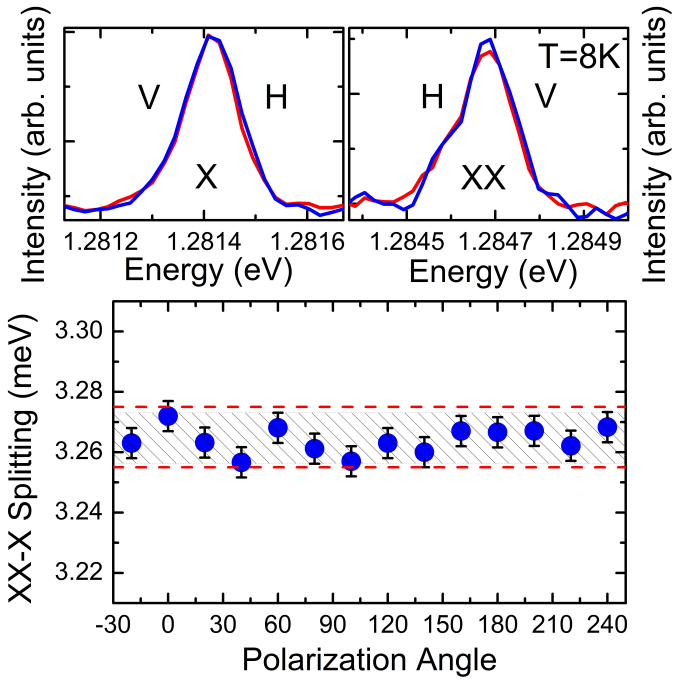

Figure 2.5: *Top*: Polarization-resolved emission from the X and XX lines of a typical (211)B InAs/GaAs QD, exhibiting very weak polarization dependence. *Bottom*: XX-X energy splitting as a function of polarization angle, showing no obvious periodicity. All points lie within the 20eV-wide shaded zone, implying that the FSS is less than 10μeV.

A typical example is depicted on the top panel of figure2.5, where the X and XX lines of another dot appear nearly completely insensitive to polarization. The extracted XX-X energy difference is plotted as a function of polarizer angle on the bottom panel of figure 2.5, showing no obvious sinusoidal behavior. However, all data points lie within the 20μeV shaded zone, clearly suggesting that the FSS of this dot is smaller than 10μeV. Similar behavior has been observed for 90% of the

examined dots.

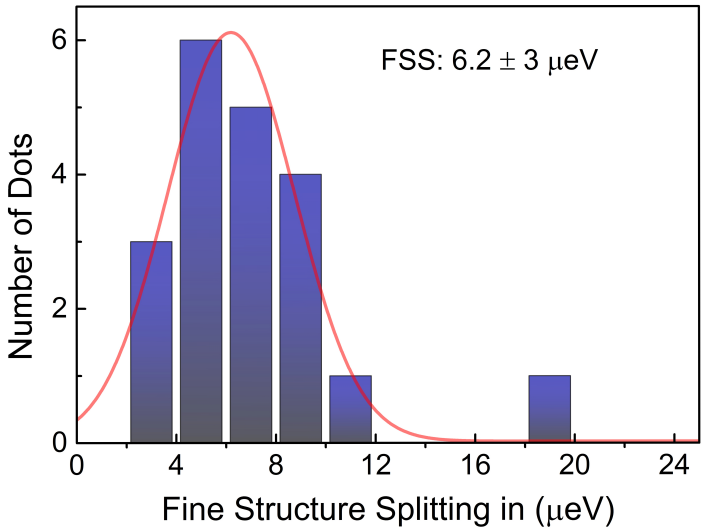

Figure 2.6: Statistical distribution of the FSS values fitted with a Gaussian along with mean and full width half maximum values.

In order to assign an FSS value to all our dots, we subtract the XX-X energy difference values at 0° and 90° polarization angle and divide by two. The thus obtained FSS values are plotted in the histogram of figure 2.6, confirming that only 10% of the QDs exhibit a splitting larger than 10μeV. By assuming a gaussian distribution, we obtain a mean FSS of 6.2 $\pm$3μeV. This is to be compared to FSS values of several tens of μeV for as-grown (100) InAs/GaAs QDs, [13] which can be reduced to less than 10μeV only when annealing is applied to specific dots [30].

2.5.3 Time resolve photoluminescence measurments

Negligible FSS is not a sufficient condition to make the (211)B InAs/GaAs QDs a good candidate for the generation of entangled photon pairs. It is necessary that these QDs exhibit purely radiative decay and single photon emission. We investigated both properties under pulsed excitation in a time-resolved μ-PL set-up. Figure2.7(a) depicts the PL decay curves obtained at 5K from the X line of a

single dot emitting at 1.2778 eV for three different excitation powers. By fitting the decay curves at long times with a single exponential, we extract a lifetime of ≈2 ns, independent of the pump power as expected for QD emission. This lifetime is comparable to the ones observed in (100) InAs/GaAs QDs emitting in the same energy range [31, 32], Ulrich2005. Specifically, Karachinsky et al [31]. reported a 2ns lifetime for InAs dots emitting at 1.30eV, Bardot et al. [32], 1.55ns for dots emitting at 1.29eV, and Ulrich et al. [33], 1ns at 1.34eV. This demonstrates the still high oscillator strength and quantum efficiency of the (211) dots in spite of the large PZ field which can be as high as ≈1 MV/cm, and which is expected to reduce the oscillator strength and increase the radiative lifetime by quantum confined Stark effect (QCSE).

In order to understand this important point, we plot in figure 2.7(b) the calculated ratios of radiative lifetimes in (211) and (100) QDs as a function of QD height, *with* or *without* a PZ field of 1MV/cm in the (211) dots, assuming a one-dimensional (1D) Schrödinger equation model and calculating the electron-hole wavefunction overlap integrals in the envelope function approximation. Strain effects on the band alignment and the effective mass dependence on growth direction have been taken into account. The 1D simplification is justified in our case by the large aspect ratio of the QDs, implying that quantum confinement along the growth direction is much stronger compared to the lateral directions. For zero field, the lifetime ratio is practically constant and close to unity, while for the 1MV/cm PZ field, the ratio increasingly deviates from unity with increasing QD height, in accordance to QCSE. However, for QD heights between 2-3 nm, which are the actual heights of our dots, the lifetime ratio barely exceeds unity by only 10-30%, accounting for the relatively short lifetimes observed in our experiments.

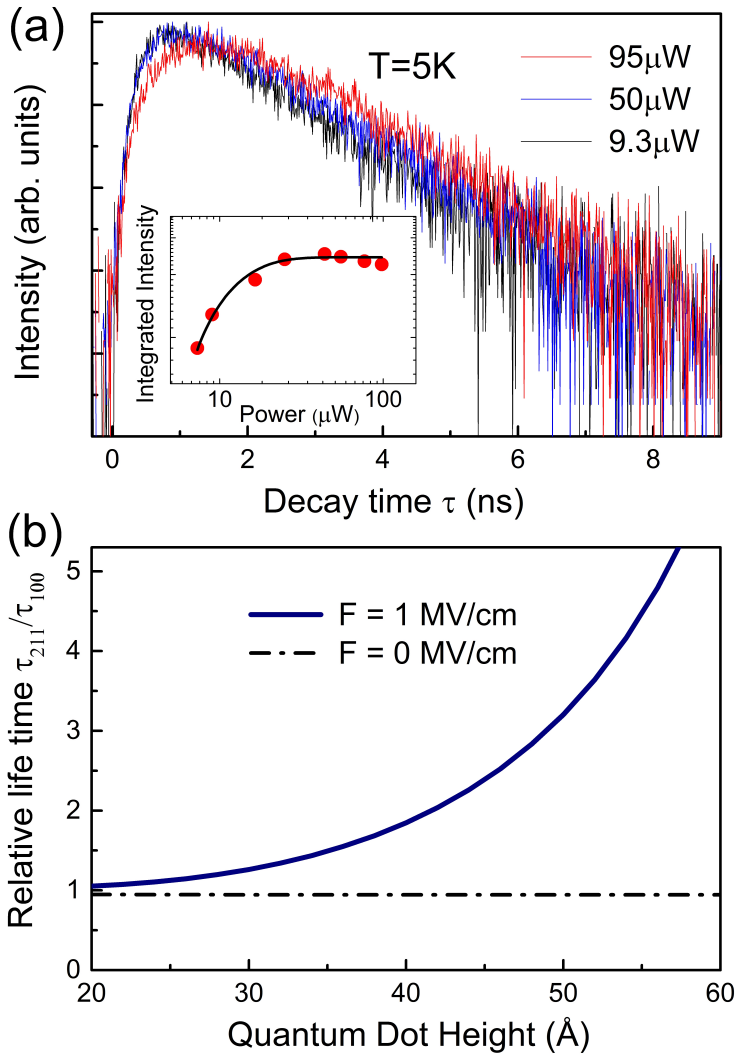

Figure 2.7: (a) Time-decay curves of the X line of a single (211)B InAs QD as a function of excitation power. The inset shows the time-integrated PL intensity versus power, marking a clear saturation regime in this power range. (b) Calculated ratio of radiative lifetimes in (211) and (100) QDs as a function of QD height, with or without a PZ field of 1MV/cm in the (211) dots.

Coming back to figure 2.7(a), the prolonged rise-time observed in the PL decay curve for 95μW is attributed to state filling and subsequent cascade from higher excited dot levels [34]. The same state-filling effects are responsible for the strong

saturation of the PL intensity, depicted in the inset of figure 2.7(a). Note that both the 2ns lifetime and the observation of state filling constitute an indirect proof of the high optical quality of the (211) InAs/GaAs QDs, equivalent to their well-known (100) counterparts.

2.5.4 Photon correlation measurements

Here is presented the single photon emission behaviour as a direct proof of the single exciton nature of the investigated QD.

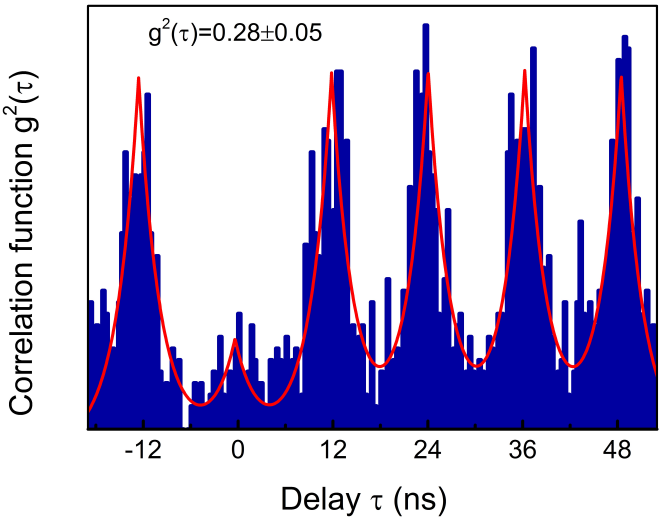

Figure 2.8: Second-order correlation function $g^2(\tau)$ obtained with 27μW pump power demonstrating clear anti-bunching behaviour characteristic of single photon emission.

The experiment was performed in a typical Hanbury-Brown-Twiss (HBT) setup [35]. More informations about the anti-bunching measurements and HBT μ-PL setup are given in Chapter 4. The two avalanche photodiodes were APD EG&G Model SPCM-AQR 13 [36]. Each APD is placed after a monochromator, spectrally filtering the X line, to avoid optical cross-talk [37]. The same single dot of figure2.7(a) is pumped with a power of 27 μW, i.e. just below saturation, in

order to maximize the photon count rate. The count rates were 6500 and 9000 counts per second (cps) on each APD with a background of 2500 and 4000 cps, respectively, measured next to the X line. The background arises from emission in a doped buffer layer of the sample, but also from stray light on the APDs ($\approx$ 1000 cps). Figure 2.8 shows the raw second order autocorrelation function $g^2(\tau)$ of the X line, after integration of 3600sec. At each repetition of the laser pulse we observe a correlation peak, the area under which normalizes to A(τ)=1$\pm$0.05 [36]. At τ=0, however, we observe absence of coincidences, signature of single photon emission from the dot under investigation. The normalized area of the τ=0 peak is A(τ)=0.28$\pm$0.05, which is less than 0.5, satisfying the criterion for single photon emission. Note that the $g^2(\tau)$ function has not been corrected for any background, and the relatively poor value of A(τ=0) is mostly due to the excess of background radiation.

2.6 Conclusions

In conclusion, we have shown that (211) InAs/GaAs QDs are good candidates for the implementation of compact entangled photon sources. We have demonstrated that the mean FSS splitting of these dots *as-grown* is below 10μeV. In addition, we have shown that their lifetimes are very similar to their (100) counterparts, and that they are capable of single photon emission.

REFERENCES

[1] Lov K. Grover. Quantum Mechanics helps in searching for a needle in a haystack. *Phys. Rev. Lett.*, 79(2):4, 1997.

[2] Peter W. Shor. Polynomial-Time Algorithms for Prime Factorization and Discrete Logarithms on a Quantum Computer. *Int. J. Theor. Phys.*, 26(5):26, 1997.

[3] Jian-Wei Pan, Dik Bouwmeester, Harald Weinfurter, and Anton Zeilinger. Experimental Entanglement Swapping: Entangling Photons That Never Interacted. *Phys. Rev. Lett.*, 80(18):3891–3894, 1998.

[4] Robert Prevedel, Philip Walther, Felix Tiefenbacher, Pascal Böhi, Rainer Kaltenbaek, Thomas Jennewein, and Anton Zeilinger. High-speed linear optics quantum computing using active feed-forward. *Nature*, 445(7123):65–69, January 2007.

[5] Matthaeus Halder, Alexios Beveratos, Nicolas Gisin, Valerio Scarani, Christoph Simon, and Hugo Zbinden. Entangling Independent Photons by Time Measurement. *Nat. Phys.*, 3(October):13, 2007.

[6] Z. Y. Ou and L. Mandel. Observation of spatial quantum beating with separated photodetectors. *Phys. Rev. Lett.*, 61(1):54–57, 1988.

[7] Paul Kwiat, Klaus Mattle, Harald Weinfurter, Anton Zeilinger, Alexander Sergienko, and Yanhua Shih. New High-Intensity Source of Polarization-Entangled Photon Pairs. *Phys. Rev. Lett.*, 75(24):4337–4341, 1995.

[8] V. Scarani, H. De Riedmatten, I. Marcikic, H. Zbinden, and N. Gisin. Four-photon correction in two-photon Bell experiments. *Eur. Phys. J. D*, 32(1):129–138, November 2005.

[9] Stefanie Barz, Gunther Cronenberg, Anton Zeilinger, and Philip Walther. Heralded generation of entangled photon pairs. *Nat. Photonics*, 4(August):553–556, 2010.

[10] Oliver Benson, Charles Santori, Matthew Pelton, and Yoshihisa Yamamoto. Regulated and Entangled Photons from a Single Quantum Dot. *Phys. Rev. Lett.*, 84(11):2513–2516, March 2000.

[11] T. M. Stace, G. J. Milburn, and C. H. W. Barnes. An entangled two photon source using biexciton emission of an asymmetric quantum dot in a cavity. *Phys. Rev. B. Condens. Matter*, 67(8):16, 2002.

[12] Matthieu Larqué, Isabelle Robert-Philip, and Alexios Beveratos. Bell inequalities and density matrix for polarization-entangled photons out of a two-photon cascade in a single quantum dot. *Phys. Rev. A - At. Mol. Opt. Phys.*, 77(4):042118, 2008.

[13] R. J. Young, R. M. Stevenson, a. J. Shields, P. Atkinson, K. Cooper, D. a. Ritchie, K. M. Groom, a. I. Tartakovskii, and M. S. Skolnick. Inversion of exciton level splitting in quantum dots. *Phys. Rev. B*, 72(11):1–4, September 2005.

[14] M. Bayer, G. Ortner, O. Stern, A. Kuther, A. Gorbunov, A. Forchel, P. Hawrylak, S. Fafard, K. Hinzer, T. Reinecke, S. Walck, J. Reithmaier,

F. Klopf, and F. Schäfer. Fine structure of neutral and charged excitons in self-assembled In(Ga)As/(Al)GaAs quantum dots. *Phys. Rev. B*, 65(19):1–23, May 2002.

[15] K. Kowalik, O. Krebs, A. Lemaître, S. Laurent, P. Senellart, P. Voisin, and J. a. Gaj. Influence of an in-plane electric field on exciton fine structure in InAs-GaAs self-assembled quantum dots. *Appl. Phys. Lett.*, 86(4):15–18, 2005.

[16] A. J. Bennett, M. A. Pooley, R. M. Stevenson, M. B. Ward, R. B. Patel, A. Boyer de la Giroday, N. Sköld, I. Farrer, C. A. Nicoll, D. A. Ritchie, and A. J. Shields. Electric-field-induced coherent coupling of the exciton states in a single quantum dot. *Nat. Phys.*, 6(October):947–950, 2010.

[17] J. D. Plumhof, V. Kápek, F. Ding, K. D. Jöns, R. Hafenbrak, P. Klenovský, A. Herklotz, K. Dörr, P. Michler, A. Rastelli, and O. G. Schmidt. Strain-induced anticrossing of bright exciton levels in single self-assembled GaAs/AlxGa1-xAs and InxGa 1-xAs/GaAs quantum dots. *Phys. Rev. B - Condens. Matter Mater. Phys.*, 83(12):1–4, 2011.

[18] Mohsen Ghali, Keita Ohtani, Yuzo Ohno, and Hideo Ohno. Generation and control of polarization-entangled photons from GaAs island quantum dots by an electric field. *Nat. Commun.*, 3:661, 2012.

[19] Adrien Dousse, Jan Suffczyski, Alexios Beveratos, Olivier Krebs, Aristide Lemaître, Isabelle Sagnes, Jacqueline Bloch, Paul Voisin, and Pascale Senellart. Ultrabright source of entangled photon pairs. *Nature*, 466(7303):217–220, July 2010.

[20] R M Stevenson, R J Young, P Atkinson, K Cooper, D a Ritchie, and a J

Shields. A semiconductor source of triggered entangled photon pairs. *Nature*, 439(7073):179–182, January 2006.

[21] N. Akopian, N. H. Lindner, E. Poem, Y. Berlatzky, J. Avron, D. Gershoni, B. D. Gerardot, and P. M. Petroff. Entangled photon pairs from semiconductor quantum dots. *Phys. Rev. Lett.*, 96(13):7–10, April 2006.

[22] Ranber Singh and Gabriel Bester. Nanowire quantum dots as an ideal source of entangled photon pairs. *Phys. Rev. Lett.*, 103(6):1–4, 2009.

[23] Andrei Schliwa, Momme Winkelnkemper, Anatol Lochmann, Erik Stock, and Dieter Bimberg. In(Ga)As/GaAs quantum dots grown on a (111) surface as ideal sources of entangled photon pairs. *Phys. Rev. B - Condens. Matter Mater. Phys.*, 80(16):161307, October 2009.

[24] Gabriel Bester, Xifan Wu, David Vanderbilt, and Alex Zunger. Importance of second-order piezoelectric effects in zinc-blende semiconductors. *Phys. Rev. Lett.*, 96(18):1–4, 2006.

[25] G. E. Dialynas, N. Chatzidimitriou, S. Kalliakos, S. Tsintzos, P. G. Savvidis, Z. Hatzopoulos, and N. T. Pelekanos. Single dot spectroscopy on InAs/GaAs piezoelectric quantum dots. *Phys. Status Solidi Appl. Mater. Sci.*, 205(11):2566–2568, November 2008.

[26] Erik Stock, Till Warming, Irina Ostapenko, Sven Rodt, Andrei Schliwa, Jan Amaru Töfflinger, Anatol Lochmann, Aleksandr I. Toropov, Sergej a. Moshchenko, Dimitry V. Dmitriev, Vladimir a. Haisler, and Dieter Bimberg. Single-photon emission from InGaAs quantum dots grown on (111) GaAs. *Appl. Phys. Lett.*, 96(9):093112, 2010.

[27] A. Mohan, M. Felici, P. Gallo, B. Dwir, A. Rudra, J. Faist, and E. Kapon.

Polarizattion-entangled photons produced with high-symmetry site-controlled quantum dots. *Nat. Photonics*, 4:202–306, March 2010.

[28] G. E. Dialynas, S. Kalliakos, C. Xenogianni, M. Androulidaki, T. Kehagias, P. Komninou, P. G. Savvidis, Z. Hatzopoulos, and N. T. Pelekanos. Piezoelectric InAs (211)B quantum dots grown by molecular beam epitaxy: Structural and optical properties. *J. Appl. Phys.*, 108(10):103525, 2010.

[29] Gustavo a. Narvaez, Gabriel Bester, and Alex Zunger. Excitons, biexcitons, and trions in self-assembled (In,Ga)As GaAs quantum dots: Recombination energies, polarization, and radiative lifetimes versus dot height. *Phys. Rev. B - Condens. Matter Mater. Phys.*, 72(24):245318, 2005.

[30] D. J P Ellis, R. M. Stevenson, R. J. Young, a. J. Shields, P. Atkinson, and D. a. Ritchie. Control of fine-structure splitting of individual InAs quantum dots by rapid thermal annealing. *Appl. Phys. Lett.*, 90(1):011907, 2007.

[31] L. Ya Karachinsky, S. Pellegrini, G. S. Buller, a. S. Shkolnik, N. Yu Gordeev, V. P. Evtikhiev, and V. B. Novikov. Time-resolved photoluminescence measurements of InAs self-assembled quantum dots grown on misorientated substrates. *Appl. Phys. Lett.*, 84(1):7–9, 2004.

[32] C. Bardot, M. Schwab, M. Bayer, S. Fafard, Z. Wasilewski, and P. Hawrylak. Exciton lifetime in InAs/GaAs quantum dot molecules. *Phys. Rev. B - Condens. Matter Mater. Phys.*, 72(3):035314, 2005.

[33] S. M. Ulrich, M. Benyoucef, P. Michler, N. Baer, P. Gartner, F. Jahnke, M. Schwab, H. Kurtze, M. Bayer, S. Fafard, Z. Wasilewski, and A. Forchel. Correlated photon-pair emission from a charged single quantum dot. *Phys. Rev. B - Condens. Matter Mater. Phys.*, 71(23):235328, 2005.

[34] Charles Santori, Glenn S. Solomon, Matthew Pelton, and Yoshihisa Yamamoto. Time-resolved spectroscopy of multi-excitonic decay in an InAs quantum dot. *Phys. Rev. B - Condens. Matter Mater. Phys.*, 65(7):073310, 2001.

[35] R. Hambury Brown and R. Q. Twiss. Correlation between photons in two coherent beams of light. *Nature*, 177(4497):27, 1956.

[36] a. Beveratos, S. Kühn, R. Brouri, T. Gacoin, J. P. Poizat, and P. Grangier. Room temperature stable single-photon source. *Eur. Phys. J. D*, 18(2):191–196, February 2002.

[37] Christian Kurtsiefer, Patrick Zarda, Sonja Mayer, and Harald Weinfurter. The breakdown flash of Silicon Avalance Photodiodes - backdoor for eavesdropper attacks? *J. Mod. Opt.*, 48(13):2039–2047, 2001.

Chapter 3

Piezoelectric QDs for High Temperature Operation

3.1 Abstract

In the first section of this chapter the carrier dynamics in self-assembled (211)B InAs quantum dots (QDs), grown by Stranski-Krastanow method has been investigated by time-resolved and temperature-dependent photoluminescence experiments. The radiative recombination times are found to be larger than 1.7ns and remain practically constant with temperature, in line with the zero degree of dimensionality of the system. Above 100K, the decay time is dominated by non-radiative channels. The main activation mechanism for non-radiative recombination is associated with carrier escape from the quantum dots to the wetting layer. In the second section of this chapter some important results on band-gap engineered InAs/GaAs QDs are discussed, where the QD and wetting layer transition energy difference is apropriate increase , resulting in higher activation.

3.2 Introduction: The key to success.

A sustainable source of "on demand" single and entangled photons operating at high temperatures would represent a vital step towards realistic quantum communication and quantum computation technologies [1, 2, 3]. Even though single photon emission at high temperatures has been demonstrated on systems such as molecules [4], color centers in diamonds [5], nano-crystals [6], and as-grown QDs [7, 8, 9], these demonstrations relied exclusively on optical pumping schemes. On the other hand, single or entangled photons emitted from self-assembled QDs under electrical injection, have already been demonstrated at low temperatures [10, 11].

As discussed in Chapter 1, piezoelectric QDs offer concrete advantages for single or entangled photon sources at elevated temperatures. The main arguments are that: they are capable of large exciton biexciton splittings, favoring single photon emission at elevated temperatures [8]. Secondly, as proposed recently [12, 13], piezoelectric QDs are capable of negligible fine structure splitting (FSS) values of the exciton state, as a prerequisite for efficient generation of entangled photon pairs. The case of InAs QDs grown on (211)B GaAs substrates [14] is a good example of a piezoelectric QD system which is technologically exploitable. As previously shown, the (211)B InAs QDs carry a strong internal piezoelectric (PZ) field that can be as high as 1MV/cm [15], exhibit ultra-small FSS values in as-grown QDs [16, 17], and are capable of large exciton to biexciton splittings, in excess of 10meV depending on the QD size and or PZ field. All these features make the (211)B InAs QDs attractive for entanglement as well as practical single photon emitter applications at high temperatures. Towards this end, the next two sections will discuss the recombination dynamics of this interesting PZ QD system, accompanied by a comprehensive study on the origins of non-radiative

mechanism by resolving the activation energies of InAs QDs either on GaAs or on xÅGaAs/yÅAlAs pseudo-alloy layer.

3.3 Recombination Dynamics in (211)B QDs

The PZ QD samples are grown by molecular beam epitaxy on (211)B semi-insulating GaAs substrates. Initially, a thin GaAs buffer layer is grown at 620^0C, followed by a 40 period (23Å GaAs/15Å AlAs) super lattice (SL), which is meant to smooth out any irregularity of the high index substrate and provide a high quality surface for the QD nucleation. The QD layer is then typically grown at 480^0C on a 10 nm GaAs layer following the SL, with a growth rate of 0.1ML/s. Under these conditions, the QDs take the shape of truncated pyramids, with typical heights of 2-3nm, and a relative large aspect ratio of > 5, as detected by AFM [14]. Next, the QDs are capped by a 30 nm GaAs layer which is grown by ramping up the temperature to 620^0C, or they are left uncapped for Atomic Force Microscopy (AFM) characterisation. For photoluminescence (PL) experiments, a He-Cd continuous wave (*cw*) laser at 325nm is used and the sample is fixed on the cold finger of a variable-temperature closed-circuit helium cryostat. The signal is analyzed using a 0.5m spectrograph equipped with a 150gr/mm grating and is detected by a liquid Nitrogen-cooled charge-coupled device (CCD) camera. For the single QD (SQD) experiments, the samples are processed by standard e-beam lithography into mesas with diameters varying from 150nm to 500nm and every mesa isolated from the next neighbour by 15μm free space. For the excitation of SQDs, a *cw* 405nm laser diode beam is focused down using an 40x objective, with a numerical aperture of 0.65. The micro-PL (μ-PL) signal is collected through the same path using a beam splitter, which is analyzed using a 0.75m spectrograph equipped with a 1200 gr/mm grating, blazed at 750nm, and is detected by a high quantum

efficiency back-thinned liquid Nitrogen-cooled CCD camera. The time-resolved PL (TRPL) experiments are performed using a Hamamatsu streak camera set-up equipped with an InGaAs photocathode and is attached to the monochromator for the spectral filtering excited using a mode locked Ti:Sapphire laser at 780 nm with a pulse width of 4ps and repetition rate of 80MHz.

3.3.1 PL and TRPL study from PZ QDs on GaAs

Before proceeding with the optical characterisation and properties of the sample, it is useful mentioning some structural properties as they are depicted on figure 3.1(a), which shows an AFM image, from an uncapped QD sample, showing the formation of uniform QDs on a smooth (211)B surface, with no aggregates or dashes.

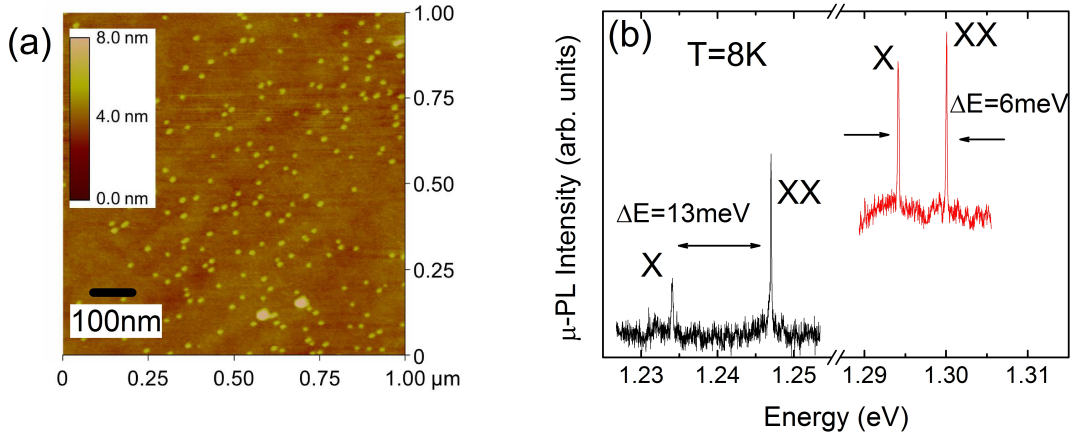

Figure 3.1: (a) AFM image from a sample with (211)B InAs QDs on the surface. (b) Characteristic μ-PL spectra from single PZ QDs having the biexciton (XX) lines at higher energies compared to the exciton (X) lines.

From the analysis of the AFM image the QD heights are measured in the range of 2-3 nm with base diameters between 28-35 nm and the QD density is about 1.8×10^{10}cm^{-2}. At this point, it is important to note that we performed

work towards reducing the QD density, down to values, as low as $10^9 cm^{-2}$, in order to facilitate the isolation of SQDs by standard e-beam lithography. The characteristic μ-PL spectra from single PZ QDs, contained in sub-micron nano-mesas are depicted in figure 3.1(b). In either spectra, the two lines corresponding to exciton and biexciton emission are labelled as X and XX, respectively. The nature of these lines are identified by their linear and quadratic power dependence at lower power levels. Moreover the absence of additional peaks in the spectra, rules out the possibility of emission from charged states. Taking into account the QD emitting at 1.3eV, the X and XX line-widths are 160 and 130 μeV, respectively, whereas for the QD emitting at 1.24 eV, the respective values are 270 and 170μeV. The energy difference between the X and XX emission lines in the presented QDs are 6 and 13meV, respectively, values which hold promise for the discreteness of the two lines even at elevated temperatures, in spite of thermal broadening effects.

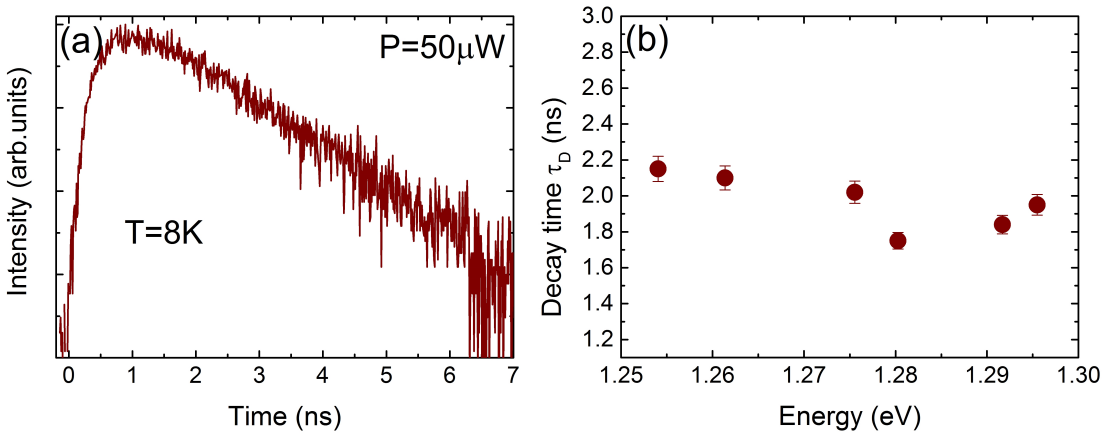

Figure 3.2: (a) Time decay curve from a SQD exciton line suggesting a lifetime of 2ns. (b) Exciton lifetimes extracted for SQDs emitting at different energies.

The ability of the (211)B InAs QDs to act as single photon emitters was previously demonstrated, by observing a pronounced anti-bunching at zero delay, from the exciton emission line of a SQD at T=5K [16]. A characteristic exciton

decay curve, obtained from a single QD, is shown in figure3.2(a), where the decay curve is fitted with the following equation (3.1).

$$I = I_0\left[exp(\frac{-\tau}{\tau_D})\right]. \tag{3.1}$$

The I_0 is the intensity at τ=0 whereas the τ_D is the decay time. In this case, the exciton lifetime is found to be about 2ns, and is independent of the excitation power below or just above the saturation level. Very similar values in the range of 1.8-2.2 ns, were also obtained on several other SQDs studied. They are plotted in figure 3.2(b), as a function of emission energy, suggesting a rather weak size dependence. These values are not very different from the lifetimes encountered in non-piezoelectric (100) InAs QDs, despite the potentially large PZ field in the dots discussed here. This, can be attributed, to the small height of the emitting QDs in our system, which minimizes the influence of the PZ field, in separating the carrier wave-functions and increasing the lifetime. Finally, we note that both the power independence of the lifetime, as well as the prolonged rise-time observed with increasing power [16], attributed to state filling effects, are both consistent with the picture that the low temperature recombination dynamics of single quantum dots is dominated by purely radiative effects.

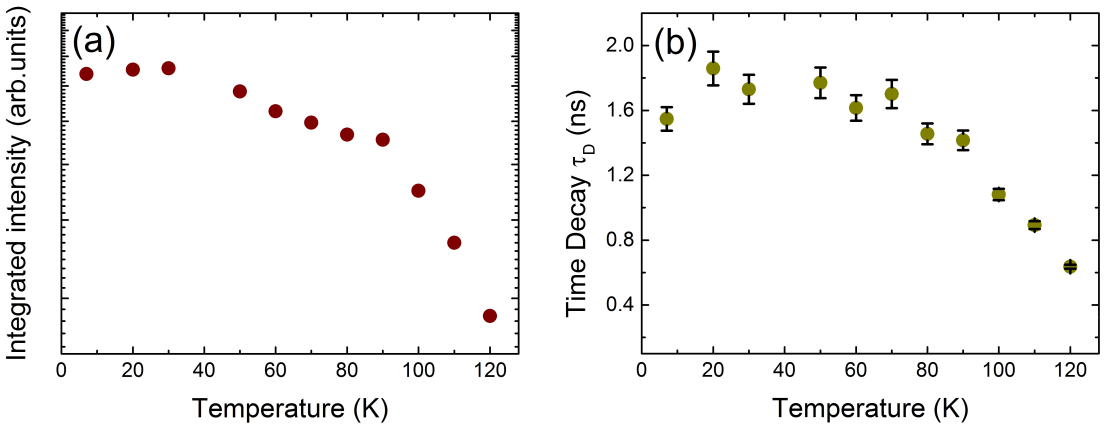

Figure 3.3: (a) Spectrally integrated PL intensity, and (b) PL time decay versus temperature from (211)B InAs QDs.

Towards the direction of developing practical single photon emitters, we need to understand the mechanisms that govern the recombination dynamics in a PZ QD at elevated temperatures. Thus, we performed temperature-dependent TRPL experiments, using a streak camera set-up. Figure 3.3(a) and (b) shows the spectrally integrated PL intensities and the corresponding time decays from ensemble of QDs, taking into account a spectral window of 10nm, around the PL maximum, which is shifted corresponding to PL maxima, at their respective temperatures. It is very clear from the figure that below ∼80K, the decay time remains constant around (1.7±0.1)ns, which is a value comparable to those measured on single QDs, suggesting that the low temperature decay times are mainly of radiative nature. However above ∼90K, we observe a significant decrease of both the PL intensities and the decay times, underlining the fact that non-radiative channels begin to take over at these temperatures.

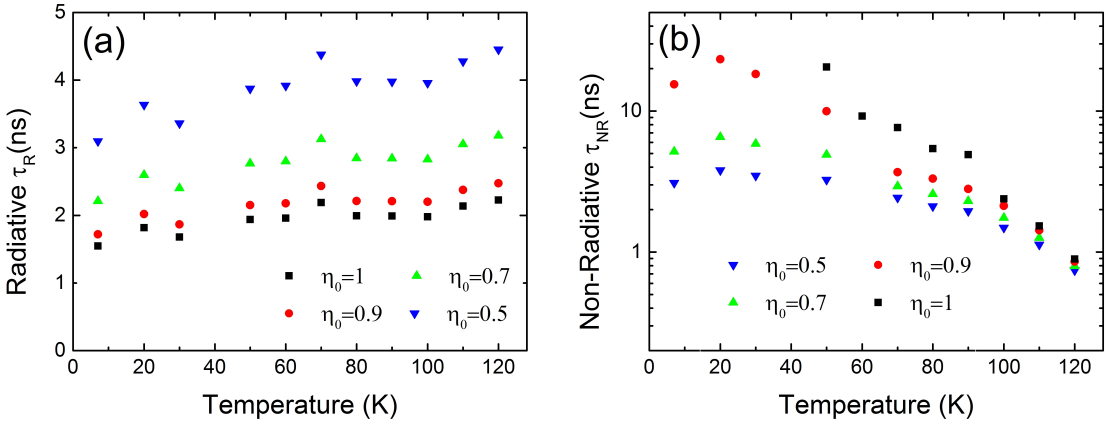

Figure 3.4: (a) Extracted radiative times versus temperature for different values of η_o, confirming the 0D character of QDs. (b) Non-Radiative times, for different values of η_o, dominate the PL decay above 80K.

Following the standard temperature-dependent TRPL analysis as described in [18, 19] and references therein, the measured time decay τ_{D} at every temperature T is related to radiative τ_{R} and non-radiative τ_{NR} recombination times as follows.

$$\frac{1}{\tau_D(T)} = \frac{1}{\tau_R(T)} + \frac{1}{\tau_{NR}(T)}. \tag{3.2}$$

In the following analysis, we tacitly make the assumption that the thermalization processes are much faster than the recombination ones (radiative or non-radiative), meaning that the carriers are in thermal equilibrium. The temperature dependence of the integrated PL intensity $\mathrm{I_{PL}(T)}$ can be expressed as

$$I_{PL} = I_0 \frac{\tau_D(T)}{\tau_R(T)} = I_0 \eta(T). \tag{3.3}$$

Where $\eta(T)$ is the radiative efficiency at a given temperature T and $\mathrm{I_0}$ is a normalization factor. The form of $\eta(T)$ is given by the temperature dependence of $\mathrm{I_{PL}}$. If the value $\eta(T)$ is known for a given temperature, then we can extract from Eqs. 3.2 and 3.3 both the radiative and non-radiative recombination times,

as a function of T, by the following relations.:

$$\tau_R(T) = I_0 \frac{\tau_D(T)}{I_{PL}(T)} = \frac{\tau_D(T)}{\eta(T)}, \tag{3.4}$$

$$\tau_{NR}(T) = \tau_D(T) \frac{I_0}{I_0 - I_{PL}(T)} = \tau_D(T) \frac{1}{1 - \eta(T)}. \tag{3.5}$$

In figure 3.4(a) and (b), are presented the estimated values for the radiative τ_{R} and non-radiative τ_{NR} lifetimes, as a function of temperature, for different values of η. Several conclusions can be drawn: for all η_o at T=0, the radiative recombination times are higher than 1.7 ns and remain practically constant with temperature, in line with the zero degree dimensionality of the system. The small increase of τ_{R} with temperature can be attributed to the large base to height aspect ratios of the QDs discussed here, allowing for some carrier thermalisation in closely spaced lateral quantization higher excited states. Furthermore, as expected from the drop in PL intensity, the τ_{NR} curves obtained for various values of η_o, merge above 100K and reach values below 1 ns, implying that at high temperatures the decay time is essentially dominated by non-radiative channels.

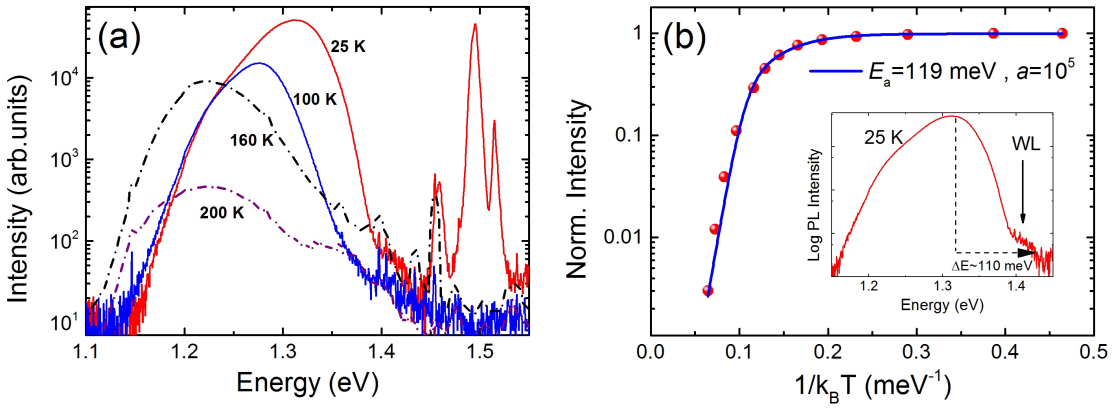

Figure 3.5: (a) Temperature dependent PL spectra from ensemble of PZ QDs. (b) Arrhenius plot of PL intensity at maximum as a function of inverse temperature for the QD sample presented on figure3.5(a). The solid line is the best fit of the equation described in the text, leading to the main activation energy. (Inset) PL spectrum at 25K showing that the activation energy corresponds well to the energy difference between the WL and the maximum of the QD PL peak.

To comprehend the origins of the non-radiative recombination mechanism, we investigated the activation energy by temperature dependent PL measurements. The PL spectra obtained from an ensemble of (211)B QDs, at different temperatures, are displayed on figure3.5(a). The dashed curves are multiplied by a factor of 12. The QD emission ranges between 1.15 to 1.4 eV, while the emission lines between 1.45 and 1.52 eV are related to the (211)B semi-insulating GaAs substrate. With increasing temperature, the QD PL peak drops in intensity, with an increasing rate above 100K. On figure3.5(b), the Arrhenius plot of the QD PL intensity corresponding to its maxima is depicted. The solid line running through the experimental points, is obtained from the following fitting equation (3.6).

$$I_{PL} = I_0 \left[1 + a \exp(\frac{-E_a}{kT}) + b \exp(\frac{-E_b}{kT}) \right]^{-1}, \tag{3.6}$$

The two exponentials in the denominator, corresponding to different activation

processes, are necessary to describe the tendencies both in the low and high temperature regimes, respectively. In the low temperature range, the small decrease in PL intensity is accounted for by a small activation energy E_b=(30±5)meV, with a relatively weak probability coefficient b, of the order of 10.

The origin of this weak activation process can be attributed to exciton thermalization to the p-shell of the QDs, whose energy separation from the X line has been found by us to be about 30meV in photoluminescence excitation spectroscopy, is not discussed in this thesis. On the other hand, in the high temperature range, the first exponential takes over, characterized by a much larger probability coefficient a, of the order of 10^5, and an activation energy of E_a=(119±24)meV. This activation energy matches well with the energy difference between the QD PL maximum and the wetting layer (WL) energy, ΔE=E_{WL}-$E_{QD\text{-}PL}$, allowing us to conclude that the main activation mechanism for non-radiative recombination is associated with carriers escaping from the QDs to the wetting layer. It should be noted that, in this sample the WL energy is determined by a weak shoulder in the low temperature PL spectrum, as indicated by an arrow in the figure 3.5(b)(inset), which is in very good agreement with the findings of previous studies on samples with more intense WL emission [14]. The fact that the activation energy relates to escape to the WL of electron-hole pairs through the barrier rather than separate electrons or holes, is a strong indication that the thermionic escape rates of electrons and holes from the QD to the WL are comparable.

3.3.2 Conclusions

Based on the above discussion, it is clear that increasing the operating temperature of (211)B InAs QDs involves an effort to increase ΔE. This can be achieved either by increasing the QD size or by "pushing" the WL energy to higher energies by

appropriate use of AlGaAs barriers around the QD layer. In what follows, we chase the latter option because, increasing the QD size, has the disadvantage of introducing dislocations above a critical size and shifting the QD emission to longer wavelengths where CCD arrays based on Si, similar to the ones used in our laboratory, have very low quantum efficiency.

In conclusion, the recombination dynamics of (211)B InAs PZ QDs were investigated by a combination of time-resolved and temperature-dependent PL. The radiative recombination times can be as low as 1.7 ns in spite of the large PZ field inside the dots, and are essentially temperature independent in good agreement with the zero-dimensional character of the dots. Above 100K, the decay time is dominated by non-radiative channels, activated mainly by carrier escape from the quantum dots to the wetting layer.

3.4 Band-gap "Engineering"

This section discusses the methods involved in increasing the activation energy of the carriers in the QDs. Towards this end in the next samples the QD layer is encapsulated between AlGaAs "pseudo-alloys", issued from binary GaAs/AlAs Short-Period Super-Lattices (SSL)s.

3.4.1 Growing low density samples of QDs inside SSL's.

The QD samples are grown by molecular beam epitaxy on (211)B GaAs semi-insulating substrates, as previously mentioned, the only difference being that the QD layer is embedded in (xÅ GaAs/yÅ AlAs) SSL where the GaAs and AlAs thickness vary as x and yÅ respectively. Moreover during the development of this series of samples, the growth conditions are carefully adjusted, for the successful implementation of low density samples, with a density as low as ∼7-8 dots per μm^{-2}, as depicted in figure 3.6(b) which is nearly two orders of magnitude lower than the QD samples studied at the beginning of this work, accompany with a plan-view image of a PZ QD depicted in figure 3.6(c).

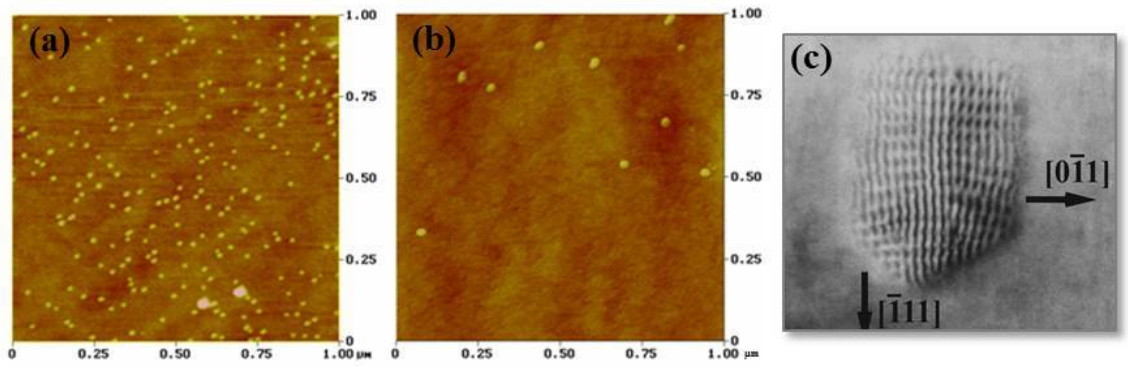

Figure 3.6: (a),(b) AFM images from uncapped samples containing QDs on the surface showing the evolution of grown QD samples from a high density, of a few $10^{-10}cm^{-2}$ down to a few $10^{8}cm^{-2}$, which is very useful for the study of isolated single QDs. (c) Plan-view TEM image of a single PZ QD.

The ability to control the growth conditions is very important since QDs on the low density samples can be easily isolated with standard e-beam lithography into circular nano-mesas for the μ-PL experiments. Although the density of QDs on samples is suppressed, the total InAs deposition of 1.8ML is consistent with our previous results, because the energy position of the WL on reference sample in figure 3.7 is at 1.4eV, consistent with our previous studies. The parameter that was found to influence the QD density on the samples is the InAs growth rate. In terms of beam equivalent pressure (BEP), which is analogue to the ion gate flux, if we consider a constant distance from the target and same ion beam diameter, the change was from 1.6×10^{-7}mbar and 18sec growth time up to 8×10^{-7}mbar and 2 seconds of growth time. This was enough to achieve the low density samples, while preserving the aspect ratio and dimensions of the QDs close to the old ones. The QD growth temperature was fixed at 480°C, and and the growth rates were as high as 0.9ML/s. The growth time was 9 times quicker than in the past growth conditions. Under these conditions, the QDs take the shape of truncated pyramids, with typical heights of 1.5-2.4 nm, and an aspect ratio of 10-12. These values are extracted by analysing the AFM images, of the remaining uncapped samples, as depicted in figure3.6. A He-Cd continuous wave *cw* laser at 325nm, is used as a source of excitation for PL experiments, which is focused onto a sample, fixed on the cold finger of a variable temperature, closed circuit helium cryostat. The signal is analysed using a 0.5m spectrograph with 150 gr/mm grating and is detected by a liquid Nitrogen-cooled Si CCD camera.

3.4.2 PL study from PZ QDs on SSL's.

The PL spectra obtained from ensembles of (211)B QDs embedded in short period binary (xÅ GaAs/16Å AlAs) SSL's, with different relative thickness's of GaAs and AlAs layers are as displayed in figure 3.7.

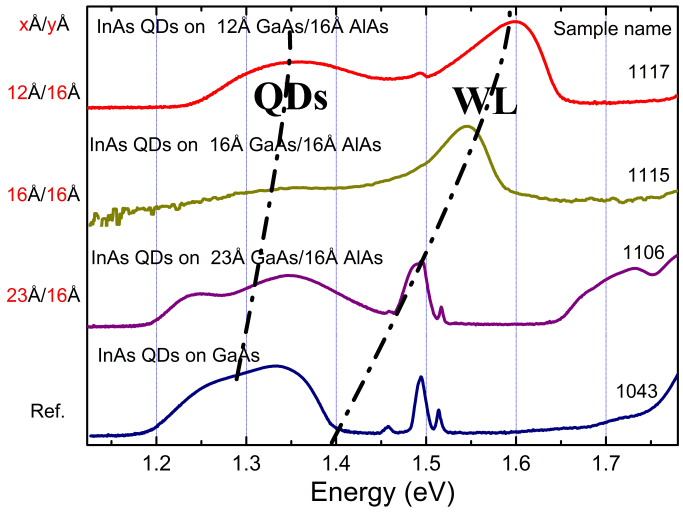

Figure 3.7: Photoluminescence spectra of ensembles of QDs, from samples where the QD layer is embedded in xÅ GaAs/16Å AlAs "pseudo-alloy" SSL with different relative thickness of GaAs and AlAs layers in a straight comparison with the reference sample where the QD layer is embedded in GaAs.

The reference spectrum where the QDs are grown on thick GaAs is depicted in the bottom of figure 3.7, where the WL energy position is at 1.4eV, as mentioned before. This spectrum is included in the figure to emphasize how fast the WL energy blue-shifts, in comparison to the emission energy of QDs, as we decrease the GaAs thickness in the SSL forming a richer in Al pseudo alloy. The much faster blue shift of the WL PL can be attributed to its small thickness of ∼1.3ML, since the carrier wave-functions in a very thin layer are much more sensitive to the surrounding layers compared to the carriers in the QDs, that can extend over several nm in height and several tens of nm in lateral dimensions.

We present now experimental evidence for increased QD emission efficiency at higher temperatures through the investigation of the activation energy in the various samples by temperature dependent PL measurements.

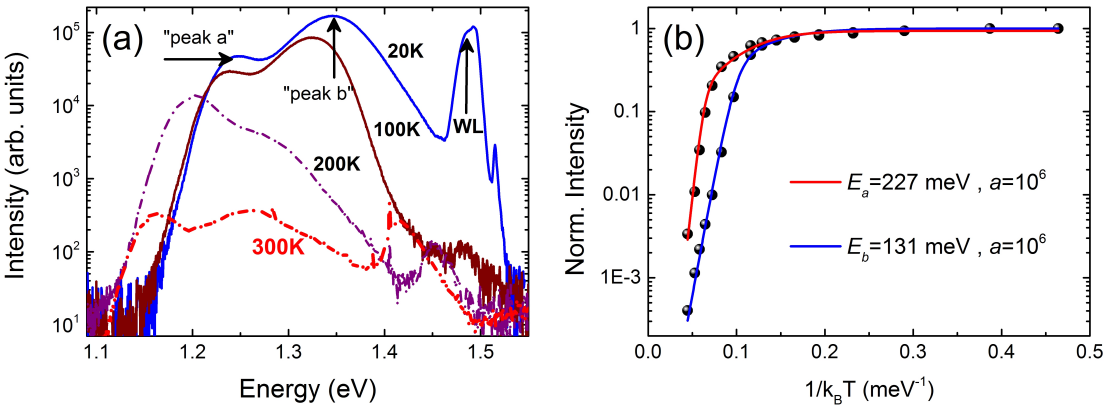

Figure 3.8: (a) Temperature dependent PL spectra from ensemble of PZ QDs. (b) Arrhenius plots of PL intensities for the two maxima indicated by arrows in the spectra. The solid lines (red and blue) are the best fit of the equation (3.6), leading to two activation energies for the "peak a" and "peak b" respectively.

The PL spectra obtained from an ensemble of (211)B QDs inside SSL's at different temperatures, are displayed in figure 3.8(a), the sample named as "1106". The dashed curves are multiplied by a factor of 8. As the temperature is increased, the PL intensity drops but the quenching is much smaller compared to samples without SSL. The activation energies extracted from the best fitting using equation (3.6) of the Arrhenius plots of figure 3.8(b), for the two maxima indicated by arrows as "peak a" and "peak b", are displayed in figure3.8(b). The activation energy with the larger probability coefficient a, of the order of 10^6 for the first "peak a" is $E_a \approx 227$meV and for the second "peak b" is $E_b \approx 131$meV, where on both occasions the weaker activation process, observed as a small decrease in PL intensity in the low temperature range, is accounted for by a small activation energy $E_b \approx 30$meV and is associated to exciton thermalization to the p-shell of the QDs as mentioned previously, and has a relatively weak probability coefficient b, of the order of 10. Taking into account the energy positions of "peak a", "peak b" and the WL, as indicated by arrows, we have calculated the difference in energies

between the emission energies of WL and "peak b" as $\Delta E'_b = E_{\mathrm{WL}} - E_{\mathrm{peak\ b}}$ and between WL and "peak a" as $\Delta E'_a = E_{\mathrm{WL}} - E_{\mathrm{peak\ a}}$. The resulted values were $\Delta E'_b$=135meV and $\Delta E'_a$=248meV respectively, in very good agreement with the extracted activation energies. This leads us to the conclusion that, as expected, the activation energy in these QD samples corresponds very well to ΔE=E_{WL}−$E_{QD\text{-}PL}$, due to which QDs with increased barrier height finally emit up to 300K as depicted in figure 3.8(a)

3.4.3 Conclusions

The emission from QDs, grown inside GaA/AlAs SSL's, result in much improved PL efficiencies at higher temperatures, including up to 300K. The activation energy in these samples can be as high as 230meV, corresponding well to the energy difference between the QD emission at 1.35 eV and the WL transition energy, which in these samples is strongly blue-shifted to 1.59 eV. This result is very promising for the implementation of single photon emitters at elevated temperatures.

REFERENCES

[1] Peter W. Shor. Polynomial-Time Algorithms for Prime Factorization and Discrete Logarithms on a Quantum Computer. *Int. J. Theor. Phys.*, 26(5):26, 1997.

[2] Lov K Grover. Quantum Mechanics helps in searching for a needle in a haystack. *Phys. Rev. Lett.*, 79(2):4, 1997.

[3] Andrew J Shields. Semiconductor quantum light sources. *Nat. Photonics*, 1(4):215–223, 2007.

[4] B Lounis and W E Moerner. Single photons on demand from a single molecule at room temperature. *Nature*, 407(6803):491–493, 2000.

[5] a. Beveratos, S. Kühn, R. Brouri, T. Gacoin, J. P. Poizat, and P. Grangier. Room temperature stable single-photon source. *Eur. Phys. J. D*, 18(2):191–196, February 2002.

[6] Ferruccio Pisanello, Luigi Martiradonna, Godefroy Lenager, Piernicola Spinicelli, Angela Fiore, Liberato Manna, Jean Pierre Hermier, Roberto Cingolani, Elisabeth Giacobino, Massimo De Vittorio, and Alberto Bramati. Room temperature-dipolelike single photon source with a colloidal dot-in-rod. *Appl. Phys. Lett.*, 96(3):50–53, 2010.

[7] P Michler, a Imamoglu, Md Mason, Pj Carson, Gf Strouse, and Sk Buratto. Quantum correlation among photons from a single quantum dot at room temperature. *Nature*, 406(6799):968–70, 2000.

[8] Satoshi Kako, Charles Santori, Katsuyuki Hoshino, Stephan Götzinger, Yoshihisa Yamamoto, and Yasuhiko Arakawa. A gallium nitride single-photon source operating at 200 K. *Nat. Mater.*, 5(11):887–892, 2006.

[9] O. Fedorych, C. Kruse, A. Ruban, D. Hommel, G. Bacher, and T. Kümmell. Room temperature single photon emission from an epitaxially grown quantum dot. *Appl. Phys. Lett.*, 100(6):061114, 2012.

[10] T. Heindel, C. Schneider, M. Lermer, S. H. Kwon, T. Braun, S. Reitzenstein, S. Höfling, M. Kamp, and A. Forchel. Electrically driven quantum dot-micropillar single photon source with 34 *Appl. Phys. Lett.*, 96(1):2008–2011, 2010.

[11] C L Salter, R M Stevenson, I Farrer, C a Nicoll, D a Ritchie, and a J Shields. An entangled-light-emitting diode. *Nature*, 465(7298):594–597, 2010.

[12] Ranber Singh and Gabriel Bester. Nanowire quantum dots as an ideal source of entangled photon pairs. *Phys. Rev. Lett.*, 103(6):1–4, August 2009.

[13] Andrei Schliwa, Momme Winkelnkemper, Anatol Lochmann, Erik Stock, and Dieter Bimberg. In(Ga)As/GaAs quantum dots grown on a (111) surface as ideal sources of entangled photon pairs. *Phys. Rev. B - Condens. Matter Mater. Phys.*, 80(16):161307, October 2009.

[14] G. E. Dialynas, S. Kalliakos, C. Xenogianni, M. Androulidaki, T. Kehagias, P. Komninou, P. G. Savvidis, Z. Hatzopoulos, and N. T. Pelekanos. Piezoelectric InAs (211)B quantum dots grown by molecular beam epitaxy: Structural and optical properties. *J. Appl. Phys.*, 108(10):103525, 2010.

[15] G. E. Dialynas, N. Chatzidimitriou, S. Kalliakos, S. Tsintzos, P. G. Savvidis, Z. Hatzopoulos, and N. T. Pelekanos. Single dot spectroscopy on InAs/GaAs piezoelectric quantum dots. *Phys. Status Solidi Appl. Mater. Sci.*, 205(11):2566–2568, November 2008.

[16] Savvas Germanis, Alexios Beveratos, George E. Dialynas, George Deligeorgis, Pavlos G. Savvidis, Zacharias Hatzopoulos, and Nikos T. Pelekanos. Piezoelectric InAs/GaAs quantum dots with reduced fine-structure splitting for the generation of entangled photons. *Phys. Rev. B - Condens. Matter Mater. Phys.*, 86(3):1–10, 2012.

[17] J. Treu, C. Schneider, a. Huggenberger, T. Braun, S. Reitzenstein, S. Hofling, and M. Kamp. Substrate orientation dependent fine structure splitting of symmetric In(Ga)As/GaAs quantum dots. *Appl. Phys. Lett.*, 101(2):022102, 2012.

[18] M Gurioli, A. Vinattieri, M Colocci, C. Deparis, J. Massies, G. Neu, A. Bosacchi, and S. Franchi. Temperature dependence of the radiative and nonradiative recombination time in GaAs/AlxGa1-xAs quantum-well structures. *Phys. Rev. B*, 44(7):3115–3124, 1991.

[19] J. Simon, N. Pelekanos, C. Adelmann, E. Martinez-Guerrero, R. André, B. Daudin, Le Dang, and H. Mariette. Direct comparison of recombination dynamics in cubic and hexagonal GaN/AlN quantum dots. *Phys. Rev. B*, 68(3):035312, July 2003.

Chapter 4

Single photon emission from a PZ QD at high temperature

4.1 Abstract

In this chapter, the results on temperature-dependent micro-photoluminescence (μ-PL) and cross-correlation measurements, on the emission from an exciton state of single (211)B InAs QDs are presented. In line with the discussion in the previous chapter, on ensemble of QDs, where the QD layer is embedded inside GaAs/AlAs SSL, this chapter discusses the single QD behaviour of such QDs at elevated temperatures. As it will be shown, the large exciton-biexciton (X-XX) splittings of the system allows for the observation of anti-bunching behaviour up to 150K, for the first time in an InAs-based QD system.

4.2 Introduction

It is well known and proven by experiments that a QD is a sustainable source of single photons with narrow spectral line-widths, high generation rates and of course high internal quantum efficiency and stability [1, 2, 3, 4]. For all these reasons, QDs are characterized as artificial atoms, having the ability to produce a regulated photon stream, which contains one and only one photon at a given time interval. For practical reasons, the single photon emitters "on demand" should be able to emit single photons even at high temperatures. Several solid state systems have already been proposed, such as: i. single molecules of terrylene [5], which operate at room temperature but suffer from photo-blinking. Blinking is a process in which the fluorescent emission stops for a certain period of time, and can be either recoverable or non-recoverable [6]. ii. Nitrogen vacancy (NV) color centers in artificial diamond, which also operate at room temperature as single photon emitters [7, 8], but they exhibit relatively long radiative lifetimes of about 10ns, limiting their maximum single photon emission rate. iii. Colloidal CdSe QDs, which also emit single photons up to 300K [1], but they exhibit significant photo-blinking, spectral diffusion effects, and suffer from very long luminescence lifetime of $\sim 1.4 \mu s$ [9]at low temperatures and up to ∼20ns at room temperature [10].

On the other hand the epitaxial QDs such as InAs/GaAs are very attractive having all the advantages of single photon emitters such as high repetition rates, no photo-blinking problems, strong electro-luminescence, and easy integration into photonic microcavities [11, 12] in order to increase their efficiency. They are compatible with the well-established micro-fabrication III-V semiconductor technology and moreover can be integrated into photonic systems, like p-i-n diode structures [13, 14, 15, 16, 17]. In most of the previous attempts with InAs QDs the operation of single photon emitters were limited to low temperatures, such

as 5-8K. In several successful attempts mentioned in the literature, the operating temperature was raised up to liquid nitrogen conditions [18, 19, 20, 21], and only one group managed to show operation at 120K by optical pumping [22]. In this chapter, a detailed study will be presented based on PZ InAs QDs, where the operation of an optically pumped single photon emitter reaches ∼150K. The photon correlation histograms are recorded from the recombination of an exciton state of a SQD, confined in a microcavity, exhibiting sub-Poissonian statistics with an anti-bunching behaviour $g^2(\tau=0)=0.46$ at 150K. Furthermore, a PL emission spectrum will be presented from another SQD, where the PL is still bright up to 260K. This is the first time that the X and XX emission lines from a single InAs QD are resolved at such high temperatures.

4.3 Temperature evolution on the emission of SQDs.

The previous chapter mainly concentrated on QD's inside SSL's, where the activation energies were significantly increased compared with samples without the use of SSL's. One of these samples named as "sample 1117", with the highest activation energy, consisting of QDs grown inside 2.4nm GaAs layer acting as nucleation layer and surrounded by a 20 periods of 1.6ÅAlAs/1.2ÅGaAs SSL, is selected as the next specimen for study. The SQD experiments are performed on the sample after it is processed by standard e-beam lithography into mesas with diameters varying from 350nm to 2000nm, where the inter-spacing between them is $\sim 15\mu$m. A mode locked tunable wavelength Ti:sapphire laser, with a repetition rate of 76MHz, or the same laser operated in CW mode, is used as the source of excitation, focused using a 40x objective, with a numerical aperture of 0.65. The same objective is used to collect the micro-PL (μ-PL) emission-signal which is then analysed through a 0.75m spectrograph equipped with 1200 gr/mm grating, blazed at 750nm. The spectra are recorded by a high quantum efficiency back-thinned liquid Nitrogen-cooled CCD.

The determination of X and XX emission lines from a SQD, is made possible with high degree of confidence, by power dependent measurements, in cases where other emission lines are absent around the spectral area of interest, which is the SQD emission area. The same approach is followed for every SQD investigated. In figure 4.1(a), power dependent spectra are shown under different powers of excitation recorded at 78K. At low powers of excitation, the X transition energy is dominant whereas at high powers, the XX gains more intensity compared to X, which is normal in experiments where the excitation is in CW mode. This behaviour is expected because at low powers, the rate of excited carriers is low

and inside the QD, electrons and holes are formed and recombine as excitons. As the power is increased, the rate of excited carriers increases as well, and as a consequence the probability having more than one exciton (XX) in the QD becomes higher.

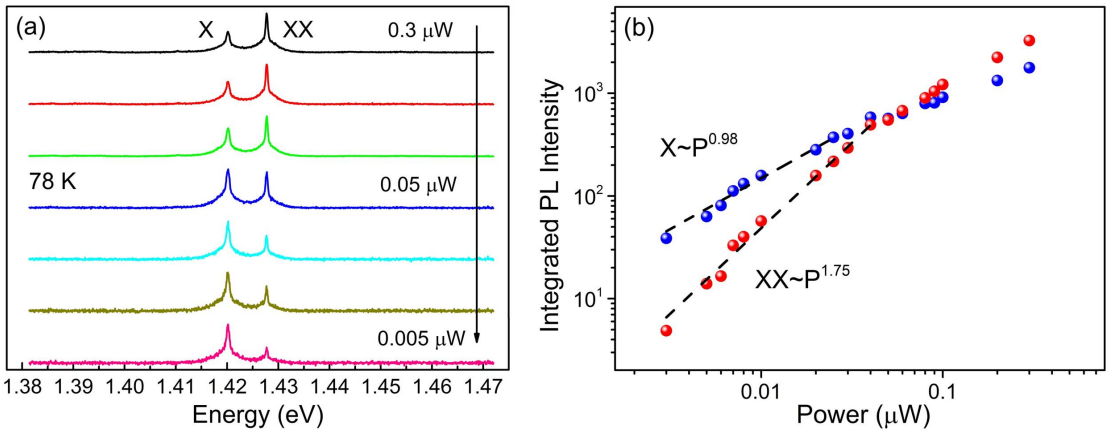

Figure 4.1: (a) A characteristic power-dependent behaviour for the exciton (X) and bi-exciton (XX) emission lines of a SQD under different powers of CW excitation. (b) Integrated intensity of X and XX emission lines versus excitation power.

The emission peaks are fitted by Lorentzians and the fitted peaks are integrated. The different behaviour of the integrated intensity for the X and XX emission peaks as a function of excitation power is depicted in figure 4.1(b). The power dependence of the integrated intensity, for the X state is linear ($\sim P^{0.96}$), whereas that for the XX state is nearly quadratic ($\sim P^{1.75}$). In all QDs that will be presented next, the XX appears at higher energy than the X line. These two excited states are well separated and in particular for the SQD of figure 4.1(a) the energy splitting is ~7.6meV, which is a characteristic behaviour of the PZ QDs. The large anti-binding energy of the XX state [23] is a key feature for single QD emission up to room temperature.

In figure 4.2, is shown the evolution of the SQD emission as a function of tem-

perature. Special care is taken during the experiment for the excitation conditions. Specifically, the excitation power is appropriately adjusted, at every temperature, just below the saturation regime of the exciton transition. With this method the carrier recombination rate from the X and XX states can be kept constant. The exposure time is the same for all spectra and for clarity the intensity of each spectrum is normalized to unity.

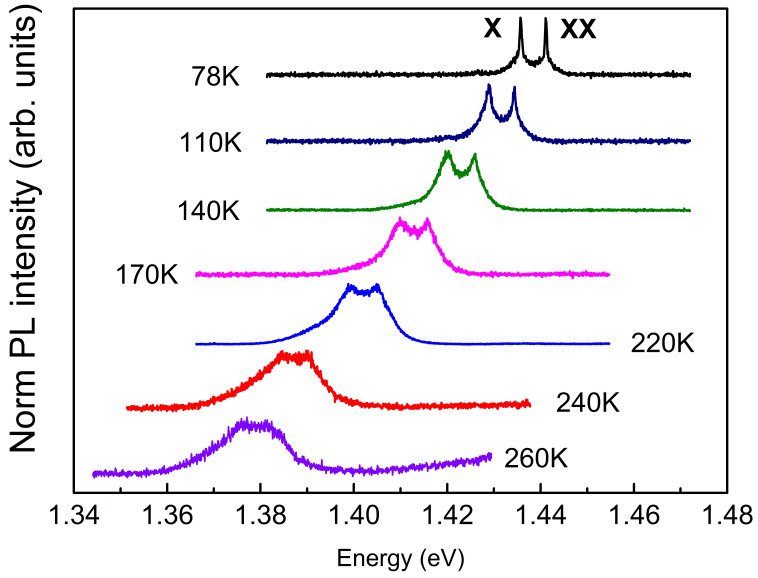

Figure 4.2: Temperature dependence of Micro-PL spectra from a SQD in the range of 78 - 260K. The X and XX emission lines are well distinguished even at 260K. The intensity of each spectrum is normalized to unity.

As the temperature is increased, the two peaks attributed to X and XX emission lines, shift simultaneously to lower energies, following the decrease of the band gap. In order to understand the spectral evolution with temperature of a single PZ QD, in figure 4.3(a) we plot the temperature dependence of the unstrained band-gap (E_g) according to the Varshni law for GaAs or InAs [24]. The relations for the GaAs and InAs are taken from M. Baira et. al. [25], which are described by the following equations:

$$E^{GaAs}(T) = E^{GaAs}(0) - \left(\frac{0.00058T^2}{300+T}\right) \tag{4.1}$$

$$E^{InAs}(T) = E^{InAs}(0) - \left(\frac{0.000419T^2}{271+T}\right) \tag{4.2}$$

It should be noted that the temperature dependence of the energy band-gap for GaAs, is independent on the crystal orientation [26]. Therefore, it is also applied to our case. A comparison between the Varshni's relations for GaAs and InAs and the experimental energy positions of the exciton state of a SQD is presented in figure 4.3(a).

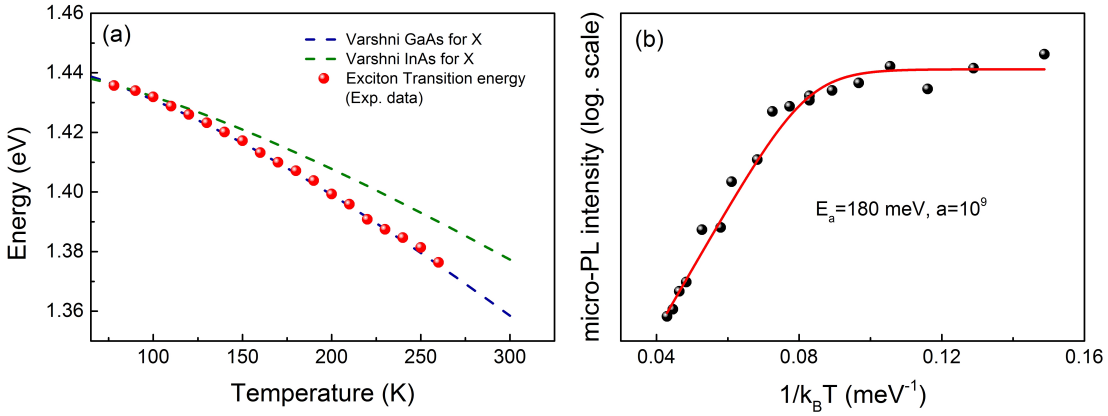

Figure 4.3: (a) Exciton transition energy reduction as a function of temperature following the Varshni model for GaAs energy band gap reduction. (b) Evolution of the X line integrated intensity as a function of kBT resulting that the activation energy mainly is attributed to carriers escape from QDs to WL.

As it can be observed, the SQD emission follows the Varshi relation for GaAs. This could be attributed firstly, to the fact that the larger part of the electron wave function is located inside the GaAs, and secondly because of possible GaAs segregation inside the InAs QD matrix. As a matter of fact, this result alerted us to reconsider the structure of QDs which led us to an analytical structural analysis of the QDs, which will be discussed in the next chapter 5.

The quenching of the integrated μ-PL intensity at higher temperatures is shown in figure 4.3(b). It is a clear indication that the number of carriers for radiative recombination reduces as the temperature increases, and this is attributed to the following reasons. First of all the carriers are thermally activated and escape from the QD to the WL, as the activation energy of ∼180 meV corresponds well to the energy difference between X transition energy and WL energy position. Moreover, at higher temperatures the X radiative recombination time increases slightly with T as shown in chapter 3 and in figure 3.4(a), contributing to the further drop of PL intensity.

4.3.1 Temperature dependence of the exciton homogeneous linewidth

Another important QD parameter for SPS applications is the linewidth (Γ) of its X emission line and its temperature dependence. The following relation 4.3 is a general equation which describes the exciton peak full width at half maximum (FWHM) linewidth $\Gamma(T)$ as a function of temperature, in quantum wells and bulk semiconductors [27] due to phonon scattering. Moreover, the same equation is used generally for QDs, such as InGaAs [28] and even in colloidal CdS/ZnS QDs [29].

$$\Gamma(T) - \Gamma(T=0) = \gamma_{ac}T + \gamma_{op}\frac{1}{exp(\hbar\omega_{LO}/kT) - 1} \tag{4.3}$$

Where $\Gamma(T = 0)$ is the zero-T linewidth, γ_{ac} and γ_{op} are the terms which represent the acoustic and optical phonon scattering respectively, and $\hbar\omega_{\mathrm{LO}}$ is the energy of the longitudinal optical (LO) phonon of GaAs. In figure 4.4, we plot the extracted FWHM linewidth (red and blue spheres), from an X and XX line of a PZ SQD, as a function of temperature. These data are compared with linewidth values available in the literature for InGaAs-based (100) QDs measured in two

different excitation conditions: non-resonant excitation (triangles) similar to our experiments, and resonant excitation (rhomps).

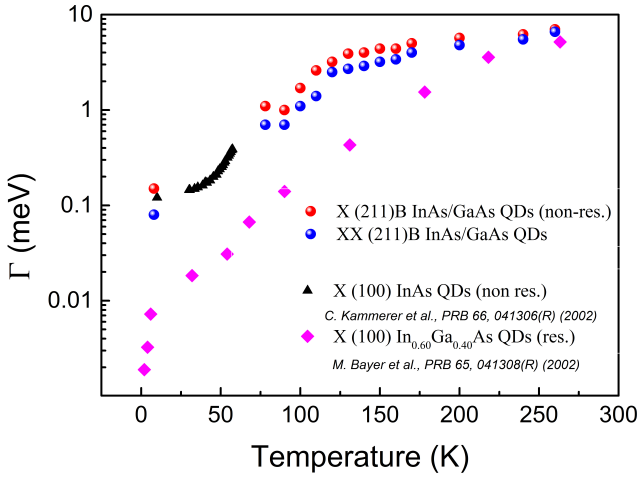

Figure 4.4: Experimental temperature dependence of XX and X linewidths for (211)B QDs in comparison with reported results of (100) QDs under resonant and non-resonant excitation conditions.

$\Gamma(T = 0)$ in our case is $90\pm15\mu eV$, which is two orders of magnitude larger than the natural linewidth $\Gamma_0 = \hbar/2\tau$ where τ is the radiative lifetime for the (211)B QDs, which is expected to be τ_D=1.3-1.8ns as discussed in Chapter 3.3.1 and visible in figure 3.2(b). The relatively elevated spectral broadening of the X line at low temperature can be attributed to spectral diffusion effect, from charges in the QD environment. First important observation of figure 4.4 is that the PZ-QD's linewidths seem to merge and to form a single curve with the non PZ-QD's, measured under non-resonant conditions. At T> $100K$, the exponential increase seems to slow down, and at 260K the experimental linewidths for the PZ QDs are 6-7 meV, similar to the non-PZ QDs [30, 31, 32]. It is worth noting that the curve for the PZ-QDs merges at high T', with the curve for non-PZ QDs obtained under resonant conditions. the above data, strongly support the idea that the presence of

high internal fields in PZ QDs does not seem to generate any additional broadening of the exciton emission line compared to non-PZ QDs. We have to mention here that the above study is limited to a PL study with non-resonant excitation. Future experiments with resonant excitation may show narrower linewidths as they are already proposed and observed by Kammerer et. al.[30].

4.4 QDs in MCs

4.4.1 Collection efficiency strategy.

During the initial study with micro-PL measurements, we realized that the PL efficiencies of single QDs were relatively low, limited to a few tens of counts per second (c.p.s.) at 78K. These numbers of c.p.s. are not enough for the implementation of photon correlation measurements, which are essential in order to observe the anti-bunching behaviour of the emitter and establish whether it can be considered as a single photon source or not. We have realised, with the standard structure based on GaAs, that the high refractive index of GaAs of 3.5 at 930nm where the SQDs emit sets a serious limitation, in the sense that only a small fraction of the emitted photons can possibly escape from the top surface of the structure. The equation 4.4 below describes the critical angle above which total internal reflection (t_{ir}) on the top semiconductor/air interface occurs.

$$\vartheta_{t_{ir}} = sin^{-1}\left(\frac{n_{air}}{n_{GaAs}}\right) \tag{4.4}$$

Applying the previous equation with GaAs constants, we obtain a very low critical angle of 17^o, which means that all radiation emitted at higher angles is fully reflected and does not come out of the structure. Taking into account that a single photon emitter can behave as a point source emitting in all directions, the portion of photons that can be efficiently collected is relatively low. If we consider now an objective lens with a N.A. of 0.65, such as the one is used in our experiments, the collection efficiency η of the system can be calculated by the following equation:([33] and references therein.)

$$\eta = \left(1 - \left(\frac{n_{GaAs} - n_{air}}{n_{GaAs} + n_{air}}\right)^2\right)\left(\frac{1}{2} - \frac{3}{8}cos(sin^{-1}(\frac{NA}{n_{GaAs}})) - \frac{1}{8}cos^3(sin^{-1}(\frac{NA}{n_{GaAs}}))\right) \tag{4.5}$$

The total efficiency η then for GaAs and $N.A. = 0.65$ is $\sim$0.9%. Many techniques have been used to improve the collection efficiency, such as interface surface roughness, solid immersion lens of LaSFN9 glass or GaAs, and of course semiconductor microcavities [34, 35, 36]. The current study utilizes the semiconductor microcavity approach.

4.4.2 Enhanced Spontaneous emission from SQDs by a Semiconductor Microcavity.

A long time ago Purcell proposed the method to control the spontaneous emission (SE) rate of a quasi monochromatic dipole by using a cavity, thereby coupling its emission with the electromagnetic modes of the cavity [37]. This can also be applied to the case of single QDs. The ability to enhance the SE rate has opened a new era to develop high-efficiency single photon emitters. In the case of the study here, four samples were grown, two of which will be discussed here, with one of them being suitable for high temperature operation.

As a first step, we decided to grow the microcavity (MC) samples following the guide line of Bennett et. al. [33]. The researchers in their study suggested that the maximum efficiency for a λ-cavity can be achieved using a 12-period bottom mirror and an optimum 4-period for the top mirror. The quantum efficiency of such a structure could thus be increased to $\sim$ 11.8% in comparison to the 0.9% of the the regular structure.

In addition, by making use of the transfer matrix method described in detail

by Furman [38], the MC structures were modelled to meet the requirements of the SPEs described in this work. Design optimization of the structure is non-trivial due to the fact that the QDs have to be positioned in the cavity in a way that maximum coupling is achieved with the photon field at the cavity mode linewidth, considering the fact that QD emission is really narrow. Moreover an additional prerequisite is that the cavity mode should support at least a certain frequency range, where not only the exciton emission line but also the biexciton one can benefit. In other words, the cavity mode should be broad enough, supporting an energy range of the order of 10-20 meV, which means that the Q factor should be relatively small. In order to comply with all these issues, only three stacks of $\lambda/4$-pairs are used in the top Distributed Brag Reflector (DBR), resulting in a low Q factor as will be discussed below.

4.4.3 Sample fabrication and structural characterization.

The total structure which consists of the bottom/top DBRs, the cavity and the QD layer, is grown on (211)B SI GaAs substrate after a GaAs buffer with approximate thickness of $1\mu m$. The bottom stack of quarter-wave GaAs/AlAs DBRs consists of 14 periods giving a highly reflective mirror of ∼99%. Then a xÅGaAs/yÅAlAs SSL or a simple GaAs layer, constitute the λ-cavity, which contains in the middle the QD layer. The cavity length defines the number of anti-nodes that are formed along the cavity. We decided to use a λ-cavity design that supports only one mode in the anti-node of the electromagnetic field, exactly positioned in the middle of the cavity layer. Finally, the top stack is grown which consists of 3-periods of GaAs/AlAs DBR. The QDs are grown by Stransky Krastanow growth mode, by depositing 1.8ML of InAs, and the position is fixed at the anti-node of the electromagnetic field inside the cavity in order to increase the total light collection efficiency from the QDs. Special care is taken to keep the density of self-assembled

QDs low, about ∼7-9 QDs per μm^2, to facilitate the isolation of SQDs through processing.

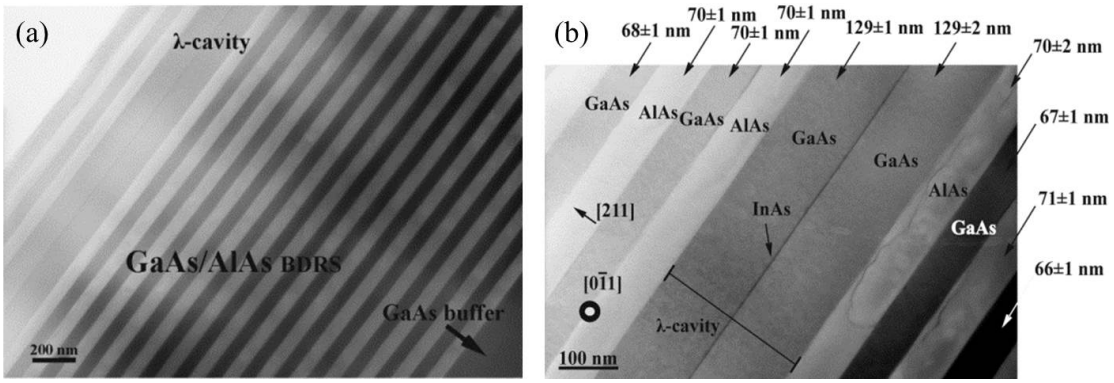

Figure 4.5: (a), (b) Cross-sectional TEM images from an MC sample, taken along the [0-11] zone axis. The morphology of the structure above the GaAs buffer layer and along the growth direction is depicted.

In figure 4.5(a), a TEM micrograph is shown depicting the overall morphology of one of the four samples named as "sample 1102", and figure 4.5(b) shows a zoom-in of the λ-cavity and a few layers of GaAs/AlAs DBRs. As can be seen from the image, the interfaces between AlAs and GaAs appear to be sharp without misfits and in addition the whole structure is dislocation free. The thickness of AlAs layers are around 70±1nm while that of GaAs layers are around 67±1nm , as visible in figure 4.5(b). Each GaAs layer of the λ-cavity is measured to be around 129±1nm, which gives a total cavity thickness of 261nm including the QD layer. The nominal values for GaAs and AlAs in the DBRs were 69nm and 80nm respectively, while the total cavity thickness was supposed to be 270nm. The variation on AlAs layer thickness between the nominal and the measured value can be attributed to the fact that the growth rate calibration of the MBE system referred to (100) orientation. However, in our structure this small variation does not affect significantly the CM position and the overall DBR quality. On the other hand, the GaAs thicknesses match well with the nominal ones, and furthermore

the QD layer seems to be positioned at the exact center of the cavity layer, which is the most important for enhanced radiative coupling.

Elements of processing. Next, we describe the main processing steps for the fabrication of SPE's. Firstly the sample is cleaned using standard organic degreasing agent. The degreasing process involves dipping of the sample in acetone for 1min, then in isopropanol for another 1min and finally rinsing in running deionized water. Then, the sample is baked at 110°C on a hot plate for approximate 15 min, for the dehydration of the substrate prior to e-beam lithography resist deposition, which increases resist film adhesion to the substrate. The appropriate Electron beam sensitive resist used for the etching process is the ma-N2403 of Micro resist Technology. The resist is spun on the sample substrate using the spin coater (SPS Spin 150) at 3000 rotations per minute (rpm) for 40 sec in order to obtain a final resist film thickness of around 300nm. The film is thermally stabilized with a bake on a hot plate at 90°C for 2 min. The resist is then exposed using an electron beam for the definition of the patterns that will be used as soft masks for the subsequent dry etching which results in the formation of mesa pillars. The specific resist is a "negative tone", which means that the exposed areas are partially cross-linked and that they can withstand the subsequent development process. At the end of the development, the exposed area patterns remain on the substrate which in turn is used as a masking material. The equipment used for this job is the Field Emission SEM (Jeol 7000F), where e-beam lithography is possible due to the electron beam writer equipment attached to the system (Raith Elphy Quantum). After the exposure, the sample is developed in the ready-to-use developer ma-D525 of Micro resist Technology, which is Tetramethylammonium hydroxide (TMAH) based, for around 1min. A further thermal stabilization of the resist is required for the dry etching process and the sample is heated at 100°C on a hotplate for about 5min.

The next step includes the mesa formation through the following procedure. The tool used for the dry etching of mesa pillars is the Reactive Ion Etching system (Vacutec 1500) equipped with an in-situ laser interferometry system. The whole process is monitored using in-situ laser interferometry in order to make an estimation of the etch depth, during the process. After the process is finished, the remaining resist film is stripped using the standard cleaning condition as mentioned earlier, (aceton, isopropanol, water rinsing), and the sample is ready for optical measurements. The final product of the processing procedure is depicted in figure4.6, where we observe micropillar-mesas with diameters varying from 350nm to 2500nm whereas the height of each mesa is about 800nm. The height of the mesa is such that it includes the top DBRs, the cavity length and 1-2 periods of the bottom DBRs.

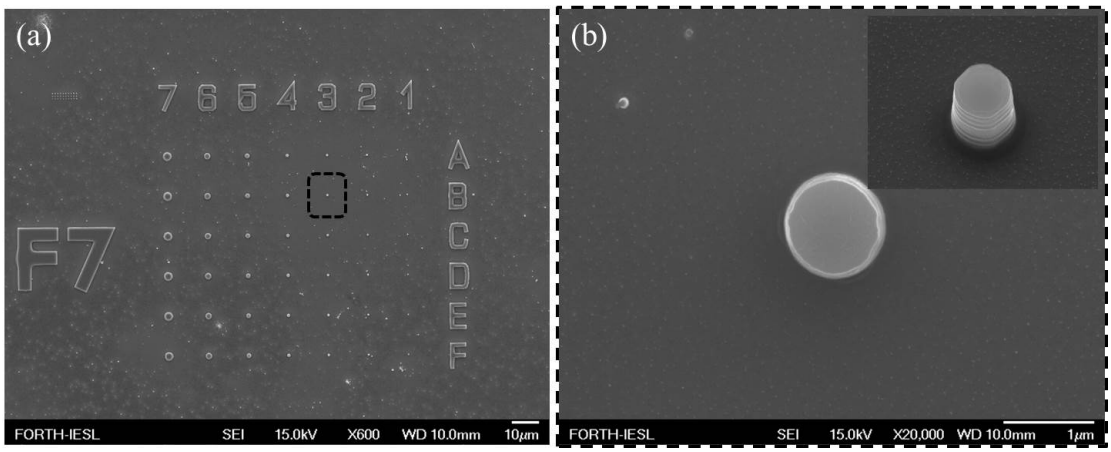

Figure 4.6: (a) SEM image representing a full period after standard process stage, containing mesas of different diameters for the purpose of micro-PL experiments. (b) A top view of an isolated mesa from the squared area of the previous image with diameter is 850nm and height of 800nm. (inset) In the inset is depicted the same mesa inclined. Some of the bottom and all the top DBR periods can be distinguished.

4.4.4 Optical characterization.

The main optical characterizations of the samples include PL (micro-PL) before (after) the processing procedure, and reflectivity. Before continuing with the discussion results, it is useful to address the setup for the optical characterization of samples. The optical setup used is depicted in figure 4.7, which consists of a typical micro-PL accompanied by a reflectivity set-up. The reflectivity setup can be described by the following steps. 1) a Halogen lamp, where the light is guided through a Multi Core Fibre (MCF) (yellow-cores) to illuminate the sample area under investigation. 2) The reflected light from the sample is collected using a Multi-Mode Fibre (white-core) (MMF) which is positioned at the center of the bunch of fibres as described in the figure inset. 3) The light is now analysed by a spectrograph and recorded by a high quantum efficiency back-thinned liquid Nitrogen-cooled CCD camera.

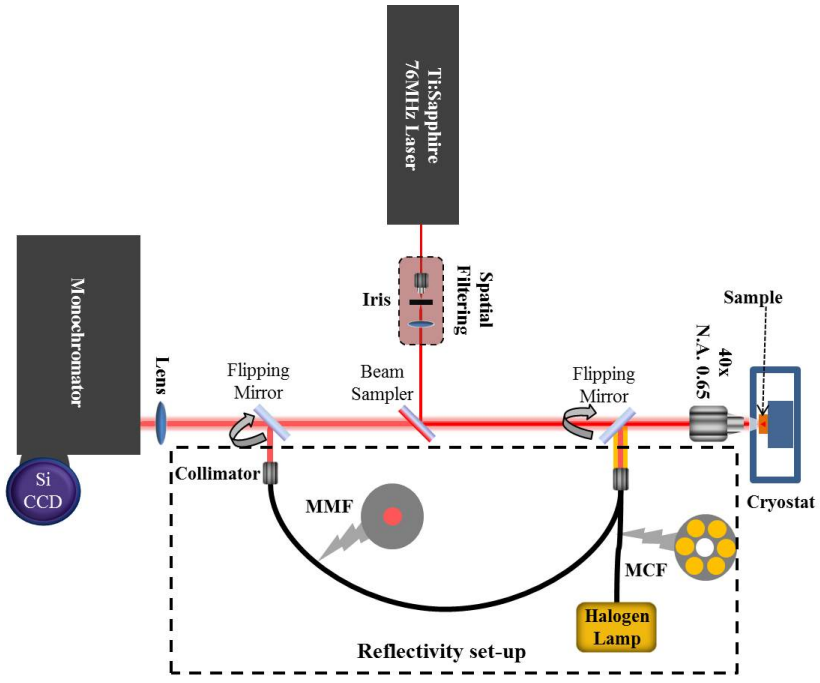

Figure 4.7: A Schematic representation of a typical micro PL set up accompanied with a fibre coupled reflectivity set-up.

The reflectivity response from the samples must be close to the simulated results, since the values for layers thicknesses used in the model are close to their actual thicknesses, estimated for the growth recipe. A direct proof of the above is obtained by comparing the reflectivity (straight-lines) of the planar cavity samples with the corresponding PL spectra derived from the emission of the QD ensembles (dash-lines), shown in figure 4.8. As expected, an enhancement in PL efficiency is observed at the Cavity Mode (CM) area for both samples named as "1101" and "1102". In sample 1101, the reflectance in the stop band area is not as high as in 1102, which probably means that in the latter sample the bottom stack of DBRs constitute a better mirror compared to the former.

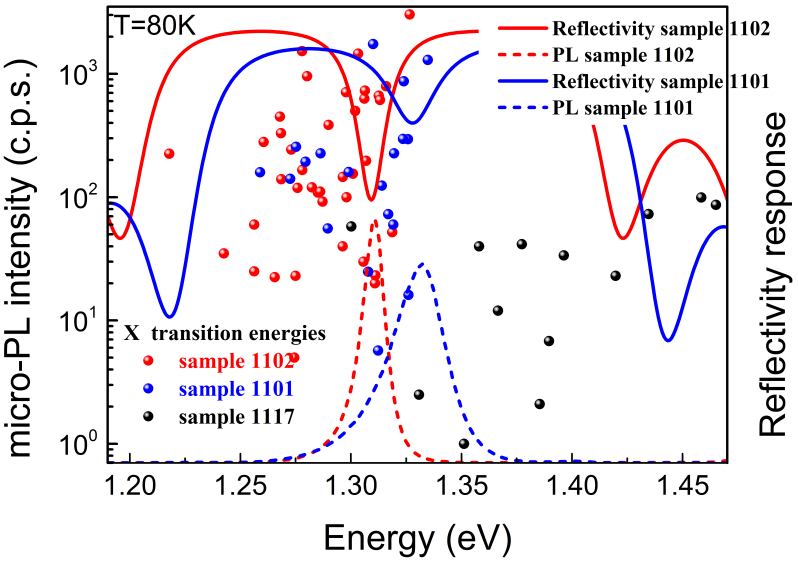

Figure 4.8: Micro-PL intensities in counts per second on logarithmic scale (left) from exciton emission lines of three different samples. The red and blue circles correspond to exciton lines from QDs in MCs, whereas the black circles from QDs in a regular structure. In the reflectivity spectra of the planar cavity samples (blue and red lines), the stop bands and CM positions can be distinguished for each sample. The PL spectra from the corresponding samples match well the CM positions observed in reflectivity.

Moreover the CM in 1102 sample is deeper and narrower compared to 1101 which goes along with an enhanced DBR mirror in 1102 and the higher reflectivity (R) value in the stop-band, resulting in an enhanced quantum efficiency for the emitters (Purcell effect) in 1102 cavity.

Before proceeding any further it is important to address the following points which are essential to observe a large Purcell effect. Purcell, assumed a localized dipole that emits at a wavelength λ_e with a spectral linewidth of $\Delta\lambda_e$ placed in resonance with a single cavity mode. The specifications of the cavity mode are the following: wavelength λ_c, linewidth $\Delta\lambda_c$ and a quality factor of Q.

$$Q = \frac{\lambda_c}{\Delta\lambda_c} \tag{4.6}$$

Since the $\Delta\lambda_e \ll \Delta\lambda_c$ we call this regime as "weak coupling" regime and the spontaneous emission (SE) rate is then given by the Fermi's golden rule, which for an electric dipole transition has the following form:

$$\frac{1}{r} = \frac{4\pi}{\hbar}\rho_{cav}(\omega)\langle|\overrightarrow{d}\cdot\overrightarrow{\varepsilon}(\overrightarrow{r})|^2\rangle \tag{4.7}$$

Where the $\overrightarrow{\varepsilon}(\overrightarrow{r})$ is the amplitude of electric field in vacuum for an emitter at a position $\overrightarrow{r}$, $\overrightarrow{d}$ is the electric dipole, $\rho_{cav}(\omega)$ is the density of modes for the emitter at angular frequency of ω which is given by a normalized Lorentzian in the case of the cavity mode.

Next the spontaneous emission (SE) rate in a cavity mode can be referred to as the total SE rate in a homogeneous medium and is given by the Purcell factor as follows.

$$F_p = \frac{3Q\lambda_c^3}{4\pi^2 n^3 V} \tag{4.8}$$

Where n refers here to the refractive index of the medium and V to the effective cavity volume. The Purcell factor as described above is the figure of merit for the cavity alone and describes the ability of a cavity to increase the coupling of an ideal single photon emitter with the vacuum field. This can be achieved in two ways: either via a local enhancement of its intensity by small cavity volumes V, or by reducing the effective mode density by high Q-factors.

Finally in order to have a successful coupling, several important conditions must be fulfilled. Firstly, the emitter i.e. a QD, must emit in exact resonance with the cavity mode. Secondly, the SPE must be located at the anti-node of the vacuum field. Thirdly, the dipole should be parallel to the vacuum electric field. The conditions are fulfilled by the microcavity samples presented in this part of the study. The layer of QDs is inserted at the center of the λ-cavity, while the dots of interest are in resonance with the CM. Even if the Q-factors in our MC samples are not very large, still the Purcell factor must be high enough in order to justify the micro-PL intensities of QDs inserted in MCs, as shown in figure 4.8.

The mean value of c.p.s. intensities from the samples with QDs inside cavities are on the average 4-5 times higher than the QDs in a regular structure (sample 1117). This means that the SE rate is enhanced by 4-5 times for the QD excitons which are coupled to the cavity mode. Especially, figure 4.8 shows the response of some QDs that satisfy the previous conditions, where the magnitude of the effect is sufficiently high when the QDs are in resonance with a confined cavity mode. The SE rate exceeds 1000 or even 2000 c.p.s. in some occasions, at a temperature of 80K. These count rates are practically impossible to be observed in regular structures, such as sample 1117 where the maximum count rate achieved is 40 c.p.s.. All these results suggest that we successfully achieved to enhance the SE rate of single photon emitters by placing them inside microcavities. In the next section, the quantum nature of the light emitted from a QD will be demonstrated

by cross correlation measurements on the emission from a single exciton state even at high temperatures. It is useful to remind here that the samples used in this study consist of QDs inside microcavities, but the cavity layer material is GaAs for the control samples, whereas for the implementation of high temperature SPE's it is xÅGaAs/yÅAlAs SSL's which act like a "pseudo-alloy" increasing the potential barrier for the carriers in the QD, as it has been presented in the previous section.

4.4.5 High Temperature Anti-bunching behaviour of PZ QDs.

The use of low density samples makes the next experimental stage with micro-PL measurements easier. For the implementation of micro-PL measurements, time-resolved PL (TRPL) and cross correlation experiments, a mode locked tunable Ti:Sapphire laser is used as a source of excitation for the SQDs, whose repetition rate is 76MHz and its photodiode signal acts as a trigger to the fast on-board module for the TRPL experiments. The dimensions and the beam shape is prepared by a spatial filtering setup, as depicted in figure 4.9, at the output of which, a clean spatial profile of a Gaussian beam is provided to the micro-PL setup. The beam is then focused through a 40x objective with a numerical aperture of 0.65 leading to a lateral resolution of about 1.4μm. The same objective is used to collect the micro-PL (μ-PL) signal, which is analyzed through a 0.75m spectrograph equipped with a 1200 gr/mm grating, blazed at 750nm. The spectra are recorded by a high quantum efficiency back-thinned liquid Nitrogen-cooled CCD. The cross-correlation measurements are implemented in a typical Hanbury Brown and Twiss (HBT) setup, as shown in figure 4.9.

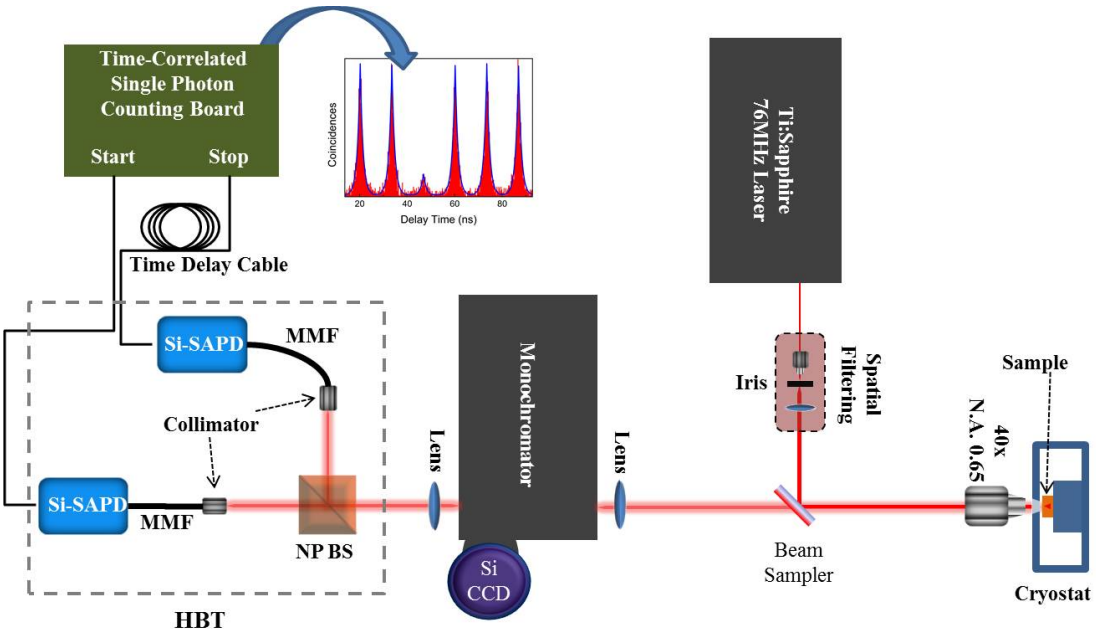

Figure 4.9: A cross correlation measurement set-up consisting of a typical micro PL set up, the HBT interferometer and a Time-Correlator Single Photon Counting Module accompanied with the SPADs as schematically depicted on the figure.

In the HBT [39] setup a monochromator is used for spectral filtering, where the width of the slit opening at the exit defines the spectral area of observation ($\Delta\lambda$), which is recorded using two fast Si Single Photon Avalanche Photodiodes (SPADs). At low temperatures up to 60K, the spectral resolution provided by the slits was arranged to be $\sim 50\mu$eV, whereas at higher temperatures the slits were opened according to the broadening to the exciton lines, which at 150K is about $\sim$2meV. After the beam exits from the monochromator it is split into two beams by using a (50:50) non-polarizing beam splitter (BS). The resulting two beams are then focused onto two SPADs. The SPADs used for the first series of measurements between 8K to 60K are from Perkin Elmer Optoelectronics model (SPCM-AQR-13), whereas for the higher temperatures and lower count rates from Excelitas model (SPCM-AQRH-FC-14), the latter having 8-10% quantum effi-

ciency at 950nm and a time resolution of ∼340ps. To avoid the optical cross-talk between SPADs, two iris with small openings are used in each arm after the beam splitter [40]. The signals (photons-coincidences) are then used to initiate (start) and disable (stop) a time-to-amplitude converter whose output is stored in a multi-channel analyzer. In this study, the signals are analyzed by a multichannel analyser acquisition card, which is a Single Photon Counting module (SPC-130), by Becker and Hickl, containing a complete electronic system for recording fast light signals by Time-Correlated Single Photon Counting (TCSPC) with a resolution of 820fs.

The quantum nature of the emitted light from a single QD, even at high temperatures will be presented in this section. The PL emission of individual QDs at low temperatures, i.e. 8K, consists of sharp lines, but at high temperatures we observe an increase in their linewidths, as already discussed previously. Another difficulty is that the MC structure where the QDs are embedded sets a limitation for the observation of the same single QD in the entire range of temperatures. This is because a QD which at a given temperature emits at a specific wavelength and couples with the cavity mode, when increasing the temperature, it loses intensity as it goes out of resonance with the CM due to the decrease of its energy gap according to Varshni's law. Thus to study the single-photon emission property of PZ QDs at elevated temperatures, different dots entering successively in the energy range of CM have to studied. Hence, the main difficulty of the experiment is to find the next well-coupled QD in the sample at the next temperature.

As it was mentioned earlier a single photon source, such as a QD, emits antibunched photons. The physics of antibunched photons can be realized by the following example. If we consider a two level system that emits a photon at a time τ=0 then it is impossible for it to emit a second one immediately after, because it is already at the ground state. The next photon can be emitted and detected after a waiting time, that can be attributed to the repetition rate of the excitation

source but mainly due to the recombination rate of the system which is higher than the repetition rate of the source of excitation i.e. a pulsed laser source. The result is a dead time between successive photon emission events. In the absence of other sources of light fluctuation, the statistics which describe these photon events are the sub-Poissonian statistics. For comparison, the photon number distribution of a laser source which is operated above threshold is a Poisson distribution which is described by the following relation:

$$P_\alpha(n) = \frac{N^n}{n!} exp(-N) \tag{4.9}$$

$P_\alpha(n)$ describes the probability to find n photons in the coherent state with the mean photon number $N = \alpha^2$. States which possess a narrower photon number distribution is called sub-Poissonian. A QD as a single photon source is able to produce photons "on demand". In this study the experiments are performed in order to prove the quantum nature of our QD system by measuring the second order correlation function or the auto-correlation function $g^{(2)}(\tau)$, as a function of the delay time τ.

$$g^{(2)}(\tau) = \frac{\langle :: I(t)I(t+\tau) :: \rangle}{\langle I(t) \rangle^2} \tag{4.10}$$

The experiments are performed by using the HBT set-up previously described under pulsed excitation conditions. I(t) is the measured intensity where "::" indicates normal ordering. The $g^{(2)}(\tau)$ function describes the probability to measure a photon coincidence at a time τ based on the condition that a first photon has been detected at a time $t = 0$. This means that the PL collected from a single photon emitter has the property of $g^{(2)}(\tau = 0) \approx 0$. The strong quantum correlation easily vanishes by increasing the number of emitters. For this reason, strong photon antibunching $g^{(2)}(\tau = 0) < 0.5$ can be considered as a criterion that a given

emitter is a single photon emitter. The auto-correlation function is measured by using a HBT interferometer set up where the signal of one detector starts a clock until a detection coincidence of the second detector results in a stop (figure 4.9).

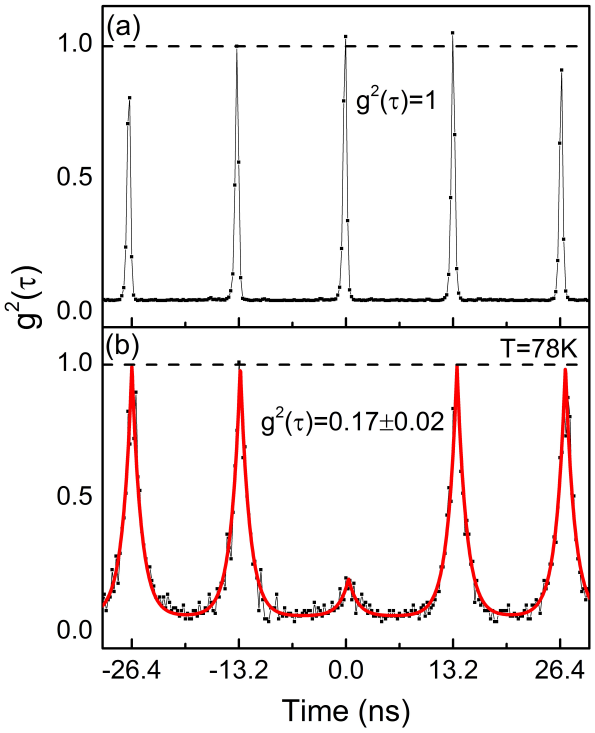

Figure 4.10: Photon correlation function $g^{(2)}(\tau)$ for (a) a pulsed coherent state source such as a laser and (b) a sub-Poissonian state as recorded from an exciton state of single PZ QD at 80K.

In the experiments where the photon correlation measurements are carried out with pulsed excitation, the value of the $g^{(2)}(\tau)$ function can be directly determined without the need of a fitting procedure taking into account the exciton lifetime and the detector response. The information about the photon number correlation between pulses is estimated from the area under the correlation peaks.

Figure 4.10 depicts the recorded histograms normalized with the response of the laser. The top part corresponds to a coherent light source with $g^{(2)}(\tau = 0)$ =1

at zero delay, whereas the bottom part is a comparison, showing an example of the second order correlation function recorded from an exciton QD state with a $g^{(2)}(0)$ =0.17. This value is obtained by normalizing the peak integrated intensity at $t = 0$ by the average area of the other four adjacent peaks. The fitting function which is used for the four peaks is described as follows.

$$correlations(t) = Ae^{-\left|\frac{t-t_0}{\tau_D}\right|} \tag{4.11}$$

In the equation t_0 can be referred to as the zero delay time of a given correlation peak and τ_D as the decay time for the exciton state under investigation.

Experimental evidence of the anti-bunching behaviour at high temperatures.

In the next figures, the histograms obtained using the HBT set up interferometer described above will be presented. The measurements have been performed at various temperatures in order to highlight the possibility of PZ QDs to act as single photon emitters on "demand", at higher temperatures. The experimental data which are presented here can be separated in two, based on the laboratories where the measurements have taken place or by the temperature of the QD system where the histograms are recorded: from 8K and up to 60K the anti-bunching behaviour of the PZ QDs are investigated in the laboratory of prof. Valia Voliotis in the Institute of NanoSciences of the Pierre and Marie Curie University in Paris, and the rest of the measurements at temperatures from 60K up to 150K, are performed in the quantum optics laboratory of Foundation for Research and Technology - Hellas (FORTH), in a new set-up installed by the writer of this manuscript and prof. Nikos Pelekanos. As mentioned before the emitter under investigation is not the same at every temperature-measurement because of the decoupling of the

electromagnetic field between the cavity mode and the emitter. This is the reason that the spontaneous emission lifetime of the emitters is not identical, as it can be easily recognized through the histograms at different temperatures, and varies in the range of 1 to 2ns. The measurements are performed with non-resonant excitation above the band gap of GaAs and always a little below the saturation regime of the examined QD exciton state.

Figure 4.11 depicts the raw second order autocorrelation function $g^{(2)}(\tau)$ of an X line in the temperature range between 8 and 60K. Based on the repetition rate of the laser which is ∼80MHz, every 12.5ns, a correlation peak is observed. At zero delay time the absence of coincidence is the signature of single photon emission from the QD under investigation. Considering the lifetime of this PZ QD it is almost certain that the QD is empty each time a pump pulse arrives. Moreover the start-stop time intervals from SPADs are recorded and then binned with time resolution of 324ps, as depicted in the histograms. The count rate on each SPAD in the two arms of HBT setup ranges from 7000c.p.s. to 20000c.p.s. in the various temperatures, which also includes the dark count rates of either detector. The total dark counts of the detectors was less than 200c.p.s., whereas during the measurements the stray light was about 800c.p.s.. Note that the count rate at 60K is higher than at 20K, partly because the system was pumped at a bit higher excitation conditions, but mainly due to the fact that we removed unused optical elements from the collection's optical path. The total recording time of the correlation events was 60 minutes at 8K and up to 120 minutes at 60K.

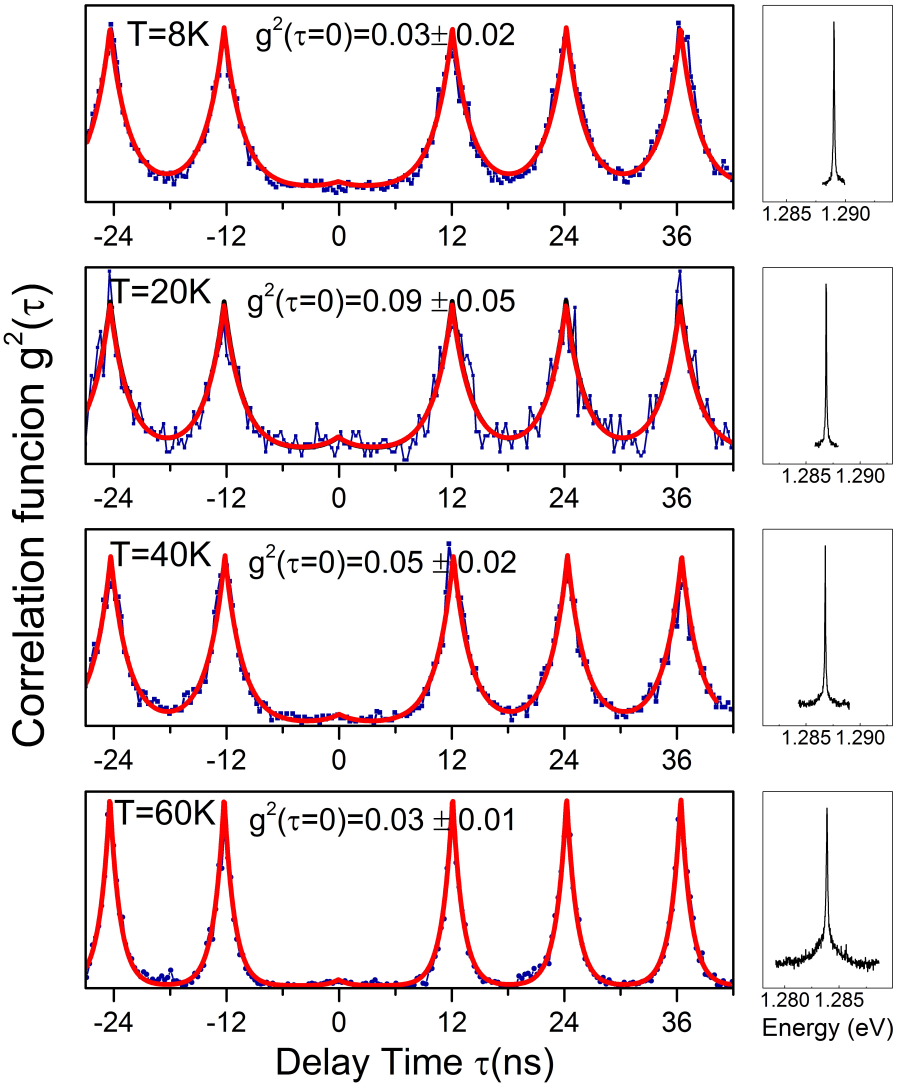

Figure 4.11: Coincidence counts histograms, measured using a Hanbury Brown-Twist interferometer under pulsed excitation representing the second order intensity correlation function $g^{(2)}(\tau)$ (left) of the respective QD exciton emission lines (right), at 8K upper panel and up to 60K lower panel, obtained from sample "1102".

As visible in figure 4.11, we observe a correlation peak at each repetition of the laser pulse and the area under each peak is normalized to $A(\tau) = 1 \pm 0.05$ as described in [2] and [8]. At the zero delay peak, the area is much smaller than the area of the adjacent peak. This absence of coincidences is a characteristic of a single photon emitter. $g^{(2)}(\tau = 0)$, which gives the probability of recording a second event after measuring a first event at t=0, remains practically constant up to 60K. It is estimated to be less than 3% at 8K, 9% at 20K, 5% at 40K and less than 3% at 60K. These numbers are much smaller than the criterion of 0.5 and constitute a direct proof that the photons are emitted one by one from the examined state of QD, showing the clear quantum nature of these emitters. As the measurements are not performed on the same QD, the signal to noise ratio and the decay time of each QD exciton are different on every measurement. In general, the clear and emphatic antibunching behaviour measured at 60K raised our hopes for the following measurements at even higher temperatures.

The next measurements show the ability of PZ QDs emitting photons "on demand" even at higher temperatures than liquid nitrogen conditions (77K), which will be useful for the implementation of quantum devices at a reasonable cryogenic cost, finding niche applications in industry. Figure 4.12 depicts temperature dependent μ-PL spectra from "sample 1120" obtained from a mesa of 400nm in diameter with an integration time of 1sec.

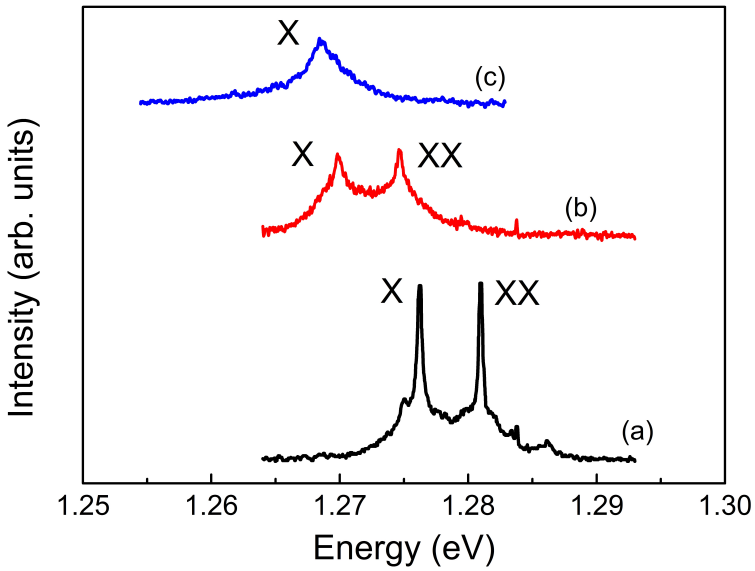

Figure 4.12: Temperature dependent photoluminescence spectra obtained from a 400×400nm micro-pillar with the same optical excitation conditions as in the photon correlation experiments. The temperature and the nominal pump power are (a)78.5K, 115nW (b) 120K, 200nW and (c) 150K, 243nW.

The spectra are obtained under the same excitation conditions identical to the ones used in the photon correlation measurements presented in figure 4.13. The power density of excitation was selected carefully, in all cases below the saturation regime of the exciton line. The spectra are shown in such a way that the maximum intensity of the exciton transition seems to decrease in absolute value, but in actuality the PL intensities remain constant if we consider spectrally integrated intensities under the PL peaks. This means that by increasing the pump power we succeed to keep the average population population at the same level, even though the non-radiative channels become active at higher temperatures. The fact that the count rate on the SPADs decreased significantly at 78K, prompted us to increase the slit width and spectrally filtering a larger spectral window compared to the one used at low temperatures. At the highest temperature of 150K the slits are opened to a spectral resolurion of 3.5 meV, making sure that the larger part of the

emission from a single exciton emission line enters in the collection path.

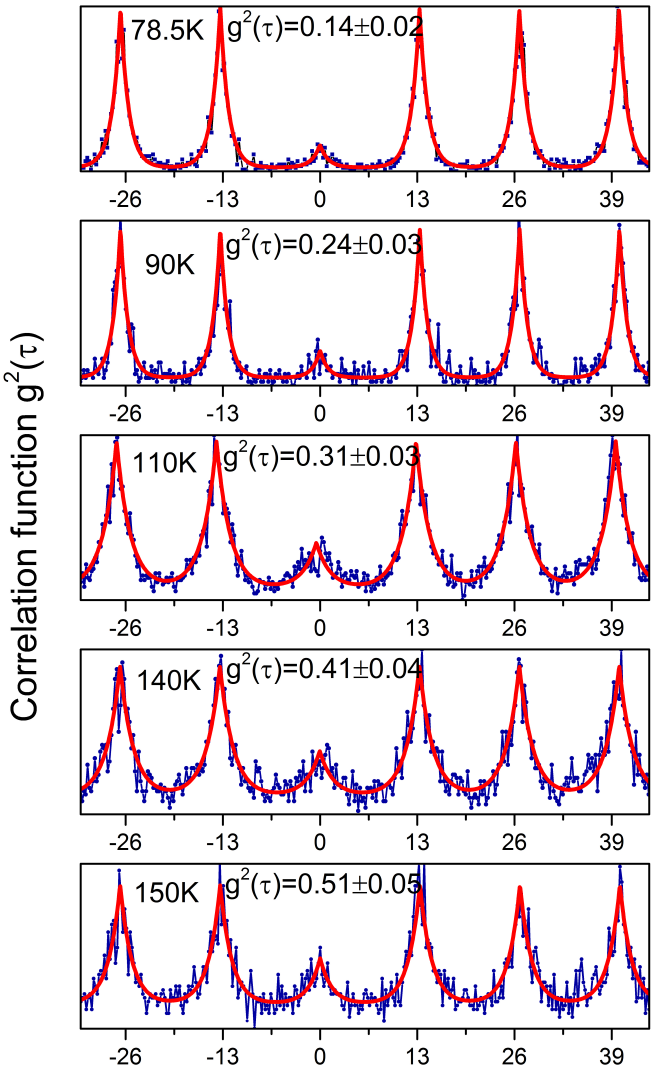

Figure 4.13: Coincidence counts histograms, measured using the Hanbury Brown-Twist interferometer under pulsed excitation, representing the second order intensity correlation function $g^{(2)}(\tau)$ from the emission of a single exciton state at 78.5K (upper panel) up to 150K (lower panel).

Figure 4.13 presents the measurements above 77K where the values of raw $g^{(2)}(\tau = 0)$ measured from the emission of a single exciton line satisfies the criterion required for a single photon emitter up to 150K. The count rates in this set of

experiments are not as high as in the previous experiments at lower temperatures, but enough to acquire satisfactory statistics on the histograms. The repetition rate of the excitation source is 13.2 ns. The histograms are presented after binning with a time resolution of 224ps.

The count rates on each SPAD ranged from 8500c.p.s. at 78.5K to 3800c.p.s at 150K. The recording time for the measurement at 78.5K is 60 minutes whereas at 150K is 210 minutes because of the relatively low count rate from the emitter, for the selected spectral window. The dark counts on the SPADs are 60c.p.s., and 80c.p.s., respectively. In the total, background counts, the stray light noise and background emission from the sample measured next to the X line have also to be included, with the corresponding counts being 320c.p.s. and 480c.p.s. respectively on the two SPADs. At high temperatures, where the spectral window is wider the background signal is increased to about 600c.p.s. and 780c.p.s. respectively.

The clarity and count rates on each histogram are not the same since each QD environment is different and the excitation energy is far way from the QD emission. Additionally, the nonzero $g^{(2)}(\tau = 0)$ is partly due to the broadening of the XX emission which starts introducing coincidences inside the spectral window of the X emission under investigation. Specifically the XX-X energy difference of the QD presented in figure 4.12 is 4.8meV. Moreover, it can be attributed to background emission from deep levels inside the GaAs substrate, which becomes more prominent at high temperatures and at the higher power levels of excitation as the QD intensity drops significantly with T. This explanation cannot be ignored since at higher temperatures, an increased decay time close to 2.5ns and in some occasions a second decay is observed at the SQD line under investigation. This implies that the total decay is long enough to extend into the adjacent correlation peak in the $g^{(2)}(\tau)$ histograms, which is clearly visible in the high temperature histograms of figure 4.13. The extended and/or the second decay are not due to the

X emission line of interest, because by selecting a narrow spectral window around the X line and by performing TRPL measurements, the decay time is found almost the same as at low temperatures, which means that the need to collect more counts on the SPADs for improved statistics of histograms by selecting a larger spectral window, leads to include emission not only from the X line but also from other sources that degrade the $g^{(2)}(\tau = 0)$. All these reasons result in a degradation of the performance of the single photon emitter "on demand" at higher temperatures. There are many ideas to overcome the present temperature limitations of SPE's such as: the use of larger QDs with larger negative binding XX energy such as shown in figure 1.10, avoiding the overlap between X and XX emission lines at high temperatures, and to eliminate background radiation. On the latter, there are two ways: i. resonant excitation at energy below the GaAs energy bandgap or even better below the WL. ii. electrical injection which would limit the recombination in the active region only, where the QDs reside, and eliminate any radiation from the substrate.

4.5 Conclusions.

The ability of the PZ QDs to act as a single photon emitters at higher temperatures than the ordinary (100) InAs QDs has been demonstrated by measuring the second order correlation function $g^{(2)}(\tau)$ at various temperatures and breaking the previous record of 120K, highlighting a new one at 140K. We strongly believe that PZ QDs hold the key for the implementation of quantum information process at a temperature appropriate for industrial use. Due to the fact that the strong PZ field exists inside the PZ QDs, the large exciton-biexciton energy splittings give us the possibility of single SPE's at high temperatures.

REFERENCES

[1] P Michler, A Kiraz, C Becher, W V Schoenfeld, P M Petroff, L Zhang, E Hu, and A Imamoglu. A quantum dot single-photon turnstile device. *Science*, 290(5500):2282–2285, 2000.

[2] Charles Santori, Matthew Pelton, Glenn Solomon, Yseulte Dale, and Yoshihisa Yamamoto. Triggered Single Photons from a Quantum Dot. *Phys. Rev. Lett.*, 86(8):1502–1505, February 2001.

[3] Valéry Zwiller, Hans Blom, Per Jonsson, Nikolay Panev, Sören Jeppesen, Tedros Tsegaye, Edgard Goobar, Mats Erik Pistol, Lars Samuelson, and Gunnar Björk. Single quantum dots emit single photons at a time: Antibunching experiments. *Appl. Phys. Lett.*, 78(17):2476–2478, 2001.

[4] R. Thompson, R. Stevenson, a. Shields, I. Farrer, C. Lobo, D. Ritchie, M. Leadbeater, and M. Pepper. Single-photon emission from exciton complexes in individual quantum dots. *Phys. Rev. B*, 64(20):201302, October 2001.

[5] B Lounis and W E Moerner. Single photons on demand from a single molecule at room temperature. *Nature*, 407(6803):491–493, 2000.

[6] Rob Zondervan, Florian Kulzer, Sergei B. Orlinskii, and Michel Orrit. Pho-

toblinking of rhodamine 6G in poly(vinyl alcohol): Radical dark state formed through the triplet. *J. Phys. Chem. A*, 107(35):6770–6776, 2003.

[7] a. Gruber. Scanning Confocal Optical Microscopy and Magnetic Resonance on Single Defect Centers. *Science (80-.).*, 276(5321):2012–2014, 1997.

[8] a. Beveratos, S. Kühn, R. Brouri, T. Gacoin, J. P. Poizat, and P. Grangier. Room temperature stable single-photon source. *Eur. Phys. J. D*, 18(2):191–196, February 2002.

[9] C. de Mello Donegá, M. Bode, and a. Meijerink. Size- and temperature-dependence of exciton lifetimes in CdSe quantum dots. *Phys. Rev. B*, 74(8):085320, 2006.

[10] Olivier Labeau, Philippe Tamarat, and Brahim Lounis. Temperature dependence of the luminescence lifetime of single CdSe/ZnS quantum dots. *Phys. Rev. Lett.*, 90(25 Pt 1):257404, 2003.

[11] B. Ohnesorge, M. Bayer, a. Forchel, J. Reithmaier, N. Gippius, and S. Tikhodeev. Enhancement of spontaneous emission rates by three-dimensional photon confinement in Bragg microcavities. *Phys. Rev. B*, 56(8):R4367–R4370, August 1997.

[12] J. Gérard, B. Sermage, B. Gayral, B. Legrand, E. Costard, and V. Thierry-Mieg. Enhanced Spontaneous Emission by Quantum Boxes in a Monolithic Optical Microcavity. *Phys. Rev. Lett.*, 81(5):1110–1113, 1998.

[13] Zhiliang Yuan, Beata E Kardynal, R Mark Stevenson, Andrew J Shields, Charlene J Lobo, Ken Cooper, Neil S Beattie, David a Ritchie, and Michael Pepper. Electrically driven single-photon source. *Science*, 295(5552):102–5, January 2002.

[14] Xiulai Xu, D. a. Williams, and J. R a Cleaver. Electrically pumped single-photon sources in lateral p-i-n junctions. *Appl. Phys. Lett.*, 85(15):3238–3240, 2004.

[15] a. J. Bennett, D. C. Unitt, P. See, a. J. Shields, P. Atkinson, K. Cooper, and D. a. Ritchie. Microcavity single-photon-emitting diode. *Appl. Phys. Lett.*, 86(18):181102, 2005.

[16] D. J P Ellis, a. J. Bennett, a. J. Shields, P. Atkinson, and D. a. Ritchie. Electrically addressing a single self-assembled quantum dot. *Appl. Phys. Lett.*, 88(13):13–16, 2006.

[17] G C Shan, Z Q Yin, C H Shek, and W Huang. Single photon sources with single semiconductor quantum dots. *Front. Phys.*, 9(2):170–193, 2014.

[18] a. Kiraz, P. Michler, C. Becher, B. Gayral, a. Imamolu, Lidong Zhang, E. Hu, W. V. Schoenfeld, and P. M. Petroff. Cavity-quantum electrodynamics using a single InAs quantum dot in a microdisk structure. *Appl. Phys. Lett.*, 78(25):3932–3934, 2001.

[19] X. M. Dou, X. Y. Chang, B. Q. Sun, Y. H. Xiong, Z. C. Niu, S. S. Huang, H. Q. Ni, Y. Du, and J. B. Xia. Single-photon-emitting diode at liquid nitrogen temperature. *Appl. Phys. Lett.*, 93(10):1–4, 2008.

[20] L. Cavigli, S. Bietti, N. Accanto, S. Minari, M. Abbarchi, G. Isella, C. Frigeri, A. Vinattieri, M. Gurioli, and S. Sanguinetti. High temperature single photon emitter monolithically integrated on silicon. *Appl. Phys. Lett.*, 100(23), 2012.

[21] . Dusanowski, M. Syperek, a. Maryski, L. H. Li, J. Misiewicz, S. Höfling, M. Kamp, a. Fiore, and G. Sk. Single photon emission up to liquid nitrogen temperature from charged excitons confined in GaAs-based epitaxial nanostructures. *Appl. Phys. Lett.*, 106(23):233107, 2015.

[22] Richard P. Mirin. Photon antibunching at high temperature from a single InGaAs/GaAs quantum dot. *Appl. Phys. Lett.*, 84(8):1260–1262, 2004.

[23] G E Dialynas, C Xenogianni, E Trichas, P G Savvidis, G Constantinidis, and Z Hatzopoulos. Negative bi-exciton binding energy in (211) B InAs / GaAs piezoelectric quantum dots. *Mater. Sci.*, (211):5–6, 2007.

[24] Y.P. Varshni. Temperature dependence of the energy gap in semiconductors. *Physica*, 34(1):149–154, 1967.

[25] M. Baira, L. Bouzaiene, L. Sfaxi, H. Maaref, O. Marty, and C. Bru-Chevallier. Temperature dependence of optical properties of InAs/GaAs self-organized quantum dots. *J. Appl. Phys.*, 105(9):094322, 2009.

[26] D. Lüerben, R. Bleher, and H. Kalt. High-precision determination of the temperature-dependent band-gap shrinkage due to the electron-phonon interaction in GaAs. *Phys. Rev. B*, 61(23):15812–15816, 2000.

[27] D. Gammon, S. Rudin, T. L. Reinecke, D. S. Katzer, and C. S. Kyono. Phonon broadening of excitons in GaAs/AlxGa1-xAs quantum wells. *Phys. Rev. B*, 51(23):16785–16789, 1995.

[28] C. Kammerer, C. Voisin, G. Cassabois, C. Delalande, Ph. Roussignol, F. Klopf, J. Reithmaier, a. Forchel, and J. Gérard. Line narrowing in single semiconductor quantum dots: Toward the control of environment effects. *Phys. Rev. B*, 66(4):041306, July 2002.

[29] D. Valerini, A. Cretí, M. Lomascolo, L. Manna, R. Cingolani, and M. Anni. Temperature dependence of the photoluminescence properties of colloidal CdSeZnS core/shell quantum dots embedded in a polystyrene matrix. *Phys. Rev. B*, 71(23), 2005.

[30] C. Kammerer, G. Cassabois, C. Voisin, M. Perrin, C. Delalande, Ph Roussignol, and J. M. Gérard. Interferometric correlation spectroscopy in single quantum dots. *Appl. Phys. Lett.*, 81(15):2737–2739, 2002.

[31] M. Bayer and a. Forchel. Temperature dependence of the exciton homogeneous linewidth in In0.60Ga0.40As/GaAs self-assembled quantum dots. *Phys. Rev. B*, 65(4):041308, January 2002.

[32] M. Benyoucef, a. Rastelli, O. G. Schmidt, S. M. Ulrich, and P. Michler. Temperature dependent optical properties of single, hierarchically self-assembled GaAs/AlGaAs quantum dots. *Nanoscale Res. Lett.*, 1(2):172–176, 2006.

[33] A. J. Bennett, P. Atkinson, P. See, M. B. Ward, R. M. Stevenson, Z. L. Yuan, D. C. Unitt, D. J P Ellis, K. Cooper, D. A. Ritchie, and A. J. Shields. Single-photon-emitting diodes: A review. *Phys. Status Solidi Basic Res.*, 243(14):3730–3740, 2006.

[34] W.L. Barnes, G. Björk, J.M. Gérard, P. Jonsson, J.a.E. Wasey, P.T. Worthing, and V. Zwiller. Solid-state single photon sources: light collection strategies. *Eur. Phys. J. D - At. Mol. Opt. Phys.*, 18(2):197–210, February 2002.

[35] Martin A Green, Jianhua Zhao, Aihua Wang, Peter J Reece, and Michael Gal. Efficient silicon light-emitting diodes. *Nature*, 412(6849):805–808, 2001.

[36] Kerry J Vahala. Optical microcavities. *Nature*, 424(6950):839–846, 2003.

[37] Em Purcell, Hc Torrey, and Rv Pound. Resonance Absorption by Nuclear Magnetic Moments in a Solid. *Phys. Rev.*, 69(1-2):37–38, 1946.

[38] Sh. a. Furman and A.V. Tikhonravov. *Basics of optics of multilayer systems.* Editions Frontieres, 1992.

[39] R. Hambury Brown and R. Q. Twiss. Correlation between photons in two coherent beams of light. *Nature*, 177(4497):27, 1956.

[40] Christian Kurtsiefer, Patrick Zarda, Sonja Mayer, and Harald Weinfurter. The breakdown flash of Silicon Avalance Photodiodes - backdoor for eavesdropper attacks? *J. Mod. Opt.*, 48(13):2039–2047, 2001.

Chapter 5

Enhanced Stark tuning of single InAs (211)B quantum dots.

5.1 Abstract

In this chapter we demonstrate enhanced Stark tuning of single exciton lines in self-assembled (211)B InAs quantum dots (QDs). This comes as a consequence of pronounced nonlinear piezoelectric effects in polar orientations of Zinc-Blende nanostructures, making this QD system particularly sensitive to relatively "small" applied external fields. The Stark shifts in the first 100kV/cm of applied external field are at least 4 times larger, compared to those observed in non-piezoelectric (100) InAs QDs of similar size. To account quantitatively for the observed transition energies and Stark shifts, we utilize a graded In-composition potential profile, as deduced from the strain analysis of high-resolution transmission microscopy images. Our results provide a direct demonstration of the importance of non-linear piezoelectric effects in Zinc- Blende semiconductors.

5.2 Introduction

Semiconductor quantum dots (QDs) are the ultimate sources of "on demand" single photons [1], entangled photon pairs [2], and indistinguishable photons [3], with direct applications in quantum cryptography and quantum information processing schemes. as previously mentioned in the introductory Chapter 1, piezoelectric (PZ) QDs, i.e. QDs carrying a strong vertical PZ field in their core, offer concrete advantages compared to non-PZ QDs, on several practical aspects of single or entangled photon sources. First, the large exciton biexciton energy difference, encountered in PZ QDs due to the strong PZ field, enable the two lines to remain resolved as the temperature increases, allowing for single photon emission at high temperatures [4]. Second, the PZ field along the QD growth axis preserves the high symmetry of the confining potential [5], leading to negligible fine structure splitting of the ground exciton state [5, 6, 7], which is a prerequisite for the generation of high fidelity entangled photons [8]. Another interesting feature of PZ QDs, which is explored in this Chapter, is their high sensitivity to relatively "small" external electric fields, giving rise to enhanced Stark tunings of their exciton lines and the possibility for widely tunable single photon sources. Such sources open new possibilities in quantum information experiments, including for instance enhancing the efficiency of a QD emitter by tuning it in resonance with a cavity mode [9], entangling the emission of two remote independent single QDs at the same energy [10], and fine-tuning the intermediate exciton state to suppress the fine structure splitting [11].

5.3 Possibility for non-linear PZ effects in (N11) QDs

A key characteristic of these high index-grown polar nanostructures is their possibility to exhibit pronounced strain-induced PZ fields, which can dramatically modify their electronic and optical properties as discussed in Chapter 1. According to linear elasticity theory applied to cubic polar heterostructures [12], the PZ polarization P_{PZ} in a biaxially-strained layer is proportional to the PZ coefficient e_{14} and the in-plane strain $\varepsilon_{//} = (\alpha_s - \alpha)/\alpha_s$ where, α_s and α are the lattice parameters of the substrate and layer, respectively. It is well known [13, 14] that e_{14} consists of two opposite-sign contributions: a purely "electronic" contribution versus an internal strain-induced one, often called simply "ionic". In III-V compound semiconductors, the electronic contribution exceeds the ionic one and e_{14} is negative. As an example, for bulk GaAs and InAs the experimental e_{14} values are -0.16 and -0.045 C/m^2, respectively [15]. In these bulk experiments, the strain values applied to the samples are minute, of the order of 10^{-6}, posing no real challenge to the linear elasticity model.

The situation is considerably different in the case of two-dimensional strained heterostructures, such as for instance InGaAs/GaAs quantum wells (QWs), where the typical lattice mismatch strain is about 1%. In such relatively high strains, it is likely that higher order terms, non-linear to strain, contribute to the PZ polarization. This is especially true in the case of InAs, where the near cancellation of the electronic and ionic contributions in the linear term favours the observation of nonlinear PZ effects [16]. Indeed, a notable nonlinear dependence of e_{14} on strain and a significant deviation from the extrapolated values based on the binary e_{14} values has been demonstrated in strained $In_xGa_{1-x}As$ (111)B QWs [17]. Evidence for nonlinear piezoelectricity has been also reported in CdTe QWs [18, 19].

The situation in the case of high-index InAs/GaAs nanostructures is even more favorable for observing nonlinear PZ effects, considering the very high strains that these nanostructures can sustain, reaching values up to 7%. Additionally to the discussion in Chapter 1, section 1.3.1, evidence for the existence of large PZ fields in (N11) InAs QDs has been reported previously [20] [21]. By using bulk InAs PZ coefficients, a PZ field of 250 kV/cm was estimated for (211) InAs QDs [20]. As a comparison, we note that this value is only a small fraction of the 7 MV/cm internal field observed in hexagonal c-axis oriented GaN QDs [22] [23]. However, late *ab initio* theoretical calculations of PZ coefficients in highly-strained InAs have suggested that the PZ field in (N11) InAs QDs reverses direction and is strongly enhanced by nonlinear PZ effects, reaching values in excess of 1 MV/cm for pure (211) InAs QDs [24]. Such strong fields are expected to fully dominate the optical and dynamic properties of (N11) InAs QDs.

5.4 Futuristic QD Device: Tunable SPE

Having in mind the demonstration of a tunable single photon emitter at elevated temperatures, and considering we have already observed the clear antibunching behaviour of PZ QDs up to 150K, we present here an experimental study of the Quantum Confined Stark Effect (QCSE) on the emission of single (211)B InAs/GaAs PZ QDs at 100K. Accordingly, bias-dependent micro-photoluminescence (μ-PL) experiments are performed on specially designed Schottky diode samples containing the PZ QDs, revealing pronounced Stark *redshifts* of the QD emission lines. The direction of these shifts intelligibly demonstrates that the direction of the PZ field is opposite to that predicted based on bulk InAs PZ coefficients, confirming the importance of non-linear PZ effects in heavily strained Zinc-Blende nanostructures. In figure 5.1 the electrical package containing the diodes mounted inside the

cryostat is presented. The package is attached on the cold finger of the cryostat and is mounted on a specially designed base (white in image) with electrical leads, having the ability to reload packages without any bonding and being fully compatible with cryogenics. The electric field is applied to the devices using vacuum compatible copper wires.

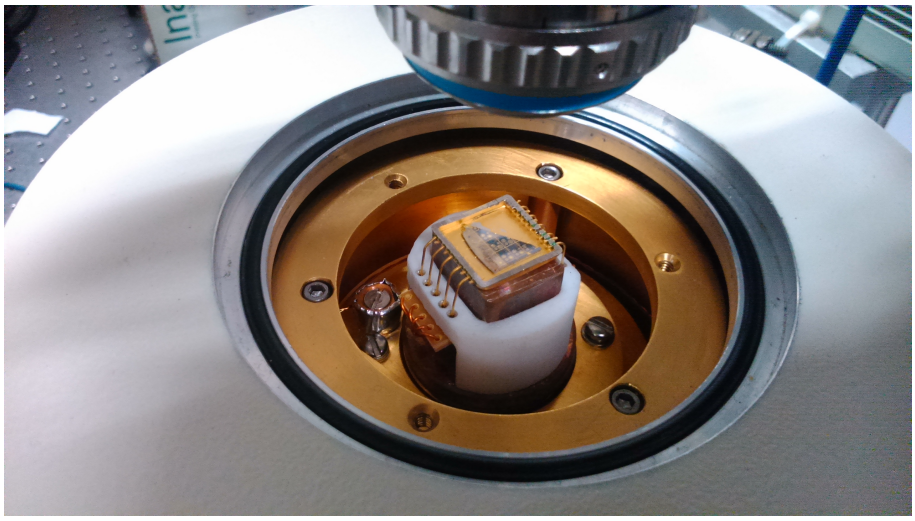

Figure 5.1: Image of the package containing the diodes mounted inside the cryostat.

5.4.1 Sample Fabrication

The sample is grown by molecular beam epitaxy on a (211)B GaAs semi-insulating substrate. The structure starts with a 1μm thick n^+ GaAs buffer layer, doped by 10^{18} cm^{-3}, to be used as the bottom n-contact. The intrinsic region contains first a 40x period 2.5nm/1.6nm GaAs/AlAs short-period super-lattice, serving as high quality template for the nucleation of QDs. Then follows the active region, which consists of three 50nm-thick $Al_{0.3}Ga_{0.7}As$ barrier layers, confining a first 12nm-thick GaAs *reference* QW_1 for the calibration of the actual electric field applied by the external bias, and a second 10nm-thick GaAs QW_2 containing the QD layer in the middle. The QD layer is formed in the Stranski-Krastanow mode

by deposition of 1.5 ML of InAs at 500^{o}C with a growth rate of 0.1 ML/s. The sample ends with a 5nm GaAs cap-layer to protect the top $Al_{0.3}Ga_{0.7}As$ layer from oxidation. A twin sample with an uncapped QD layer grown on the top surface under the same conditions provides information about the QD structural characteristics by Atomic Force Microscopy (AFM). The QDs have a density of a few times 10^9 cm^{-2}, typical height between 1.5 and 2.5 nm, and appear to have relatively large base-to-height aspect ratios, consistent with a truncated pyramid morphology [25].

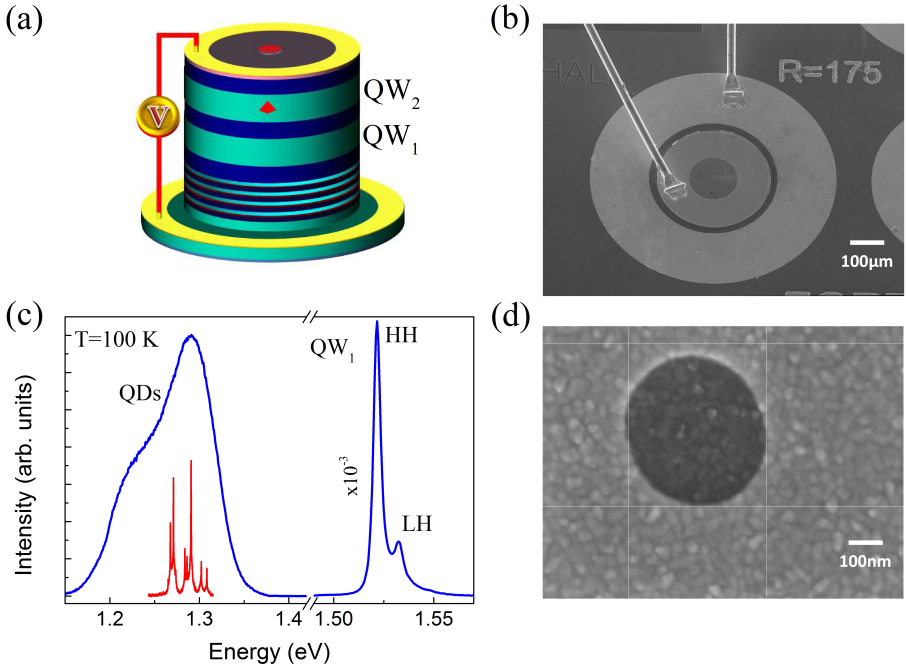

Figure 5.2: (a) Schematic representation of the total diode structure. (b) Top view SEM image of a bonded device. (c) Macro-PL spectrum (blue line) from the active region of the diode, showing characteristic emission from the QDs and QW_1 at 100K. The sharp-peaked spectrum in red is micro-PL emission through nano-apertures such as the one shown in (d), opened on the top metal layer.

A schematic of the complete Schottky diode structure is depicted in figure5.2(a), while a scanning electron microscopy (SEM) image of a bonded device is shown in

figure5.2(b). The diodes are fabricated using standard GaAs processing technology and consist of 0.75m deep mesas with 350-500 m diameter, etched down to the n^+ GaAs layer by reactive ion etching, onto which ring-shaped n-type (Ge/Au/Ni/Au) ohmic contacts are evaporated and activated by rapid thermal annealing at 410^{o}C. On the top of the mesa, Ti/Pt/Au Schottky contacts are formed in a ring-shaped geometry with 175-250 m wide rings at the edge of the mesas, whereas in the interior region of the rings 80nm of Ti are deposited and nano-apertures with varying diameters between 350nm and 5m are opened for optical access by electron beam lithography.

5.4.2 Experimental

An example of a 400nm diameter nano-aperture is shown in figure5.2(d). The μ-PL spectra are collected using a 40x objective with numerical aperture of 0.65 from a spot size smaller than 1.5μm. The sample is cooled down to 100K in a liquid N_2 (LN) flow cryostat. A variable-wavelength continuous-wave Ti:Sapphire laser is used as excitation source. The excitation power level in all bias-dependent experiments is kept sufficiently low to make screening effects in the diode negligible. The signal is dispersed in a 0.75m spectrograph with a 600 grooves/mm grating and is detected with a LN-cooled charge-coupled device (CCD) camera. Samples for HRTEM imaging are prepared in cross-sectional geometry, either by mechanical grinding or tripod polishing, followed by low-voltage Ar^+ ion-milling in the Gatan PIPS. HRTEM observations are carried-out in a Jeol 2011 electron microscope, operated at 200 kV. HRTEM images are digitized at a resolution of 4000 dpi using a Nikon SUPER COOLSCAN 9000 scanner and then are processed by Digital Micrograph software package. Strain analysis is performed on numerous HRTEM images of InAs QDs using the Geometrical Phase Analysis (GPA) method [26]. In the GPA method, the relative variation of the lattice fringe spacing is determined

by phase variations in the HRTEM images, with respect to a reference region. Assuming validity of Vegard's law, the GPA strain profile of a given QD can then be associated with compositional variations within the dot.

5.4.3 Optical characterization of the structure

The macro-PL spectrum obtained at 100K from an unprocessed part of the sample is presented in figure5.2(c), and exhibits characteristic broad emission from the QD layer in the 1.2-1.32 eV range, as well as intense heavy-hole (HH) and light-hole (LH) emission from the reference QW_1. The sharp-peaked spectrum underneath the QD macro-PL, corresponds to micro-PL emission from a few QDs through a nano-aperture of relatively small size.

5.5 Enhanced QCSE on PZ QDs

5.5.1 Applied Field calibration

In figure5.3(a), the PL spectra of QW_1 are plotted as a function of external reverse bias in the range 0 to 1.1V, showing pronounced Stark shifts for both transitions, reaching 10.8meV for the HH peak as the bias increases to 1.1V. Beyond this value, the QW_1 PL weakens drastically due to carrier escape and decrease of oscillator strength caused by band-bending. By comparison, the PL from single QDs persists up to 4V of external bias, reflecting the much stronger confinement in QDs.

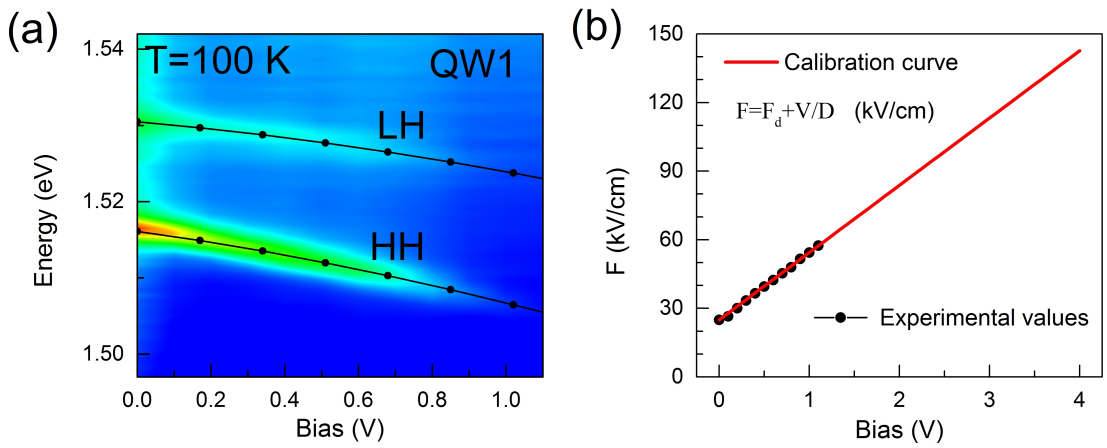

Figure 5.3: (a) Variation of HH and LH transition energies of QW_1 as a function of external bias at 100K. The dotted lines represent theoretical estimates of the QW_1 transitions. (b) Calibration curve (red line) between external bias and applied electric field extrapolated from the experimental points (dots) obtained by fitting the QW_1 transitions for each bias.

By solving the one dimensional (1D) self-consistent Schrdinger-Poisson equation for QW_1 as a function of applied electric field, and fitting the HH and LH transition energies for each bias, shown as dotted lines in figure5.3(a), we deduce the calibration curve of figure5.3(b) between applied electric field and external bias. The obtained linear law $F = F_d + \frac{V}{D}$ reproduces very well the one estimated for an *ideal* diode with an intrinsic region thickness of D=0.34m, while its zero-bias limit corresponds to an internal F_d diode field of 25kV/cm in good agreement with a Schottky barrier height of 0.8 eV.

5.5.2 Observation of large Stark Shifts from PZ SQDs

In figure 5.4(a) and (b), we present the PL images of two different single PZ QDs as a function of applied electric field by taking into account the calibration curve of figure5.3(b). In each case, the bi-exciton (XX) and neutral exciton (X) emission lines are identified, according to their quadratic and linear power dependence,

respectively, in conjunction with the absence of any other lines around the single QD emission.

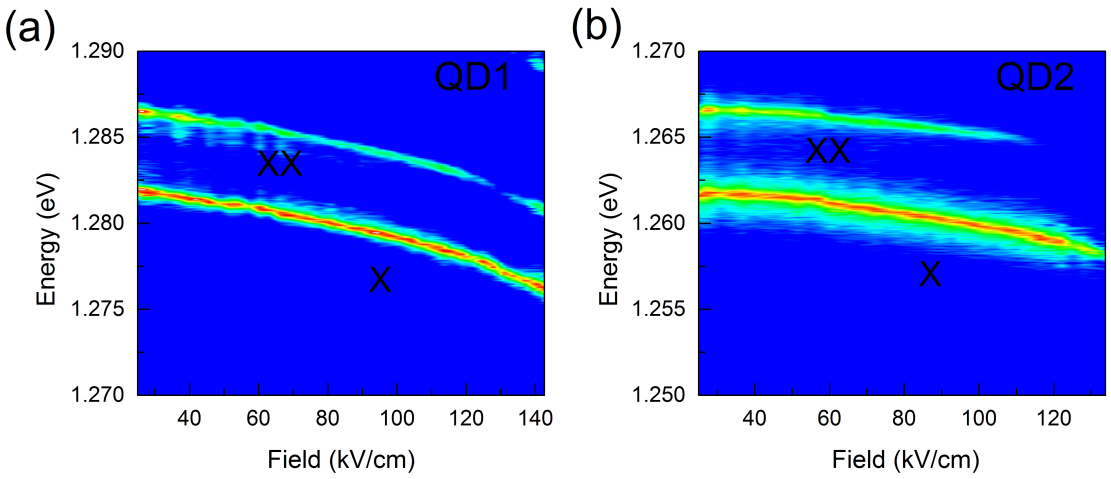

Figure 5.4: (a) and (b) PL images recorded for various values of the applied electric field at 100K represents the exciton and biexciton emission lines from two different single QDs.

The excitation power level is kept constant for all values of external bias, and is adjusted just below the saturation regime for the X state at zero bias. For clarity, the QD PL images in figure 5.4 are normalized to the X peak intensity. With increasing bias, the QD PL progressively drops in intensity, with the exposure times at high fields being three times larger compared to low fields. The main reason our experiments are limited to a reverse bias of 4V is to keep leakage currents low.

The continuous red-shift of the QD lines, throughout the applied bias range, allows us to conclude that the external field applied to the structure "adds" to the internal PZ field of the QD. This is already a significant result in itself, because it demonstrates for the first time experimentally the importance of second order PZ terms in Zinc-Blende nanostructures [24]. Because, if only linear PZ terms were important, then for the (211)B orientation and the sign of bulk InAs e_{14}

coefficient, the direction of the applied electric field would be anti-parallel to the PZ field, thus producing blue-shifts instead of the observed red-shifts.

In figure 5.4(a), we observe for the X transition of QD_1 a red-shift of about 5.8meV for the first 140kV/cm of external field, which is already ~ 4 times larger than the respective Stark shifts observed in (100) counterparts [27] in the same field range. Moreover, we observe that the Stark shift varies significantly from one QD to another. For instance, QD_2 in figure 5.4(b) gives a Stark shift of only 3.4 meV in the same field range. This cannot be attributed merely to QD size variation, as in this picture, QD_2 emitting at lower energies than QD_1 should be of larger QD size and thereby exhibit larger Stark shift, which is obviously not the case. These dot-dependent Stark shifts strongly suggest that not only the dot size but also the In-content varies from one dot to another. In order to explain the observed shifts, we resort to HRTEM measurements to obtain direct information about the strain state and In-content profile of our QDs.

5.5.3 HRTEM characterization

The conclusion from HRTEM imaging along the $[0\,1\,\overline{1}]$ and $[\overline{1}\,1\,1]$ projection directions is that QDs tend to adopt an anisotropic pyramidal shape, elongated along the $[\overline{1}\,1\,1]$ direction, with a base-aspect ratio in the range of 1.3-1.4. In figure 5.5(a), a typical HRTEM image of a QD along the $[0\,1\,\overline{1}]$ direction is shown, from which can be deduced, despite the presence of intense strain contrast, an approximate value of QD width of 8-10 nm, a QD height of about 2-3 nm, and a wetting layer (WL) thickness smaller than 1 nm. No structural defects are observed in the QD, whatsoever, neither at the interfaces with the GaAs layers nor at the core, implying the absence of plastic relaxation. GPA measurements are performed along the in-plane and out-of-plane directions. A $g/3$ size Gaussian mask (g is

the magnitude of the reciprocal space vector) is placed around the corresponding spatial frequencies in the fast Fourier transform of the HRTEM image, resulting in ≅1 nm spatial resolution in real space. The underlying GaAs layer is used as the reference region.

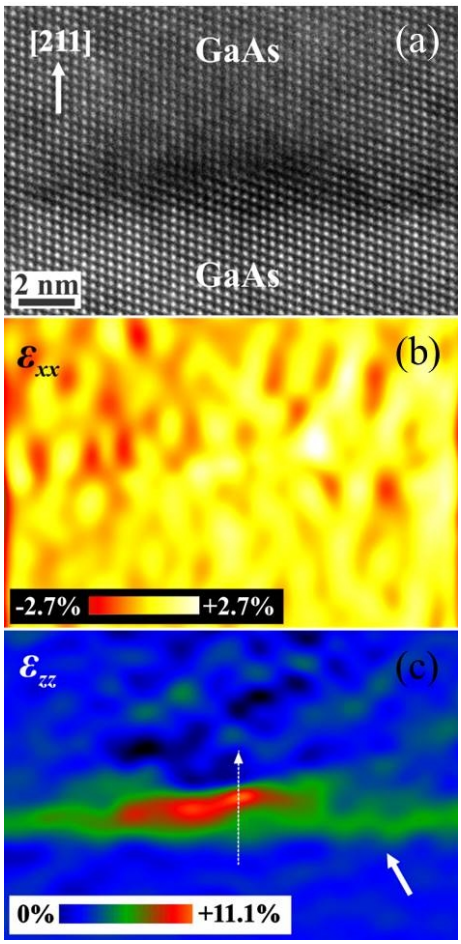

Figure 5.5: (a) HRTEM image in the $[0\,1\,\bar{1}]$ projection direction, depicting an InAs QD embedded in GaAs(211). (b) Corresponding in-plane GPA strain map showing an average $\varepsilon_{xx} = 0$ interfacial strain. (c) GPA strain map along the growth direction, illustrating the variation of the ε_{zz} strain inside QD with the GaAs lattice as reference. The shape of the QD is roughly delineated and the tilted arrow denotes the WL. The color map shows the corresponding line profile of the ε_{zz} strain along the dotted arrow, showing the progressive increase of ε_{zz} from the base towards the tip of the QD.

As shown in the GPA strain map of figure 5.5(b), an average $\varepsilon_{xx} = 0$ in-plane strain is determined, suggesting full registration of the two lattices and confirming elastically strained QDs in the absence of any interfacial misfit defects. Some small deviations of the ε_{xx} strain from the average value may arise due to thickness fluctuations of the sample in the area of interest, and can be neglected. Conversely, a significant variation of the GPA strain along the growth direction is observed in figure5.5(c). As depicted in the color map of the ε_{zz} profile of figure 5.5(c) there is a gradual variation of the out-of-plane strain along the growth direction. If we follow the dotted arrow in the same figure, ε_{zz} gradually increases from $\varepsilon_{zz} = 0.042 \pm 0.001$ near the GaAs/InAs interface to almost 0.111 ± 0.001 at the tip of the QD and then rapidly descends to zero over the tip. This trend is observed in almost all QDs studied, though with different absolute ε_{zz} values. The corresponding ε_{zz} profile across the WL starts from about 0 just above GaAs and reaches a maximum value of 0.042 ± 0.001, suggesting severe intermixing.

In order to substantiate the experimental ε_{zz} GPA strain values, the QDs are assumed to be under biaxial strain, and following the formulation of Hammerschmidt et al. [28], it is possible to determine from continuum-elasticity theory the Poisson's ratio and the strain tensor along the [2 1 1] direction of the zinc-blende lattice. Subsequently, the in-plane and out-of-plane elastic response of biaxially-strained pure InAs QDs are calculated, and in conjunction with the bulk lattice parameters of GaAs and InAs, the theoretical InAs-on-GaAs(211) $\varepsilon_{zz} = 0.1201$ GPA strain value is deduced. Hence, applying Vegard's law to our experimental strain measurements, the following conclusions on the chemical composition of the QD of figure 5.5 can be drawn: For $\varepsilon_{zz} \cong 0.042$ to 0.111 (± 0.001) GPA strain values, the corresponding In-content in the QD progressively increases from $x_{QD} = 0.35$ to 0.92 (± 0.01) from the base to the tip of the QD, making it clear that Ga segregates in the QD lattice mainly at the initial stages of QD growth. Simi-

larly, the In-content in the WL seems to increase from 0 at the interface to about 0.35 ($\pm$0.01), suggesting that it should be rather considered as an $In_xGa_{1-x}As$ alloy. Among the different QDs studied by GPA, a minimum of $x_{QD} = 0.20 \pm 0.01$ at the base region and a maximum of $x_{QD} = 0.92 \pm 0.01$ near the tip have been estimated. It should be pointed out however, that despite the fact that HRTEM imaging is performed on very thin areas of the sample with thickness comparable to the dimensions of the QDs (< 10 nm), considering that the dots are entirely buried in GaAs and their HRTEM images are 2D projections of 3D material, a slight influence on the ε_{zz} and therefore on the In content of the QDs is still probable.

5.5.4 A comparison on the QCSE of (211) vs (100) QDs

In this section is presented the effort to simulate the observed transition energies and Stark shifts of our (211)B InAs QDs, using a graded In-composition potential profile, according to the conclusions of the strain analysis of HRTEM images. This is achieved by solving a 1D Schrdinger equation in the envelope function approximation, using the nextnano3 semiconductor nano-device simulator [29], including strain and PZ effects in the (211)B orientation. The 1D simplification is justified in our case, by the large aspect ratio of the QDs, implying that quantum confinement along the growth direction is much stronger compared to the lateral dimensions, and the fact that the applied electric field is perpendicular to the growth plane.

The QD height is fixed to 2 nm, in keeping with AFM and HRTEM results. Then, we try several In-profiles in order to reproduce the X transition energy and the Stark shift of QD_1 in figure5.4(b). For this particular QD, best fitting is obtained in figure5.6(a) assuming a linear In-profile starting from 30% at the base

and reaching 74% at the apex of the dot. It should be noted here, that the X transition energy is quite sensitive to the average In content in the QD, but not so much on the steepness of the In profile. As an example, for pure InAs QDs the X transition energy is estimated 0.26 eV lower than the 1.282eV of QD_1. On the other hand, if instead of the 30% to 74% profile, we assumed 0% to 100%, the X transition energy would merely change by 6 meV. The steepness of the In-profile, however, has a clear effect on the Stark shift curve. In the above estimates, the nonlinear PZ effect has been taken into account, using the second order PZ coefficients of Bester et al. [24].

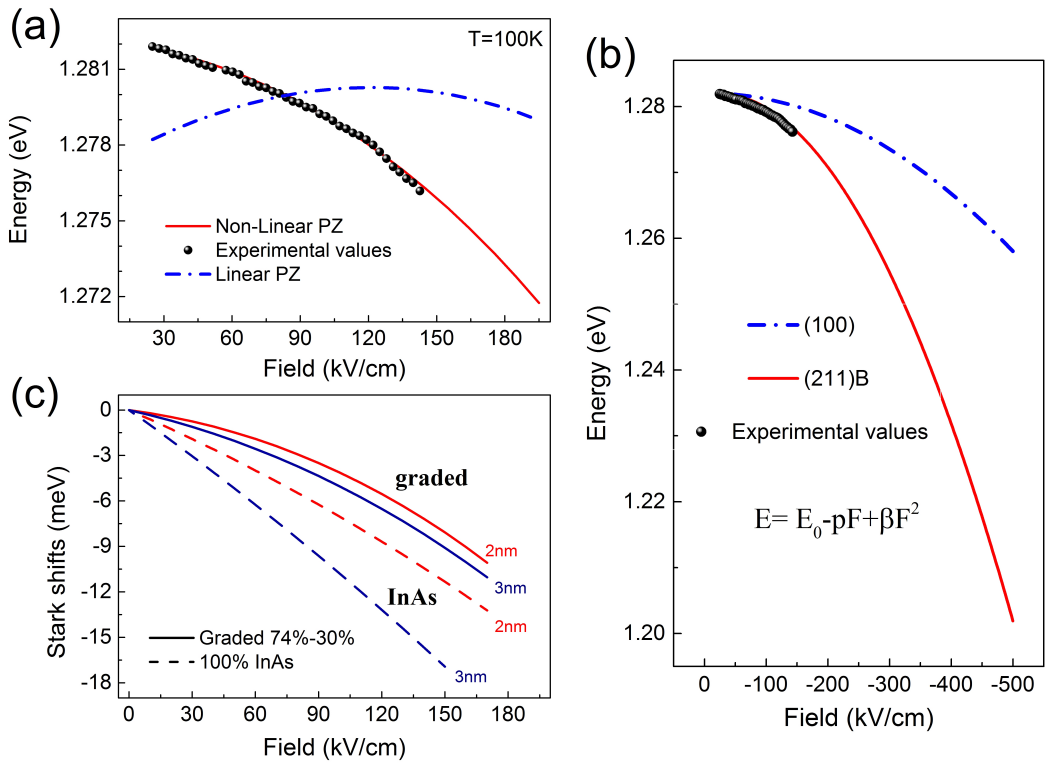

Figure 5.6: (a) Experimental values (dots) of the QD X transition energy versus applied electric field and calculated curve (red line) including non-linear PZ terms. The calculated curve with only linear PZ-terms taken into account (dashed-line) is also shown for comparison. (b). Comparison of Stark shifts between (211)B and (100) QDs showing the potential of PZ QDs in obtaining enormous Stark shifts compared to non-PZ QDs. (c.) Calculated Stark shifts of the X transition energy of QDs with heights of 2nm and 3nm, either for pure InAs (dashed-lines) or for graded 74% to 30% In content profile (solid-lines).

In figure 5.6(a), we compare the best fitting solid curve with the dash-dotted line, which is produced assuming only linear terms in the PZ coefficient and which clearly predicts a blue-shifting behaviour, unlike the experimental observation.

Next in figure 5.6(b), we extend the calculated Stark shifts for QD1 up to 500 kV/cm, in order to compare them with the reported experimental data for non-PZ (100) InAs QDs [27]. A Stark shift up to 80meV can be expected from our

(211)B QDs at 500kV/cm, showing the large potential of these PZ dots towards the implementation of broadly tunable single photon emitters at high temperatures. Finally, in figure5.6(c), we plot the estimated Stark shifts in the case of pure (211)B InAs QDs (dashed lines) or 30%-74% graded In profile (211)B In(Ga)As QDs (solid lines), for two different QD heights of 2 and 3 nm. The curves follow the expected trend, in the sense that the larger Stark shifts correspond to the pure and larger QDs, with the shifts almost doubling with respect to the graded QDs in the first 150kV/cm.

5.6 conclusions

In summary, we have observed enhanced Stark tunings of single exciton lines of (211)B InAs QDs at 100K, due to the internal PZ field present in these nanostructures. The observed Stark shifts are up to a factor of 4 higher compared to standard non-PZ (100) InAs QDs, making this PZ QD system quite suitable for the implementation of tunable single photon emitters at high temperatures. To account quantitatively for the observed transition energies and Stark shifts, we utilized a graded In-composition potential profile, as deduced from the strain analysis of high-resolution transmission microscopy images. The direction of the observed redshifts clearly demonstrates that the PZ field is opposite to that predicted based on bulk InAs PZ coefficients. Our findings are in excellent agreement with recent theory taking into account nonlinear piezoelectric effects in highly strained InAs [16], and have wide implications on the understanding of strained nanostructures grown along polar directions, such as for instance nanowire heterostructures grown along (111) crystallographic orientations.

REFERENCES

[1] Matthew Pelton, Charles Santori, Jelena Vucković, Bingyang Zhang, Glenn Solomon, Jocelyn Plant, and Yoshihisa Yamamoto. Efficient Source of Single Photons: A Single Quantum Dot in a Micropost Microcavity. *Phys. Rev. Lett.*, 89(23):1–4, November 2002.

[2] N. Akopian, N. H. Lindner, E. Poem, Y. Berlatzky, J. Avron, D. Gershoni, B. D. Gerardot, and P. M. Petroff. Entangled photon pairs from semiconductor quantum dots. *Phys. Rev. Lett.*, 96(13):7–10, April 2006.

[3] Charles Santori, David Fattal, Jelena Vucković, Glenn S Solomon, and Yoshihisa Yamamoto. Indistinguishable photons from a single-photon device. *Nature*, 419(6907):594–597, 2002.

[4] Satoshi Kako, Charles Santori, Katsuyuki Hoshino, Stephan Götzinger, Yoshihisa Yamamoto, and Yasuhiko Arakawa. A gallium nitride single-photon source operating at 200 K. *Nat. Mater.*, 5(11):887–892, 2006.

[5] Andrei Schliwa, Momme Winkelnkemper, Anatol Lochmann, Erik Stock, and Dieter Bimberg. In(Ga)As/GaAs quantum dots grown on a (111) surface as ideal sources of entangled photon pairs. *Phys. Rev. B - Condens. Matter Mater. Phys.*, 80(16):161307, October 2009.

[6] Ranber Singh and Gabriel Bester. Nanowire quantum dots as an ideal source of entangled photon pairs. *Phys. Rev. Lett.*, 103(6):1–4, August 2009.

[7] Savvas Germanis, Alexios Beveratos, George E. Dialynas, George Deligeorgis, Pavlos G. Savvidis, Zacharias Hatzopoulos, and Nikos T. Pelekanos. Piezoelectric InAs/GaAs quantum dots with reduced fine-structure splitting for the generation of entangled photons. *Phys. Rev. B - Condens. Matter Mater. Phys.*, 86(3):1–10, 2012.

[8] Matthieu Larqué, Isabelle Robert-Philip, and Alexios Beveratos. Bell inequalities and density matrix for polarization-entangled photons out of a two-photon cascade in a single quantum dot. *Phys. Rev. A - At. Mol. Opt. Phys.*, 77(4):042118, 2008.

[9] A K Nowak, S L Portalupi, V Giesz, O Gazzano, C Dal Savio, P-F Braun, K Karrai, C Arnold, L Lanco, I Sagnes, A Lemaître, and P Senellart. Deterministic and electrically tunable bright single-photon source. *Nat. Commun.*, 5:3240, 2014.

[10] R. B. Patel, a. J. Bennett, I. Farrer, C. a. Nicoll, D. a. Ritchie, and a. J. Shields. Tunable Indistinguishable Photons From Remote Quantum Dots. *Nat. Photonics*, 4(July):632–635, 2010.

[11] A. J. Bennett, M. A. Pooley, R. M. Stevenson, M. B. Ward, R. B. Patel, A. Boyer de la Giroday, N. Sköld, I. Farrer, C. A. Nicoll, D. A. Ritchie, and A. J. Shields. Electric-field-induced coherent coupling of the exciton states in a single quantum dot. *Nat. Phys.*, 6(October):947–950, 2010.

[12] D. L. Smith and C. Mailhiot. Theory of semiconductor superlattice electronic structure. *Rev. Mod. Phys.*, 62(1):173–234, January 1990.

[13] Richard M Martin. Piezoelectricity. *Phys. Rev. B*, 5(4):1607–1613, February 1972.

[14] Walter a. Harrison. Effective charges and piezoelectricity. *Phys. Rev. B*, 10:767–770, 1974.

[15] P Quadflteo. Piezoelectricity in III-V Compounds with a Phenomenological Analysis of the Piezoelectric Effect. *October*, 323:323–330, 1968.

[16] Andrea Dal Corso, Raffaele Resta, and Stefano Baroni. Nonlinear piezoelectricity in CdTe. *Phys. Rev. B*, 47(24):16252–16256, June 1993.

[17] J. L. Sánchez-Rojas, A. Sacedón, F. González-Sanz, E. Calleja, and E. Muñoz. Dependence on the in concentration of the piezoelectric field in (111)B InGaAs/GaAs strained heterostructures. *Appl. Phys. Lett.*, 65(16):2042–2044, 1994.

[18] R. André, C Deshayes, J Cibert, Le Si Dang, S Tatarenko, and K Saminadayar. Optical studies of the piezoelectric effect in (111)-oriented CdTe/Cd1-xZnxTe strained quantum wells. *Phys. Rev. B*, 42(17):11392–11395, December 1990.

[19] R. André, C. Bodin, J. Cibert, L. S. Dang, and G. Feuillet. Non-linear piezoelectric effect in CdTe and CdZnTe. *Le J. Phys. IV*, 03(C5):429–432, 1993.

[20] S. Sanguinetti, M. Gurioli, E. Grilli, M. Guzzi, and M. Henini. Piezoelectric-induced quantum-confined Stark effect in self-assembled InAs quantum dots grown on (N11) GaAs substrates. *Appl. Phys. Lett.*, 77(13):1982, 2000.

[21] M. Gurioli, S. Sanguinetti, and M. Henini. Dynamic quantum-confined stark effect in self-assembled InAs quantum dots. *Appl. Phys. Lett.*, 78(7):931–933, 2001.

[22] F. Widmann, J. Simon, N. T. Pelekanos, B. Daudin, G. Feuillet, J. L. Rouvière, and G. Fishman. Giant piezoelectric effect in GaN self-assembled quantum dots. *Microelectronics J.*, 30(4):353–356, 1999.

[23] J. Simon, N. Pelekanos, C. Adelmann, E. Martinez-Guerrero, R. André, B. Daudin, Le Dang, and H. Mariette. Direct comparison of recombination dynamics in cubic and hexagonal GaN/AlN quantum dots. *Phys. Rev. B*, 68(3):035312, July 2003.

[24] Gabriel Bester, Xifan Wu, David Vanderbilt, and Alex Zunger. Importance of second-order piezoelectric effects in zinc-blende semiconductors. *Phys. Rev. Lett.*, 96(18):1–4, 2006.

[25] G. E. Dialynas, S. Kalliakos, C. Xenogianni, M. Androulidaki, T. Kehagias, P. Komninou, P. G. Savvidis, Z. Hatzopoulos, and N. T. Pelekanos. Piezoelectric InAs (211)B quantum dots grown by molecular beam epitaxy: Structural and optical properties. *J. Appl. Phys.*, 108(10):103525, 2010.

[26] M. J. Hÿtch, E. Snoeck, and R. Kilaas. Quantitative measurement of displacement and strain fields from HREM micrographs. *Ultramicroscopy*, 74(3):131–146, 1998.

[27] Anthony J. Bennett, Raj B. Patel, Joanna Skiba-Szymanska, Christine a. Nicoll, Ian Farrer, David a. Ritchie, and Andrew J. Shields. Giant Stark effect in the emission of single semiconductor quantum dots. *Appl. Phys. Lett.*, 97(3):1–4, 2010.

[28] T. Hammerschmidt, P. Kratzer, and M. Scheffler. Elastic response of cubic crystals to biaxial strain: Analytic results and comparison to density functional theory for InAs. *Phys. Rev. B - Condens. Matter Mater. Phys.*, 75(23):1–6, 2007.

[29] Stefan Birner, Tobias Zibold, Till Andlauer, Tillmann Kubis, Matthias Sabathil, Alex Trellakis, and Peter Vogl. Nextnano: General purpose 3-D simulations. *IEEE Trans. Electron Devices*, 54(9):2137–2142, 2007.

Chapter 6

Conclusions and Future perspectives

The advantages of InAs QDs, grown on (211)B GaAs substrates, has been deeply investigated in this work, harnessing GaAs technology as well as the strain-induced internal electric field within the QDs. In this context, negligible fine structure splittings have been derived from *as-grown* piezoelectric QDs, which is less than $10mu$eV, accompanied by single photon emission, up to temperatures as high as 150K, making them the best candidates for single or even entangled photon sources, at elevated temperatures. Moreover, the demonstration of enhanced Stark shifts from a single InAs piezoelectric QDs, utilizing the high internal electric fields, proves the importance of non-linear piezoelectric effect in Zinc-Blende structures, making them an excellent choice for tunable single photon emitters at high temperatures. These results unravel a completely new standard for applications based on semiconductor QDs.

Piezoelectric QDs of such potential would be optimal for having a deeper understanding, about the quantum mechanical phenomena in low dimensional semiconductor based structures. However in such structures, it would be really

fascinating to observe single photon emission, at elevated temperatures, by electrical injection. Another area of interest would be QDs having a greater height, in comparison to the ones discussed in this work, leading to larger Stark shifts.